Climate Modeling & Downscaling for Semi-Arid Regions

by

Ashish Sharma

A Dissertation Presented in Partial Fulfillment
of the Requirements for the Degree
Doctor of Philosophy

Approved August 2012 by the
Graduate Supervisory Committee:

Huei-Ping Huang, Chair
Ronald Adrian
Marcus Herrmann
Patrick E. Phelan
Enrique Vivoni

ARIZONA STATE UNIVERSITY

December 2012

ABSTRACT

This study performs numerical modeling for the climate of semi-arid regions by running a high-resolution atmospheric model constrained by large-scale climatic boundary conditions, a practice commonly called climate downscaling. These investigations focus especially on precipitation and temperature, quantities that are critical to life in semi-arid regions. Using the Weather Research and Forecast (WRF) model, a non-hydrostatic geophysical fluid dynamical model with a full suite of physical parameterization, a series of numerical sensitivity experiments are conducted to test how the intensity and spatial/temporal distribution of precipitation change with grid resolution, time step size, the resolution of lower boundary topography and surface characteristics.

Two regions, Arizona in U.S. and Aral Sea region in Central Asia, are chosen as the test-beds for the numerical experiments: The former for its complex terrain and the latter for the dramatic man-made changes in its lower boundary conditions (the shrinkage of Aral Sea). Sensitivity tests show that the parameterization schemes for rainfall are not resolution-independent, thus a refinement of resolution is no guarantee of a better result. But, simulations (at all resolutions) do capture the inter-annual variability of rainfall over Arizona. Nevertheless, temperature is simulated more accurately with refinement in resolution. Results show that both seasonal mean rainfall and frequency of extreme rainfall events increase with resolution. For Aral Sea, sensitivity tests indicate that while the shrinkage of Aral Sea has a dramatic impact on the precipitation over the confine of (former) Aral Sea itself, its effect on the

precipitation over greater Central Asia is not necessarily greater than the inter-annual variability induced by the lateral boundary conditions in the model and large scale warming in the region. The numerical simulations in the study are cross validated with observations to address the realism of the regional climate model.

The findings of this sensitivity study are useful for water resource management in semi-arid regions. Such high spatio-temporal resolution gridded-data can be used as an input for hydrological models for regions such as Arizona with complex terrain and sparse observations. Results from simulations of Aral Sea region are expected to contribute to ecosystems management for Central Asia.

DEDICATION

To my family

ACKNOWLEDGMENTS

I am extremely grateful to my advisor, Professor Huei-Ping Huang, for giving me an opportunity to work under his mentorship towards my PhD. I am thankful for his invaluable advice, patience guidance, exceptional support and encouragement throughout the course of my doctoral studies and this research. In past, I had the privilege of having him as a member of my supervisory committee for my Master's thesis.

There are no words to express my deep gratitude to Prof. H.J.S. Fernando for his mentorship throughout my graduate studies. He is so impressive in his teaching that made continue my doctoral studies.

I am also grateful to Dr. Ronald J. Adrian, Dr. Marcus Herrmann, Dr. Patrick E. Phelan and Dr. Enrique Vivoni for their input and guidance as my committee members. I would like to thank our collaborators Dr. Peter Zavialov and Valentina Khan from P.P.Shirshov Institute of Oceanology of the Russian Academy of Sciences, Moscow, Russia for their valuable comments. I would also like to acknowledge the support by NSF AGS-0934592, NOAA CPPA Program and U.S. CRDF.

I would also like to thank the EFD family and my friends for their constant support and help. I would like to thank my wife Meenu who has been supportive throughout my doctoral career. Finally, I am thankful to God and grateful to my parents for their constant motivation and support throughout my career and especially during my graduate studies abroad.

TABLE OF CONTENTS

Page

CHAPTER Page

CHAPTER Page

LIST OF TABLES

LIST OF FIGURES

Figure Page

Figure Page

Figure Page

Figure Page

Figure Page

Chapter 1

1. INTRODUCTION

This work focuses on the need to relate local- and regional-scale climate variables to the large scale atmospheric forcings by *climate downscaling* for semi-arid regions. The term "climate downscaling" refers to the use of a high-resolution atmospheric model to produce detailed regional climate, given the large-scale boundary conditions provided by the output of coarse resolution global climate models or by coarse resolution observations. The numerical simulations in this study will use the Weather Research and Forecasting (WRF) model. A series of numerical sensitivity experiments will be conducted to test how the intensity and spatial/temporal distribution of precipitation and temperature change with grid resolution, physical parameterization, time step size, resolution of lower boundary topography and change in surface characteristics.

1.1 Motivation

The climate variability is important and affects many aspects of human life in semi-arid regions. Water resources are scarce in such regions and a slight reduction or increase in rainfall can produce huge impact on societal living. Thus, these regions are very sensitive to small changes in climate. For example, small change in climate can cause famine, droughts or local floods, and people need to manage water resources for long-term development. Hence, it is important that

climate variability in a semi-arid region should be well understood in order to formulate more sustainable policies and strategies. According to the assessment of population levels by the Office to Combat Desertification and Drought of the United Nations Development Programme (UNDP), the arid and semi-arid regions in the world account for approximately 30% of the world total area and are inhabited by approximately 20% of the total world population. The arid and semi-arid regions hold are about 24% of the total population in Africa, 17% in the Americas and the Caribbean, 23% in Asia, 6% in Australia and Oceania, and 11% in Europe [*UNDP/UNSO*, 1997]. Thus, the intensity of extreme events of rainfall has important implications for regional climate and water management of semi-arid regions.

1.2 Need for Downscaling Of Global Climate Model Simulations

We rely on the output of global climate models to make major decisions on economical and societal activities. There have been considerable improvements in the last two decades in the quality of climate models. Nevertheless, even the state of the art climate models have coarse resolutions of *O*(100 km) [IPCC 2007, for example see Figure 1] which is not sufficient to resolve mesoscale flows. At this length scale *O*(100 km) or above, global climate models simulate large-scale circulation patterns [*Giorgi*, 1990; *Hurrell*, 1995] and their output can be used to define the boundary conditions for mesoscale models. Global models lack the ability to resolve fine topography at local scales. Thus,

climate information derived from them needs to be further downscaled to improve the accuracy of assessing and predicting climate at local and regional scales. For the purpose of this study, it is important to note that most of the rainfall in the global models is produced by subgrid-scale precipitation with very crude representation of surface heterogeneity within a grid box. While those models have produced meaningful projections of large-scale hydrological conditions in future climate, [e.g., *Seager et al*. 2007], they are less useful in predicting local changes in precipitation especially for regions characterized by complicated terrain and/or spatially concentrated rainfall patterns.

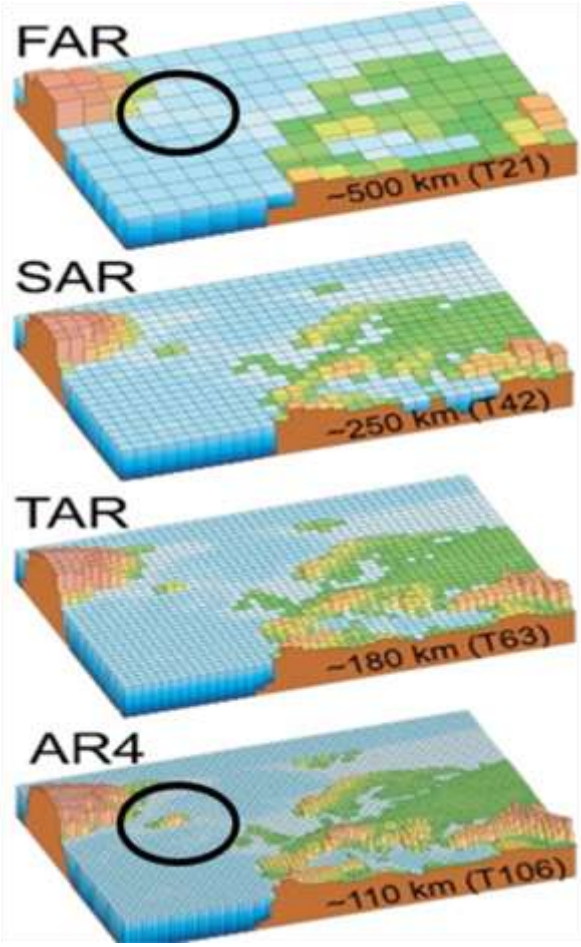

Figure 1: Improvement in topographic resolutions for global climate models according to Intergovernmental Panel on Climate Change (IPCC). The four panels are the Assessment Reports (AR) by [*IPCC*, 2007]. The First Assessment Report (FAR) was released in 1991, Second Assessment Report (SAR) in 1996, Third Assessment Report (TAR) in 2001 and Fourth Assessment Report (AR4) in 2007. The grid resolution for each AR is shown in their corresponding figure panels. The highlighted black circle in first panel shows missing Iceland and England from topographic resolution from FAR. Improvements in ARs made these topographic features explicitly visible with advancements in time as circled in AR4.

As a potential remedy, a complementary approach has been developed that utilizes large-scale boundary conditions to constrain a mesoscale model for long-term, regional climate prediction [e.g., *Leung,* 2003; *Leung and Qian*, 2003; *Lo et al*., 2008]. These constraints prevent the model from drifting away from the driving conditions applied on the boundary conditions, especially in mid and upper troposphere regions [*Giorgi and Bates*, 1989; *Giorgi and Marinueci*, 1991]. Thus, the mesoscale model simulation is usually driven by time dependent large-scale fields (e.g. wind, temperature, water vapor and surface pressure) provided either by analyses of observations or by a GCM to the lateral boundaries of the domain. This approach allows regional climate features and extreme events to be more realistically simulated and produce results that are more accurate than those from the driving GCM. A regional climate model (RCM) usually has a different horizontal and vertical resolution and set of parameterizations from those of GCMs which are forcing RCMs. Another benefit of running a regional climate model is that its output can be further used as an input for a hydrological model at micro-scale to improve water resource management.

1.3 Objectives

Because the prediction of climate change is vital for mitigation, adaptation, and planning in various sectors of society and the economy, quantifying uncertainty at different resolutions is important. Thus, the objective of this research is to study the numerical sensitivity for regional climate, focusing

specially on rainfall for semi-arid regions. The central problem to address in this thesis is the sensitivity of mesoscale climate simulations as the model resolution approaches the "cloud-resolving scale" of $L < 10$ km. Using the Weather Research and Forecast (WRF) model [*Skamarock et al*., 2008], a non-hydrostatic geophysical fluid dynamical model with a full suite of physical parameterization, a series of numerical sensitivity experiments are conducted to test how the intensity and spatial/temporal distribution of precipitation and temperature change with grid resolution, time step size, resolution of lower boundary topography and surface characteristics. Two regions, Arizona in U.S. and Aral Sea in Central Asia, are chosen as the testbeds for the numerical experiments (Figure 2). Inspite of being different in landscapes and at different locations, they have scanty rainfall and desert vegetation. The former has dramatic contrasts in topography and local rainfall patterns [*Seller et al*., 1960; *Sheppard et al.*, 2002; *Woodhouse*, 1997] that provide an ideal test ground for studying the impact of model resolution. The latter region concentrates on addressing the sensitivity of simulated precipitation and temperature on a change in distribution of surface characteristics and land mask at the surface. The numerical simulations for both the regions are compared with observations to address the realism of the regional climate model.

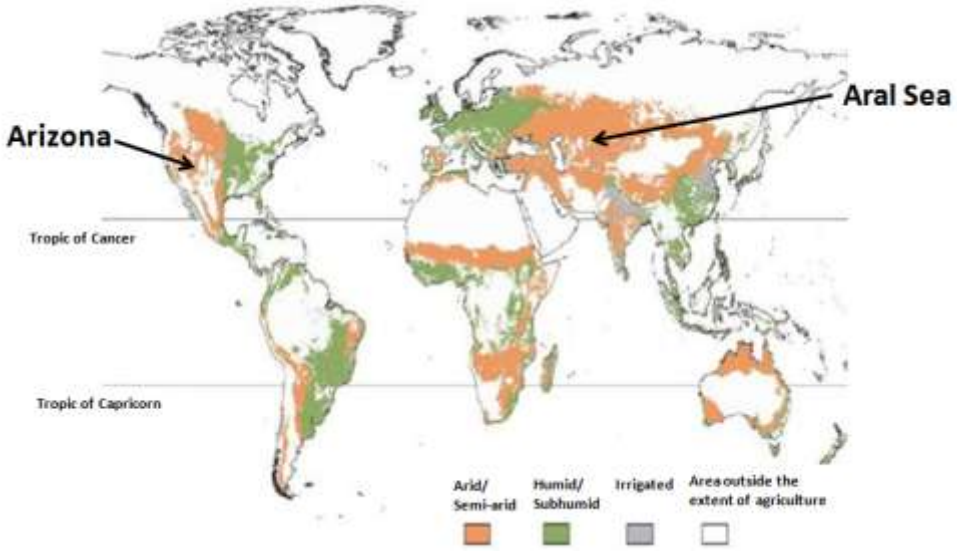

Figure 2: World map showing arid/semiarid, humid, irrigated regions of the world based on agricultural areas from World Development Report [*WDR*, 2008]. See link for more details: (http://www.syngentafoundation.org/index.cfm?pageID=46) Mostly, arid and semiarid regions are in subtropics.

1.4 Regional Climate Modeling

For the first part of the study, simulations for Arizona are performed over seven winter (November-January) seasons. The dependence of the climatology as well as high-frequency behavior of simulated rainfall on model resolution and/or subgrid-scale convective scheme is analyzed. To maintain focus, the analyses focus on liquid-form precipitation. For completeness, wintertime snowfall is also studied for two years for Arizona. Winter season is chosen for most of the

simulations because numerical models, whether global or regional, are widely known to produce substantial bias in North American summer monsoon [e.g., *Collier et al.*, 2007; *Lin et al.*, 2008]. Their performance for wintertime precipitation is generally more robust. The second part of the study investigates the effect of change in surface topography and surface vegetation coverage over Aral Sea region. Here, both wintertime and summertime regional climate simulations are performed for two decades. Both forms of precipitations (rain and snow) and temperature are studied over the region. To quantify the sensitivity of the changing surface boundary condition, a set of simulations with an identical lateral boundary condition but different extents of the Aral Sea are performed. These regional climate simulations will be performed using the WRF model.

While using a regional climate model, one has to make sure that the domain used in the simulation is big enough to allow full development of circulations and horizontal resolution optimum to capture small-scale features. Thus, for simulations of Arizona, the outermost domain covers almost complete US and some North Pacific Ocean and for Aral Sea the outermost domain covers almost Asia and some parts of Europe. We use nesting to downscale the climate data form coarse to fine resolution over an area of interest domain. During this process, it is expected that as the grid spacing is decreased, the simulations produce results closer to observations due to the refinement in topography. This primary hypothesis is designed to test the sensitivity of the model at different grid resolutions of 12 to 3 km. It is hypothesized that, as grid spacing is decreased below 12 km, the simulation results match close to observations. For this premise,

Arizona is used as a test-bed. A secondary hypothesis tests if reduction in vegetation cover and drying of water bodies has an effect on decrease in rainfall and increase in warming in a region. Aral Sea region in Central Asia is selected for this hypothesis.

Regional climate models (RCMs) play an important role in downscaling global climate model information to the regional and local scale at which local stakeholders and decision makers operate. This dissertation will contribute to climate science and applications of RCMs to hydrological, ecological, agricultural and water resource management problems, including the study of hydrologic extremes for event rainfall amounts. A byproduct of the analysis from some simulations also provides insight on the interaction of regional and local climate with large-scale climatic conditions.

In chapter 2, the Weather Research and Forecasting (WRF) model shall be introduced, and the numerics and physics inside the model will be discussed. The chapter 3 examines the numerical sensitivity of the model for our first test domain of Arizona. Chapter 4 is an extension of the study on Arizona where we compare station observations with simulations. In chapter 5, the sensitivity tests are performed at a different level of complexity over Aral Sea region by artificially modifying the model to replicate the true changed surface characteristics. In the sixth chapter the dissertation will conclude, stating the future goals after summarizing the results.

Chapter 2

2. WRF MODEL

The model used for this research work is the Advanced Research Weather Research and Forecasting (WRF) (ARW) version 3.1. The Weather Research and Forecasting (WRF) model is a Numerical Weather Prediction (NWP) and atmospheric simulation system designed for both research and operational applications [*Wang et al.*, 2008]. We present a brief overview of the WRF Model to get an insight about the modeling technique and procedure.

2.1. Governing equations

The fundamental equations that govern the motions of the atmosphere are derived from the basic laws of physics, particularly the conservation laws of mass, momentum and energy. In addition to the three conservation laws, climate models require an equation of state that relates several parameters to other equations and a moisture equation. For atmosphere, equation of state relates the pressure, density and temperature. This equation, together with the moisture equation and the equation for conservation of mass, momentum and energy, constitute the basic equations used in climate modeling.

Navier-Stoke Equations are:

Momentum equation: $$\frac{\partial \mathrm{v}}{\partial t} + \mathrm{v}.\nabla \mathrm{v} = -\frac{1}{\rho}\nabla p + 2\Omega \times \mathrm{v} + \nu \nabla^2 \mathrm{v} \qquad (1)$$

Continuity Equation: $$\frac{\partial \rho}{\partial t} + \nabla.(\rho \boldsymbol{v}) = 0 \qquad (2)$$

Equation of state: $p = \rho RT$ (3)

The extra term $2\Omega \times \mathrm{v}$ in momentum equation is the Coriolis term, where Ω is the angular velocity and $\boldsymbol{v}$ is the velocity vector. We use thermodynamical equation to calculate temperature and potential temperature given by:

$$\frac{\partial T}{\partial t} + \boldsymbol{v}.\nabla T = \kappa \nabla^2 T + Q_T \tag{4}$$

Conventionally, Navier-Stoke equation doesn't have moisture equation. We focus on moisture to analyze precipitation. So, the general equation for moisture q is given by,

$$\frac{\partial q}{\partial t} + \nabla.(\mathrm{v}\, q) = Q_q \tag{5}$$

All the above equations constitute the basic equations used in climate modeling. The global climate models have grid spacing $\Delta x \sim O(100\mathrm{km})$ but the Kolmogorov scale is $\sim O(\mathrm{cm})$. Hence, finer structures appear with increasing resolution. But, it is computationally not possible to reach close to Kolmogorov scale for climate simulations for relatively large domains. This brings us to make certain approximations. For atmospheric model, WRF, we neglect actual

molecular viscosity from momentum equation. Thus, the rest of the terms in momentum equation resolve only the large-scale flow and a lot of phenomenon are unresolved. Instead, we include big forcing/damping terms F_U, F_V, F_W and F_Θ. These terms are the result of sub-grid scale processes. A part of these terms include Coriolis force terms $F_{U_{cor}}, F_{V_{cor}}$ and $F_{W_{cor}}$, that are real and resolved. The rest terms compensate for the phenomenon that remains unresolved. These terms include diabatic forcings like solar radiations and parameterized sub-grid scale effects that involve small-scale momentum fluxes.

The equations in the WRF model use a terrain-following mass vertical coordinate [*Laprise*, 1992] with top of the model as a constant pressure surface to better simulate airflow over complex terrain. The equations use a terrain-following hydrostatic-pressure vertical coordinate η defined by a normalized hydrostatic pressure (or mass) as,

$$\eta = (p_h - p_{ht})/\mu, \tag{6}$$

where $\mu = p_{hs} - p_{ht}$. p_h is the hydrostatic component of the pressure, p_{hs} is the pressure at the surface and p_{ht} refer to values along the top boundaries. Value of η varies from 1 at the surface to 0 at the upper boundary of the model domain as shown in Figure 3. Since the vertical coordinate is pressure based and normalized, it is easy to mathematically cast governing equations of the

atmosphere into a relatively simple form. This terrain-following mass vertical coordinate has its advantages: The coordinate system conforms to natural terrain. This allows for good depiction of continuous fields, such as temperature, advection and winds, in areas where terrain varies widely but smoothly. It lends itself to increasing vertical resolution near the ground. This allows the model to better define boundary-layer processes, such as diurnal heating, low-level winds, turbulence, low-level moisture and static stability. It eliminates the problem of vertical coordinate intersecting the ground, unlike in height or isentropic coordinate systems.

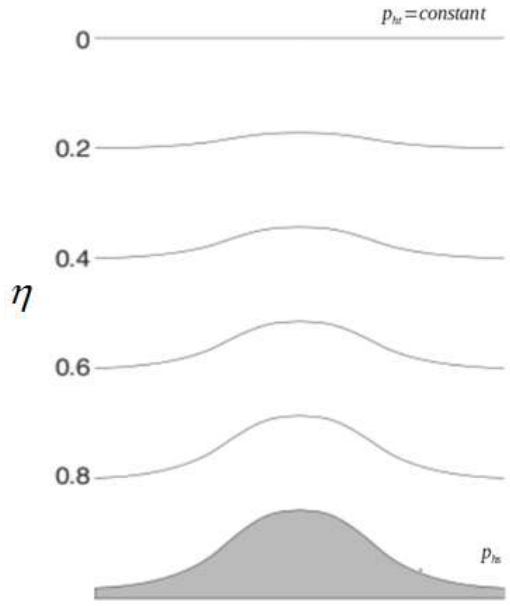

Figure 3: WRF η coordinate showing a terrain-following mass vertical coordinate with a value of 1 at the surface and 0 at the top of troposphere.

Using this vertical coordinate, the flux-form Navier-Stoke equations used in the model are:

$$\frac{\partial U}{\partial t}+\left(\nabla\cdot\mathrm{V}\,u\right)+P_x\left(p,\varphi\right)=F_U \tag{7}$$

$$\frac{\partial V}{\partial t}+\left(\nabla\cdot\mathrm{V}\,v\right)+\mathrm{P}_y\left(p,\varphi\right)=F_V \tag{8}$$

$$\frac{\partial W}{\partial t}+\left(\nabla\cdot\mathrm{V}\,w\right)+\mathrm{P}_\eta\left(p,\mu\right)=F_W \tag{9}$$

$$\frac{\partial \Theta}{\partial t}+\left(\nabla\cdot\mathrm{V}\,\theta\right)=F_\Theta \tag{10}$$

$$\frac{\partial \mu}{\partial t}+\left(\nabla\cdot\mathrm{V}\right)=0 \tag{11}$$

$$\frac{\partial \varphi}{\partial t}+\mu^{-1}\left[\left(\nabla\cdot\mathrm{V}\,\varphi\right)-gW\right]=0 \tag{12}$$

$$\frac{\partial Q_m}{\partial t}+\left(\nabla\cdot\mathrm{V}\,Q_m\right)=F_{Q_m} \tag{13}$$

The pressure gradient terms in momentum equations are given by,

$$\mathrm{P}_x\left(p,\Phi\right)=\left(\alpha/\alpha_d\right)\left[-\partial_x\left(p\phi_\eta\right)+\partial_\eta\left(p\phi_x\right)\right] \tag{14}$$

$$\mathrm{P}_y(p,\Phi)=(\alpha/\alpha_d)\left[-\partial_y(p\phi_\eta)+\partial_\eta(p\phi_y)\right] \tag{15}$$

$$\mathrm{P}_x(p,\mu)=-gm^{-1}\left[(\alpha/\alpha_d)p_\eta-\mu\right]. \tag{16}$$

where $m(x,y)$ represents the mass of dry air per unit area within the column in the model domain at (x,y), hence the flux form variables are defined as:

$$U=\mu u/m, V=\mu v/m, W=\mu w/m, \Omega=\mu\dot{\eta}\Big/m, \Theta=\mu\theta/m.$$

where, m is the map-scale factor that maps the equations to the sphere. To transform the governing equations, map scale factors Δx and Δy are defined as the ratio of the distance in computational space to the corresponding distance on the earth's surface:

$$(m_x,m_y)=\frac{(\Delta x,\Delta y)}{\text{distance on earth}} \quad . \tag{17}$$

The solver supports four projections to the sphere: the lambert conformal, polar stereographic, mercator, and latitude-longitude projections [*Haltiner and Williams*, 1980]. These projections use map factors. Computationally, grid lengths Δx and Δy are constants. However, the physical distances between grid points in

the projection vary with position on the grid. We use mercator projection in our simulations.

The velocities $\mathrm{V} = \mu \mathrm{v} = (u, v, w)$ are the physical velocities in two horizontal and one vertical direction. $w = \dot{\eta}$ is the transformed 'vertical' velocity, θ is the potential temperature and Θ coupled potential temperature.

$Q_m = \mu q_m$; $Q_m = Q_v, Q_c, Q_i, \ldots$, represent the mass of water vapor, cloud, rain, etc. q_* is the mixing ratio (mass per mass of dry air); $\phi = gz$ (the geopotential), p (pressure), and α_d is the specific volume of the dry air, and $\alpha = 1/\rho$ is the specific volume that includes all moist species, i.e. $\alpha = \alpha_d (1 + q_v + q_c + q_i \ldots)^{-1}$.

To close the system, the diagnostic relation for the specific volume is given by the hydrostatic relation for dry air,

$$\phi_\eta = -\alpha_d \mu, \tag{18}$$

and the moist equation of state: is given by,

$$p = p_0 \left(R_d \theta \left(1 + \left(R_v / R_d \right) q_v \right) / \, p_0 \alpha_d \right)^\gamma \tag{19}$$

where $\gamma = c_p / c_v = 1.4$ is the ratio of the heat capacities for dry air, R_d is the gas constant for dry air, and p_0 is the reference pressure (typically 10^5 Pascals). The right-hand-side terms F_U, F_V, F_W and F_Θ represent forcing terms arising from

model physics, turbulent mixing, spherical projections, and the earth's rotation. Thus, we include all the processes that we can resolve or parameterize. Also, the fine structures always appear with increasing resolution. Resolving these small structures is a primary reason for increasing spatial resolution. The solver has the ability to correctly represent structures at the resolution limits (approximately $6\Delta x - 10\Delta x$).

Production of rainfall

Precipitation is a result of moist convection. Moist convection is the key process in regulating the water vapor in the atmosphere, which provided the largest feedback for climate change. Moist convection is divided in two categories: deep convection and shallow convection. Deep convections are lofty vertical moist towers of water vapor with strong updraft motion in troposphere that produces precipitation, and then warms & dries the atmosphere. Shallow convections are not deep enough for precipitation processes to play a major role in cloud development. They are weak vertical velocity towers that do not produce precipitation, warming or drying as water is not removed from atmosphere. Since, individual moist convection happens at a very small scale (25-1000 m), it is computationally impossible to represent these processes on the grids of most numerical weather prediction models [*Stensrud*, 2007]. Production of rainfall is analogical to *squeezing a wet towel*, wherein it causes water to fall out. Likewise, the drier the air, more height it needs to make clouds and rain. Thus, the atmosphere needs to be unstable for convection to happen and ultimately produce

rainfall. If there is little amount of moisture in boundary layer, which is not enough for atmosphere to lead to a convective unstable profile, then atmosphere will remain stable and vice-versa. At some point the moisture convergence and vertical temperature due to heating of surface gets high enough that entire column becomes moist and unstable. The instability results in latent heat release that is produced from condensation in mid and upper levels of atmosphere. This latent heat release reduces the density in upper levels, produce rainfall and restore stability [*Marshall and Plumb*, 2008]. We will use a convective scheme based on this principle by *Kain and Fritsch* [2004].

2.2 Model Discretization

The spatial discretization in the ARW solver uses Arakawa C-grid staggering with 2^{nd}- to 6^{th}-order advection options in horizontal and vertical. The ARW solver advances in time using a time-split integration scheme. The model uses a third-order Runge-Kutta (RK3) time integration scheme. The RK3 time step is limited by the advective Courant number $u\Delta t/\Delta x$ and the user's choice of advection schemes. WRF offers an option to choose from 2^{nd} to 6^{th} order discretizations for the advection terms. The time-step limitations for 1-D advection in the RK3 scheme using these advection schemes are given in *Wicker and Skamarock* [2002].

For stability, the time step used in the ARW should produce a maximum Courant number less than that given by theory. Thus, for 3-D applications, the time step should satisfy the following equation:

$$\Delta t_{\max} < \frac{C_{r_{theory}}}{\sqrt{3}} \cdot \frac{\Delta x}{u_{\max}} \tag{20}$$

Given additional constraint from the time splitting, and to provide a safety buffer, we usually choose a time step that is approximately 25% less than that given by above equation. This time step is typically a factor of two greater than that used in leapfrog-based models. Figure 4 shows different horizontal and vertical grid configurations of WRF model.

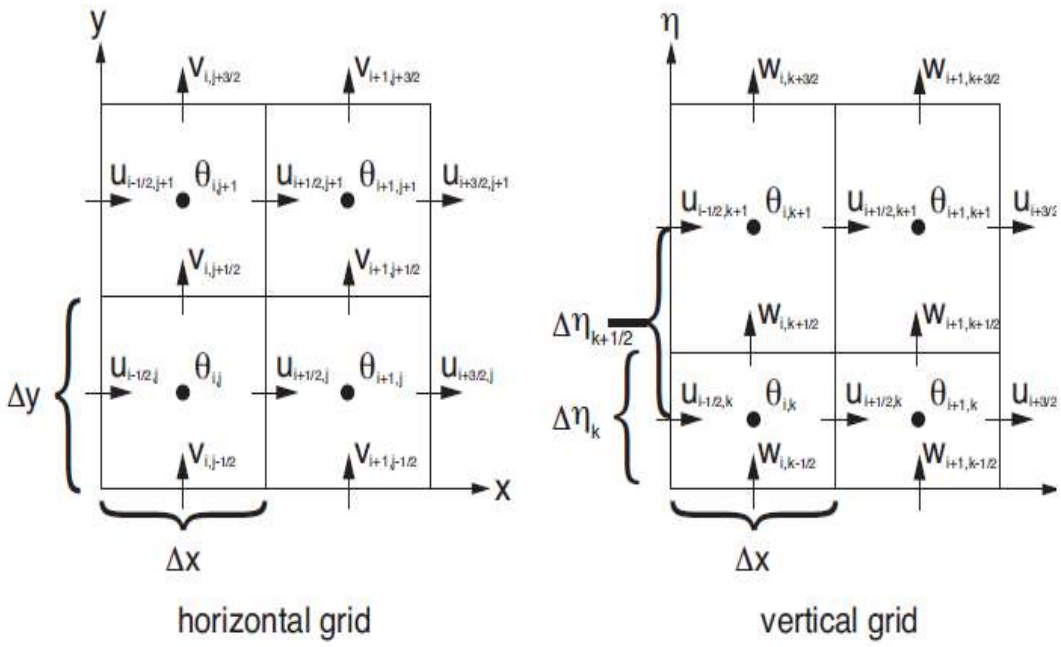

Figure 4: Horizontal and vertical grids of the ARW with scalars in the center of grid box and vectors at the center of edges.

For ARW the time-step configuration constraint is determined by the smallest physical horizontal grid spacing, $\min\left(\Delta x / m_x, \Delta y / m_y\right)$.

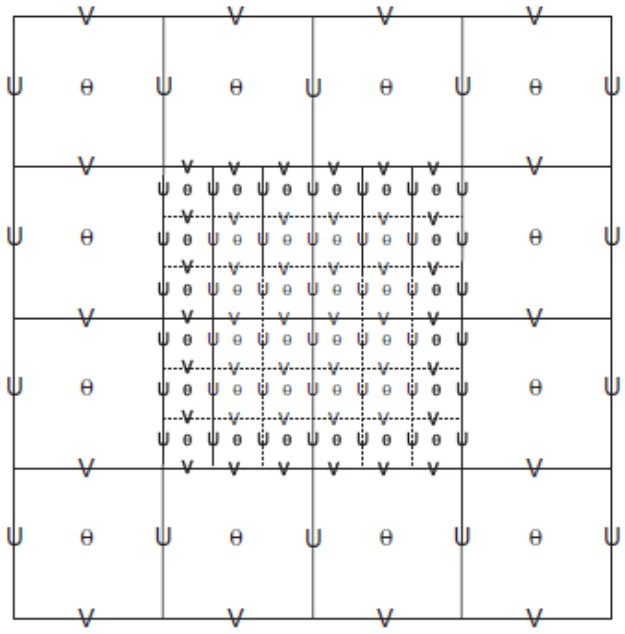

Figure 5: Illustration of typical nesting in ARW model: Here a 3:1 embedded nest is shown. Scalar temperature is calculated at the center of grid box and velocities at the center of sides.

Figure 5 shows the illustration of Arakawa-C staggered grid for a parent domain with an imbedded nest domain with a 3:1 grid size ratio. The solid lines denote coarse grid cell boundaries for the parent domain, and the dashed lines are the boundaries for each fine grid cell of the child domain. The horizontal components of velocity $(U \text{and} V)$ are defined along the normal cell face, and the thermodynamic variables (θ) are defined at the center of the grid cell.

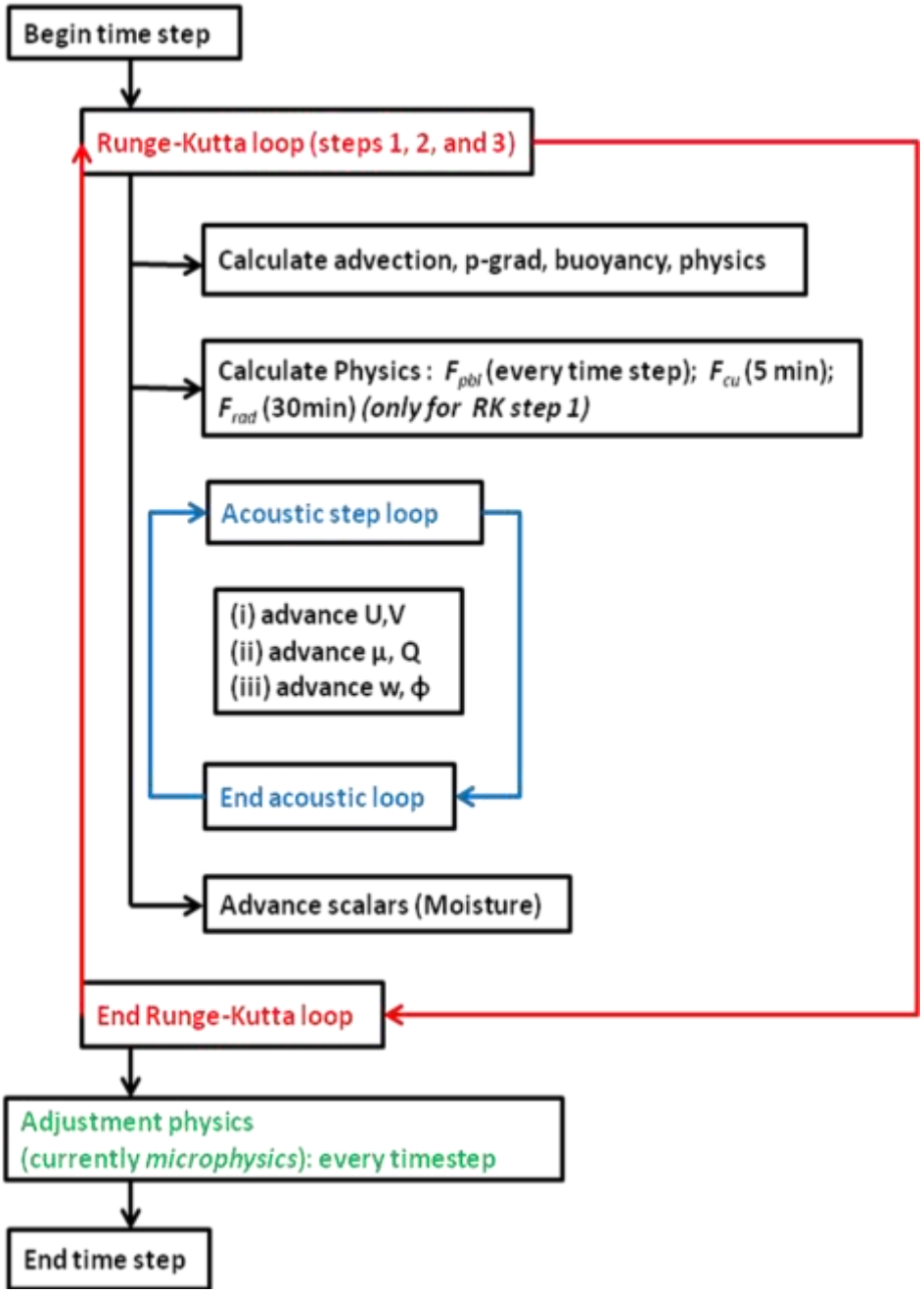

Figure 6: A flowchart showing the steps followed in the WRF model for a time step computation and instances when and where physics is called during a time step.

2.3 WRF system

WRF runs with user-defined initial and boundary conditions. WRF utilizes WPS (WRF Preprocessor System) that transforms the large terrestrial and meteorological data available online on global grid resolution as an input to WRF model for real cases. Steps for this procedure are as follows: Firstly, we define a physical grid (including the projection type, location on the globe, number of grid points, nest locations, and grid distances) and interpolate static fields to the prescribed domain. Secondly, we convert the metrological data to the desired format required for the selected domain. Thirdly, after specifying the domain with the required parameters, WPS horizontally interpolates the meteorological data onto the projected domain(s). The program METGRID from WPS presents a complete 3-dimensional dataset of variables on the selected model grid's horizontal staggering at the selected time slices, which is sent to the ARW pre-processor program for real-data cases.

The input to the ARW real-data processor from WPS contains 3-dimensional fields (including the surface) of temperature (K), relative humidity (and the horizontal components of momentum (m/s, already rotated to the model projection). The 2-dimensional static terrestrial fields include: albedo, Coriolis parameters, terrain elevation, vegetation/land-use type, land/water mask, map scale factors, map rotation angle, soil texture category, vegetation greenness fraction, annual mean temperature, and latitude/longitude. The 2-dimensional time-dependent fields from the external model, after processing by WPS, include: surface pressure and sea-level pressure (Pa), layers of soil temperature (K) and

soil moisture (kg/kg, either total moisture, or binned into total and liquid content), snow depth (m), skin temperature (K), sea surface temperature (K), and a sea ice flag. Figure 7 shows a schematic flowchart of the steps followed in WRF code. In the Runge-Kutta 3 (RK3) [*Wicker and Skamarock*, 2002] scheme, physics is integrated within the RK3 time integration. Within the acoustic integration, the acoustic time step $\Delta\tau$ is specified by the user. The efficiency of the RK3 timesplit scheme arises from the fact that the RK3 time step Δt is much larger than the acoustic time step $\Delta\tau$, hence the most costly evaluations are only performed in the less-frequent RK3 steps.

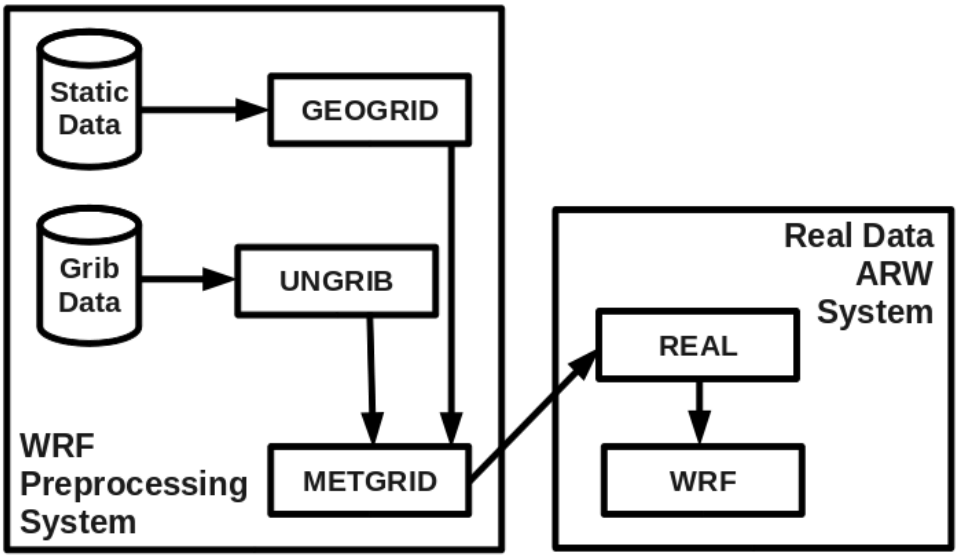

Figure 7: Schematic showing the data flow and program components in WRF.

To conclude, we will use WRF Model with multiple nesting, configuring the innermost domain to cover the desired domain in consideration. The readers are referred to *Skamarock et al.* [2008] for further details on WRF.

Chapter 3

3. ARIZONA STUDY: PART 1

3.1. Background

As discussed in Chapter 1, global climate models have a coarse resolution of *O*(100 km). At that resolution, most of the rainfall is produced by subgrid-scale convective parameterization with a very crude representation of surface heterogeneity within a grid box. While those models have produced meaningful projections of large-scale hydrological conditions in future climate [e.g., *Seager et al.*, 2007; *Mariotti et al*., 2008], they do not have the capacity to predict local climate changes at the mesoscale especially for regions characterized by complicated terrain. A complementary approach of *climate downscaling* has been developed that uses large-scale boundary conditions to constrain a mesoscale model for long-term, regional climate prediction [e.g., *Giorgi et al*., 2001; *Leung et al*., 2003; *Lo et al*., 2008]. The increased model resolution allows an increase in the fraction of grid-scale precipitation and reduction of parameterized subgrid precipitation. This, combined with a refined representation of topography and surface heterogeneity, might help improve the realism of simulated precipitation [e.g., *Giorgi and Marinucci*, 1996; *Leung et al*., 2003; *Kim*, 2004; *Duffy et al*., 2006; *Duliere et al*., 2011]. State-of-the-art climate downscaling studies for seasonal and longer time scales have so far adopted a horizontal resolution within the range of 12-50 km [e.g., *Knutson et al.*, 2007; *Rockel et al.*, 2008; *Caldwell et al*., 2009; *Bukovsky and Karoly*, 2009; *Urrutia and Vuille*, 2009; *Raucher et al.*,

2010; *Duliere et al.*, 2011]. On the other hand, previous studies that adopted a higher resolution (e.g., 3 km) to determine the sensitivity of rainfall on model resolution and convective parameterization are mostly restricted to short-term weather prediction [e.g., *Gilliland and Rowe*, 2007; *Mercader et al*., 2007]. To bridge this gap of knowledge, this study will explore the changes in rainfall in seasonal climate downscaling simulations when the horizontal resolution of the regional model is refined from 12 km to 3 km. As will be demonstrated shortly, grid-scale precipitation becomes the dominant contributor to the total rainfall at these scales. Given so, we will also test the sensitivity of simulated rainfall to the switching on and off of cumulus parameterization. The main purpose of simulations is two-fold: First, to determine the numerical sensitivity of the seasonal mean rainfall when the resolution of the model is successively refined to the nearly cloud-resolving scale of 3 km. Secondly, if a numerical sensitivity produces a converge, to examine whether the solution converges to the observed seasonal mean climatology.

We choose to perform the numerical simulations for the winter season in Arizona, a region with dramatic contrasts in topography and local rainfall patterns [*Sellers,* 1960; *Woodhouse,* 1997; *Sheppard et al.*, 2002] that provide an ideal test ground for the impact of model resolution. We choose winter because numerical models, whether global or regional, are widely known to produce substantial biases in North American summer monsoon [e.g., *Collier and Zhang*, 2007; *Lin et al*., 2008], while their performance for wintertime precipitation is generally more robust. Also, wintertime precipitation plays an important role in water resource

management till spring season. While the summertime bias is itself an important issue, it might prove to be a distraction in the context of our sensitivity study. Regional climate simulations using the Weather Research and Forecast (WRF) model [*Skamarock et al*., 2008] will be performed over seven winter (November-January) seasons. The dependence of the climatology as well as high-frequency behavior of simulated rainfall on model resolution and/or subgrid-scale convective scheme will be analyzed. To maintain focus, the analysis will focus on liquid-form precipitation, leaving the complexity of snowfall to later work.

3.2 Objectives

This study will investigate the impact of resolution on precipitation through climate downscaling for long winter season simulations (Nov-Jan) for seven years for Arizona to get small-scale climatology at a critical scale (6 km) beyond which rainfall becomes explicitly resolved and study the sensitivity of seasonal rainfall on model resolution. Our study will refine the horizontal grid size to a partially cloud-resolving 3 km, which has not been done before in the context of seasonal downscaling for Arizona. As we approach this resolution, the cumulus parameterization scheme begins to lose its validity. We will therefore perform experiments with the cumulus scheme switched on and off as another sensitivity test. This research provides a detailed analysis and an insight to improve the understanding of climate simulations of the region that has strong footprints of interactions between atmospheric circulations and topography.

3.3 Model and numerical experiments

We will use Weather Research and Forecast (WRF) [*Skamarock et al*., 2008] Model Version 3.1, a non-hydrostatic mesoscale model that allows multiple nesting. The model grids are configured such that the innermost domain covers the State of Arizona while the outermost domain covers the entire western U.S. (see Figure 8). In between, two- or three-layer nesting is adopted with the large-scale boundary condition imposed at the lateral boundary of the outermost domain only. We will not apply interior nudging. The time-varying large-scale boundary condition is constructed from 6-hourly NCEP Global Analysis (FNL) data (from the NCAR CISL Data Support Section archive, http://dss.ucar.edu/datasets/ds083.2) on 1 deg x 1 deg grid. Hourly outputs are saved for all runs to help the analysis of high-frequency behavior and extreme events of rainfall.

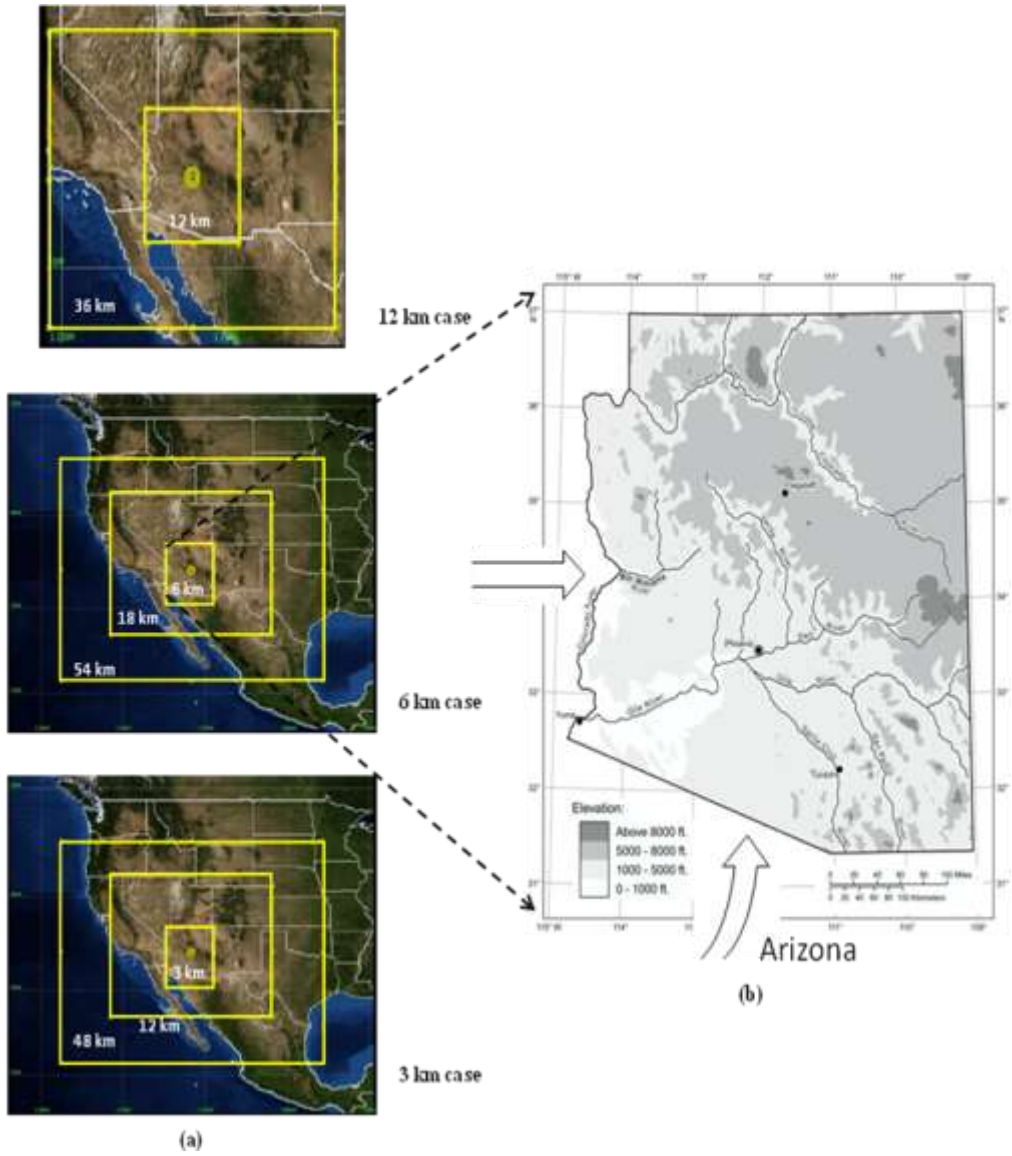

Figure 8: The model domains and arrangement of nesting for the numerical experiments: (a) nested domains for WRF model, (b) An illustration that the innermost domain covers the State of Arizona; The arrows indicate the prevailing directions of moisture fluxes into Arizona in wintertime [*Sellers*, 1960]. The topographic map is taken from Arizona Geographic Alliance, Arizona State University (http://geoalliance.asu.edu/azga).

The horizontal grid size for the innermost domain is varied from 12 km to 6 km, then to 3 km. Hereafter, unless otherwise noted, the "model resolution" in our discussion refers to the grid size of the innermost domain. The 12 km runs are carried out with two layers of nesting, using 36 km resolution for the outer domain. The 6 km and 3 km runs adopt a 3-layer nesting using (54 km, 18 km) and (48 km, 12 km) as the resolutions for the outermost and intermediate domains, respectively. Detail of the nesting is shown in Figure 8. At 12 km resolution, subgrid-scale cumulus convective scheme is turned on. As the parameterized convective rainfall diminishes with an increasing resolution, at 6 km resolution we perform a pair of experiments, one with convective scheme turned on and another with it turned off. (This is for the innermost domain only. Cumulus parameterization is always turned on for the intermediate and outermost domains.) Convective scheme is turned off at 3 km resolution. Whenever convective parameterization is retained, we choose Kain-Frisch scheme [*Kain*, 2004]. Table 1 summarizes the horizontal resolution and arrangement of nesting for our major experiments. For the two cases in Table 1 that eliminate cumulus convective parameterization, all rainfall is produced by grid-scale processes.

Table 1: A summary of the horizontal resolution and arrangement of nesting for four sets of simulations performed in this study. Also indicated in the table is whether cumulus parameterization is turned on or off.

Nesting	**Resolution**			**Cumulus convective parameterization (Kain-Frisch scheme)**
	Outermost domain	**Intermediate domain**	**Innermost domain**	
2 layer	36 km	---	12 km	**ON**
3 layer	54 km	18 km	6 km	**ON**
				OFF
3 layer	48 km	12 km	3 km	**OFF**

To ensure proper resolution of topography and surface characteristics that matches the increase in model resolution, we use USGS 24 classification categories of land-use data for interpolating topography and land surface characteristics (from standard *geogrid* package in WRF) at different spatial resolutions for different levels of nesting: We use 10', 5', and 2' geogrid resolution for the outermost, intermediate, and innermost model domains, respectively. The model has 28 levels in the vertical with the model top set at 50 hPa. For other physical parameterization schemes, we selected (from WRF's available options)

Single-Moment (WSM) 3-class simple ice scheme for microphysics; Dudhia scheme for shortwave and Rapid Radiative Transfer Model (RRTM) scheme for longwave radiation; Monin-Obukhov Similarity scheme for surface-layer process. The YSU scheme is used for boundary layer mixing and Thermal Diffusion is chosen for land surface process.

Each of the 4 cases in Table 1Table 1 consists of seven 92-day continuous runs for the 7 winter seasons (November-January) from 2003-2009. (Winter 2009 refers to November 2009-January 2010.) Sea Surface Temperature is updated daily and is provided from FNL data. As explained in Introduction, winter is chosen because the model generally simulates the climatology of the cold season more accurately than the warm season. Note that for water resource applications, wintertime rainfall is particularly important over the semi-arid part of Arizona, where rainfall in summer is quickly recycled back to the atmosphere due to intense evaporation [e.g., *Bryson and Hare*, 1974].

To compare the WRF simulations of winter seasonal rainfall with observation, we will use the PRISM (Parameter-elevation Regressions on Independent Slopes Model, data archive available at http://www.prism.oregonstate.edu) monthly mean precipitation dataset. It is consolidated from station measurements with spatiotemporal interpolations [*Daly et al.*, 2000; *Gibson et al.*, 2002) and is the official climatological rainfall data of USDA.

3.4 Results

3.4.1 Seasonal cumulative rainfall

We first analyze the simulated rainfall based on two variables, RAINC and RAINNC, from the WRF model output. The former is the rainfall produced by cumulus parameterization and the latter is the rainfall produced by grid-scale processes, including mechanical lifting and adjustment of thermodynamic profile at grid scale. Figure 9a and b show the seven-winter mean of November-January cumulative rainfall produced by parameterized subgrid-scale convection and grid-scale processes, respectively, from the 12 km run. At this resolution, grid-scale rainfall is already the dominant contributor to the total rainfall, in comparison to coarse resolution global climate models for which the precipitation generated by subgrid-scale convective scheme is comparable to grid-scale precipitation. The maximum of rainfall over central Arizona (along the Mogollon Mountains) in both panels reflects topographic influence. A maximum of rainfall just south of U.S.-Mexican border (at the bottom edge of the plot) in Figure 9a is due to the fact that that particular spot is over the water (Gulf of California). Note that in this study we do not analyze snowfall, which is otherwise substantial over areas with high altitude in northern Arizona.

Figure 9c and 9d are similar to Figure 9a and 9b but for the simulations with 6 km resolution that retained cumulus convective parameterization. The refinement of resolution from 12 to 6 km leads to a further decrease of the relative contribution of the subgrid-scale convective rainfall as expected. Interestingly,

the total rainfall (RAINC+RAINNC) increases with resolution, as further shown in Figure 10a (total rainfall at 12 km resolution) and Figure 10b (6 km resolution). This increase occurs not only over the central mountain range of Arizona but also over southern Arizona where the mountains are shorter, more scattered, and with smaller scales (therefore the increased resolution leads to enhanced effects of those mountains on rainfall).

Given the diminished contribution of parameterized subgrid-scale convection to the total rainfall at 6 km resolution, we next experiment with an identical set of runs but with cumulus convective scheme turned off. The total winter seasonal rainfall (that comes entirely from RAINNC) for this run is shown in Figure 10c. It is found that eliminating the convective parameterization only very slightly affects the total rainfall. (The case with RAINC=0 produced even a slightly greater amount of total rainfall.) Without cumulus parameterization, grid-scale rainfall (RAINNC) was enhanced to compensate for the absence of subgrid-scale convection. This behavior is qualitatively understandable since, given the large-scale moisture convergence, a certain amount of rainfall is anticipated in order to restore static stability and maintain water balance. Without cumulus parameterization, grid-scale processes do all the work to produce this amount of rainfall.

With the insight from the two sets of 6 km runs, we then executed the 3 km runs without cumulus parameterization. Figure 10d shows the total winter rainfall from this set of runs. The increase of horizontal resolution from 6 to 3 km leads to a relatively smaller change in the total rainfall for Arizona, compared to

the change from 12 to 6 km (this will be quantified in the discussion related to Figure 14). The 3 km run does produce a few spots of intense rainfall over the mountain range in central Arizona that are not as pronounced in the 6 km runs. In addition, at 3 km resolution one begins to notice northwest-southeast oriented "streaks" in the rainfall pattern, which likely reflect the effects of the fine-scale topography in that region. The substantial increase in regional rainfall from 12 to 6 km cases underscores the sensitivity of seasonal rainfall simulation to model resolution. From 6 to 3 km the total simulated rainfall begins to convergence (as will be more clearly demonstrated in Figure 14). We should next examine whether they converge to the observed climatology.

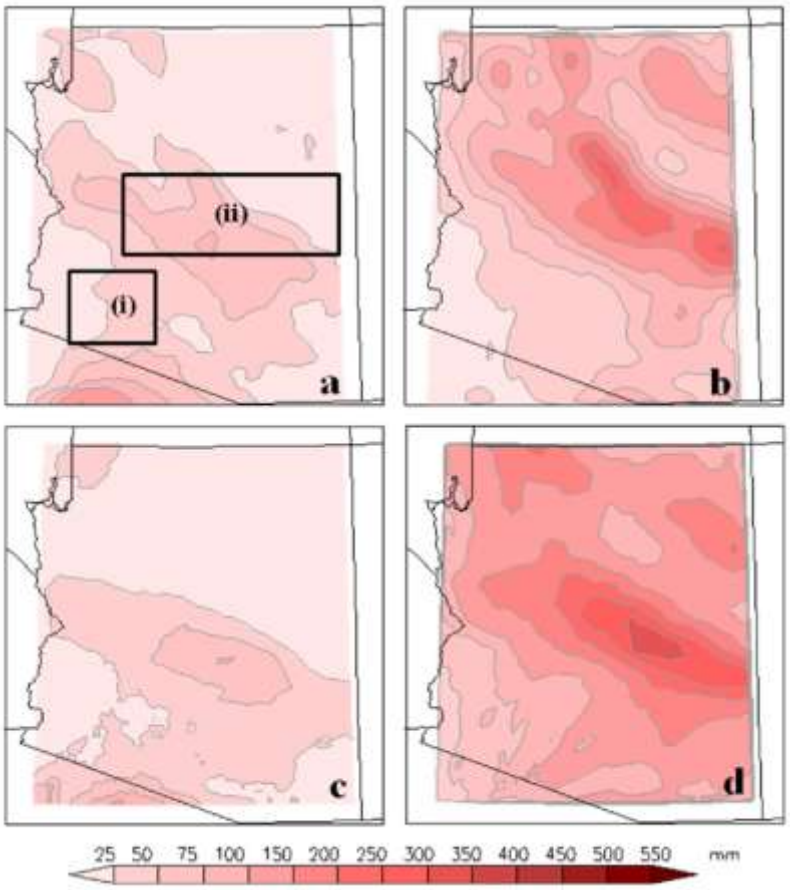

Figure 9: The cumulative rainfall for winter season (November 1 – January 31), averaged over 7 winters from 2003 to 2009, from different sets of runs. (a) Rainfall produced by subgrid-scale cumulus parameterization (RAINC) from the 12 km runs. (b) Rainfall produced by grid-scale convection (RAINNC) from the 12 km runs. (c) RAINC from the 6 km runs with cumulus parameterization turned on (d) RAINNC from the 6 km runs with cumulus parameterization turned on. Boxes (i) and (ii) in panel (a) are the areas chosen for the further analysis of the time-series of rainfall in Figs. 5-7. Box (i) is defined as 111.78^{o}W-113.61^{o}W and 31.90^{o}N-33.69^{o}N and box (ii) defined as 109.35-112.02^{o}W and 33.25^{o}N-35.18^{o}N.

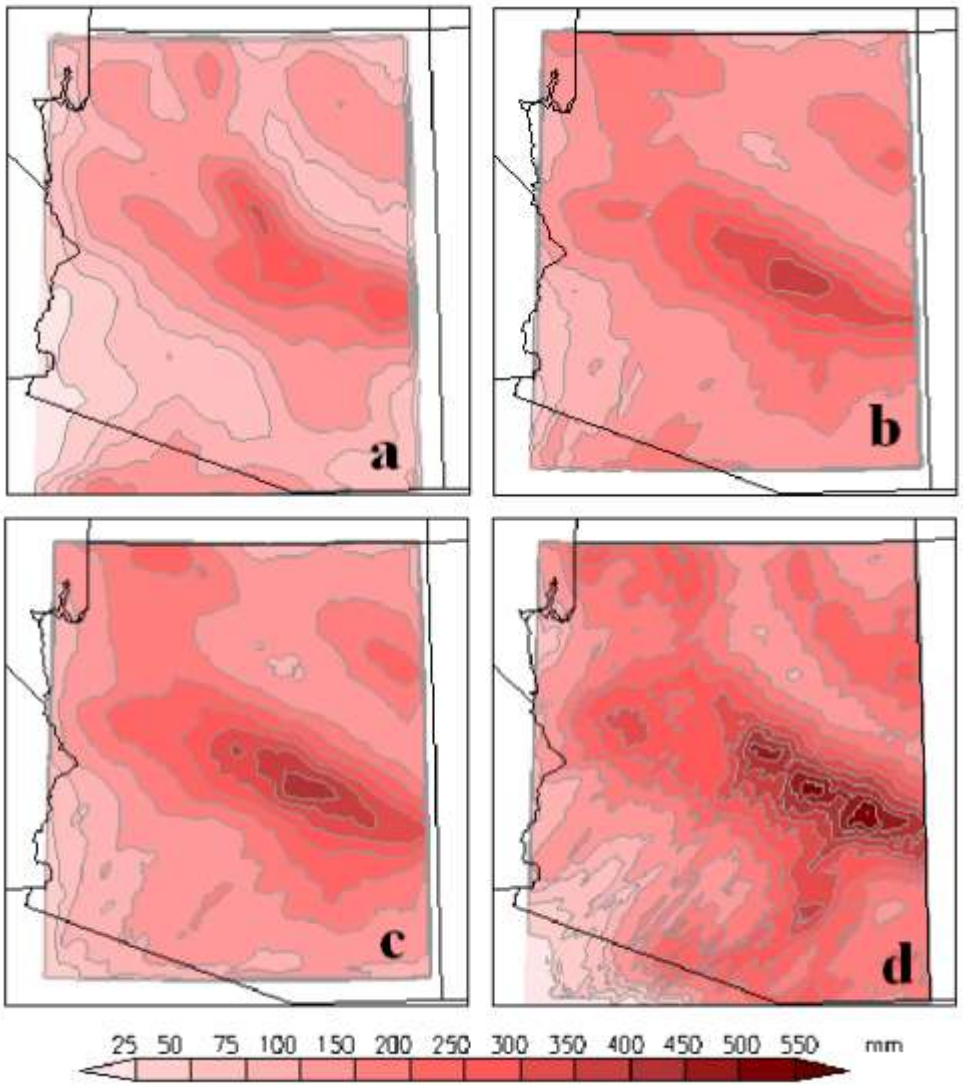

Figure 10: Same as Figure 9 but for different runs or combinations of variables for rainfall. (a) Total rainfall (RAINC+RAINNC) from the 12 km runs. (b) Total rainfall (RAINC+RAINNC) from the 6 km runs with cumulus parameterization turned on. (c) Total rainfall (all produced by grid-scale convection, RAINNC) from the 6 km runs with cumulus parameterization turned off. (d) Total rainfall (RAINNC) from the 3 km runs.

3.4.2 Effect of changes in time step size

The tests of numerical sensitivity and convergence have been significantly expanded to include experiments on changing the time step size. After examining the effect of the model grid refinement, a set of new runs for testing numerical convergence with a reduced time step is performed at a 3 km grid resolution. In these runs the time step size was changed from 288 to 144 seconds. Figure 11 shows the changes in winter seasonal rainfall by halving *dt* for two contrasting years of 2006 (Arizona just recovered from a drought in 2006) and 2009. The results generally assure that (for the range of time step size we use) the dependence of the simulated seasonal rainfall on *dt* is weak. The impact of changing *dt* on the frequency and intensity of extreme rainfall hourly amounts remains to be analyzed.

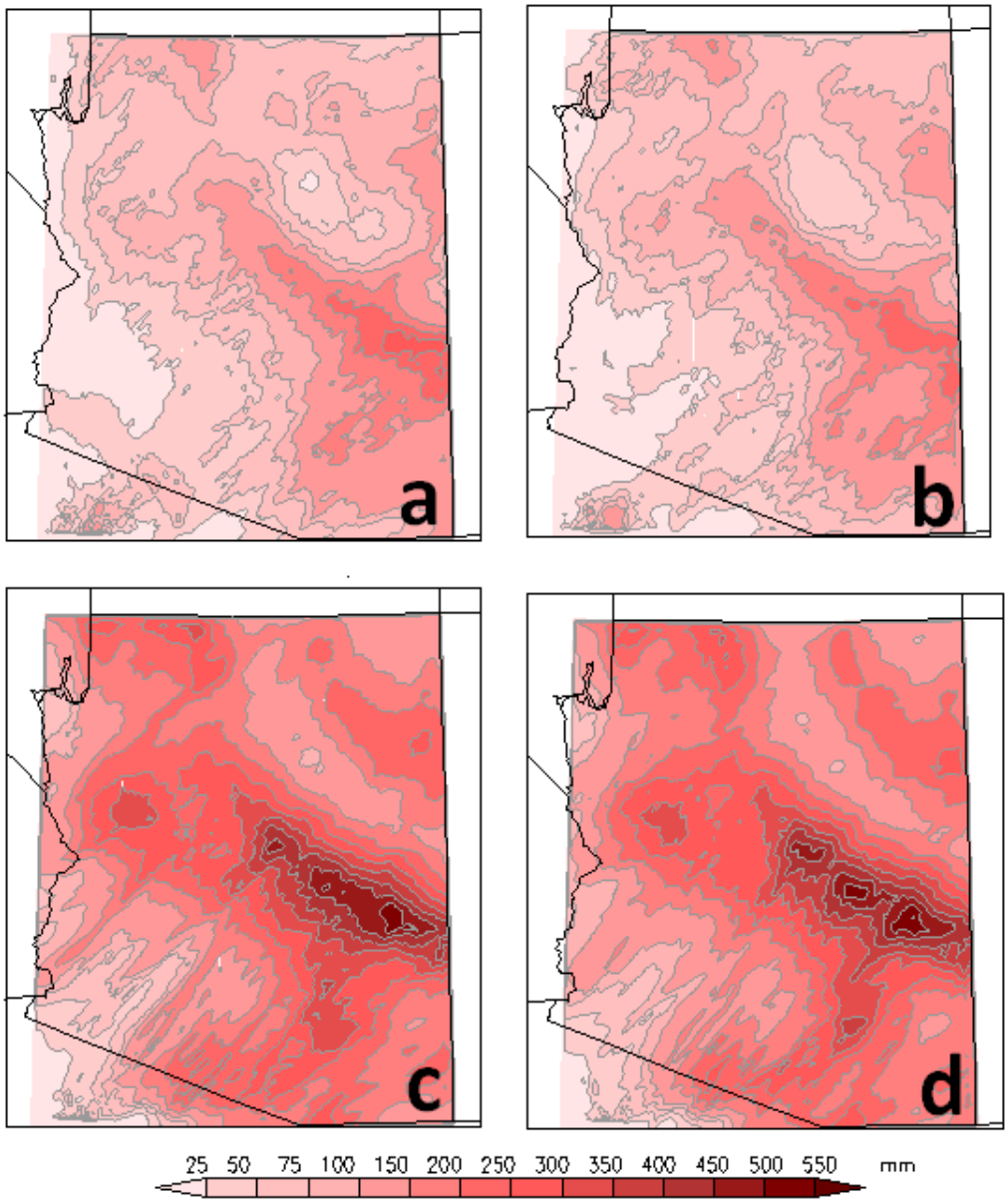

Figure 11: The cumulative rainfall for winter season (Nov 1 - Jan 31) for (a) year 2006 with temporal resolution *dt* (where *dt* = 288s), (b) for half the temporal resolution *dt/2*, (c) and (d) are same as cases (a) and (b) but for year 2009.

3.4.3 Isolating the effects of refining grid resolution vs. refining topography

The existing runs with changing horizontal resolution include two effects due to the change of model grid size and the refinement of topography. New experiments are performed to separate these two effects. Figure 12 shows the outcomes of two new runs using the coarser 10' topographic data (interpolated to model grid) in the surface boundary condition for both 6 km and 3 km runs, and compare them to the existing 6 km and 3 km runs with 2' topography. The results indicate that the effect of changing the resolution of topography is not negligible (using the 2' topography leads to more "streaks" in the rainfall pattern whose realism remains to be analyzed). Yet, even with a fixed topography the effect of changing the grid resolution alone can explain a large portion of the change in seasonal rainfall from 6 to 3 km resolution in previous simulations.

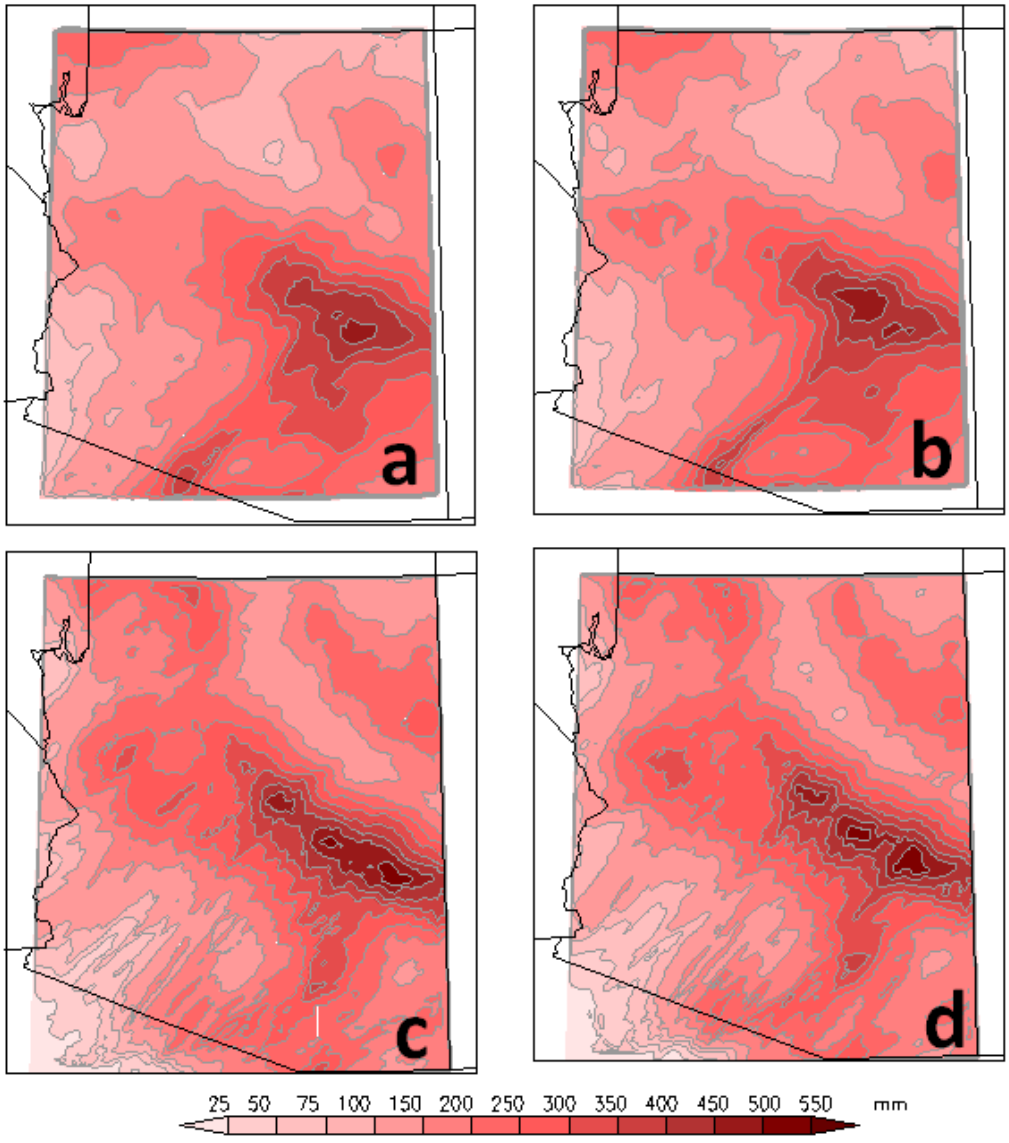

Figure 12: The cumulative rainfall for winter season for year 2009 for (a) 6 km run with 10' resolution, (b) 6 km run with 2' resolution, (c) 3 km run with 10' resolution, and (d) 3 km run with 2' resolution (here resolution refers to topographic not model grid resolution).

3.4.4 Comparison of simulated rainfall with PRISM observations

Figure 13 shows the seven-year average of the winter (November-January) cumulative rainfall from observation that can be used to compare to the model simulations in Figure 9. Figure 14 further compares the simulated year-to-year winter seasonal rainfall at different model resolutions with the corresponding observations. The observations are based on the PRISM dataset [*Daly et al*., 2000; *Gibson et al.*, 2002] of monthly mean rainfall. They are shown in Figure 14 in the leftmost column. The other 3 columns show the simulations with 12, 6, and 3 km resolutions. (For brevity, for the 6 km runs we only show the case with cumulus convective scheme turned off.) This comparison reveals several interesting behaviors of the simulated rainfall. First, the model simulations (at all resolutions) did qualitatively capture the interannual variability of rainfall over Arizona. For example, the model produced a very wet winter for 2004 and a dry winter for 2005 as observed. This is further illustrated in Figure 15, the comparison of the year-to-year domain averaged rainfall with observation (PRISM data) for (a) the entire Arizona, (b) Box (i), and (c) Box (ii) (the two boxes are marked in Figure 9a). In Figure 15a, we have also added the rainfall from coarser resolution runs with 54, 36, and 18 km grids, taken from the outermost or intermediate domains for the major simulations. They are not included in the plots for Box (i) and (ii) because with the coarse resolution the number of grid points within each box is relatively small, rendering the statistics less reliable. Except for the case with the lowest resolution (54 km), all other simulations capture a significant portion of the observed interannual variability of

rainfall. The more notable difference among those runs is actually in the long-term mean, for which the 36 km case matches well with observation while the runs with higher resolutions produce excessive rainfall. A plausible explanation is that 36 km is close to the resolution used by the majority of applications of WRF and likely the resolution used for model validation during the development phase of the model. If the model was previously tuned at around 30 km resolution for its climatology to resemble observation, there is indeed no guarantee that refining (or coarsening, as is the case of 54 km run) the resolution will improve or maintain the simulated climatology. That Figure 15 shows otherwise is an indication that the physical parameterization schemes in the model are not resolution dependent. As surveyed in Introduction, most of the existing climate downscaling experiments have used a horizontal resolution coarser than 12 km. Given our finding, those appear to be sensible choices; We caution against hastily pushing for increasingly higher resolutions without carefully validating the model climatology at those resolutions.

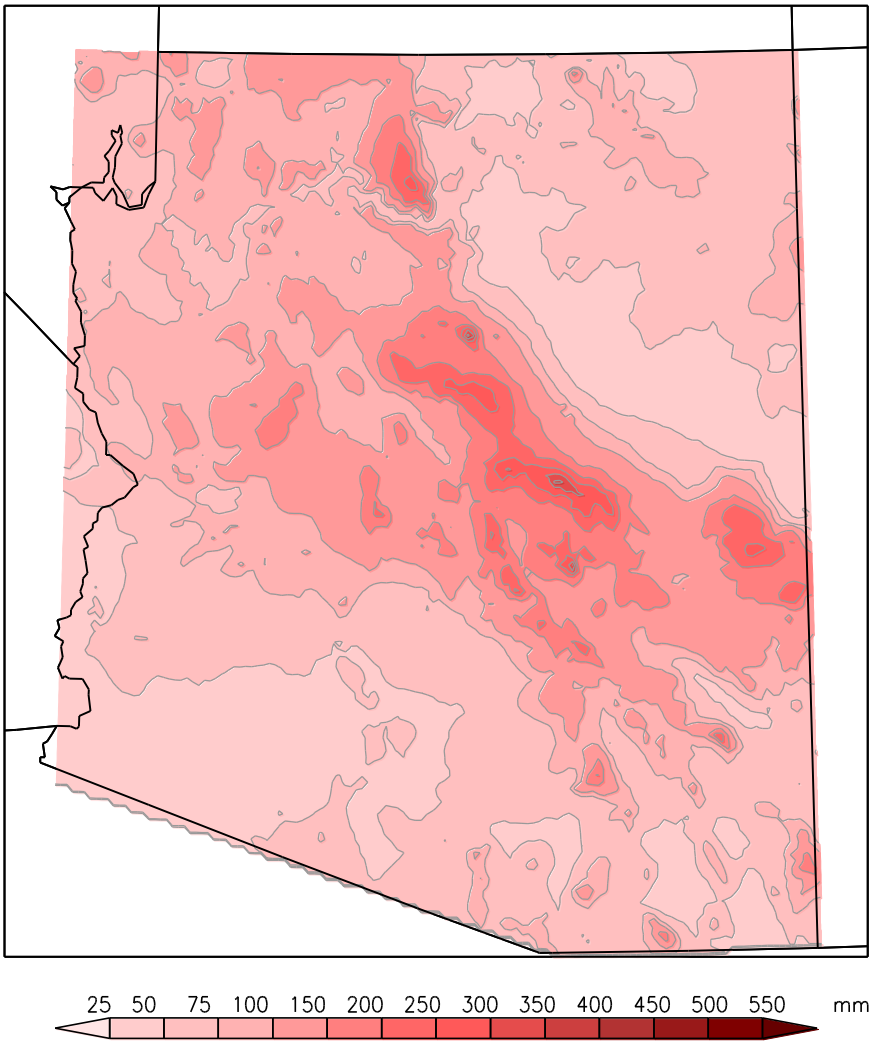

Figure 13: The cumulative observed rainfall for winter season (November 1 – January 31), averaged over 7 winters from 2003 to 2009, using the PRISM monthly data.

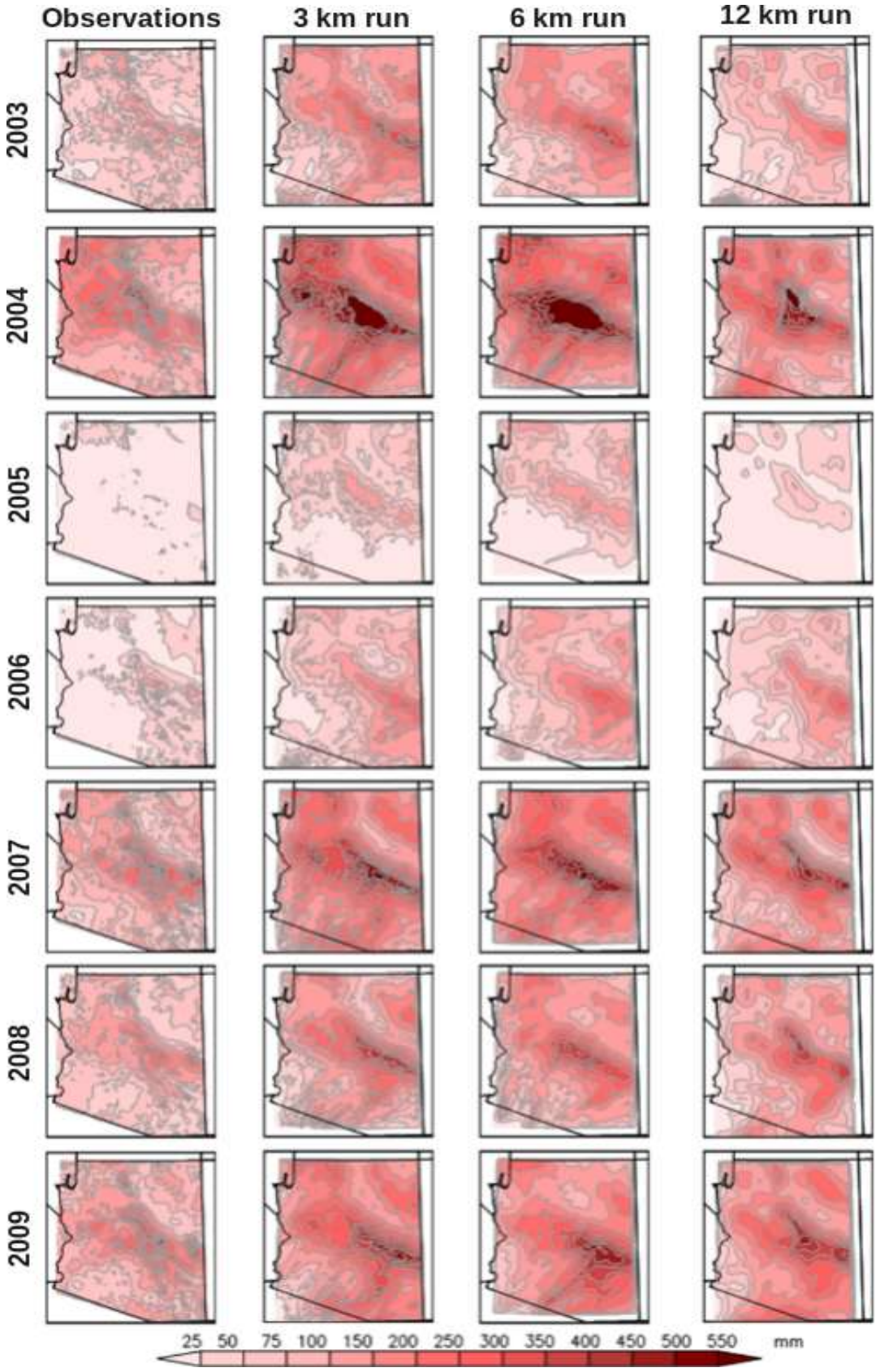
Observations
3 km run
6 km run
12 km run
2003
2004
2005
2006
2007
2008
2009
25 50 75 100 150 200 250 300 350 400 450 500 550 mm

Figure 14: A year-by-year comparison of the simulated winter seasonal-mean rainfall with observation using the PRISM dataset. The 7 winters are arranged from top to bottom. The observation is shown at the leftmost column, followed to the right by the simulations with 3 km, 6 km, and 12 km resolution. For brevity, for the 6 km runs only the case with cumulus convective scheme turned off is shown. The results for the case with convective scheme turned on are similar in pattern and magnitude.

An encouraging aspect of Figure 15 is that it shows the merit of using WRF to simulate interannual variability of rainfall (even without interior nudging, as is the case of our simulations) in the context of climate downscaling. This conclusion is slightly more optimistic than some recent studies [*Rockel et al*., 2008 and discussions therein] that voiced concerns that the amplitude of interannual variability is reduced in climate downscaling especially if the regional model domain is large and interior nudging is turned off. However, this study has used a smaller model domain and a higher horizontal resolution than those adopted by *Rockel et al*. [2008] and related studies. Thus, the finding here is still consistent with the view of *Rockel et al*. that using a smaller domain helps alleviate the problem of the loss of low-frequency variability.

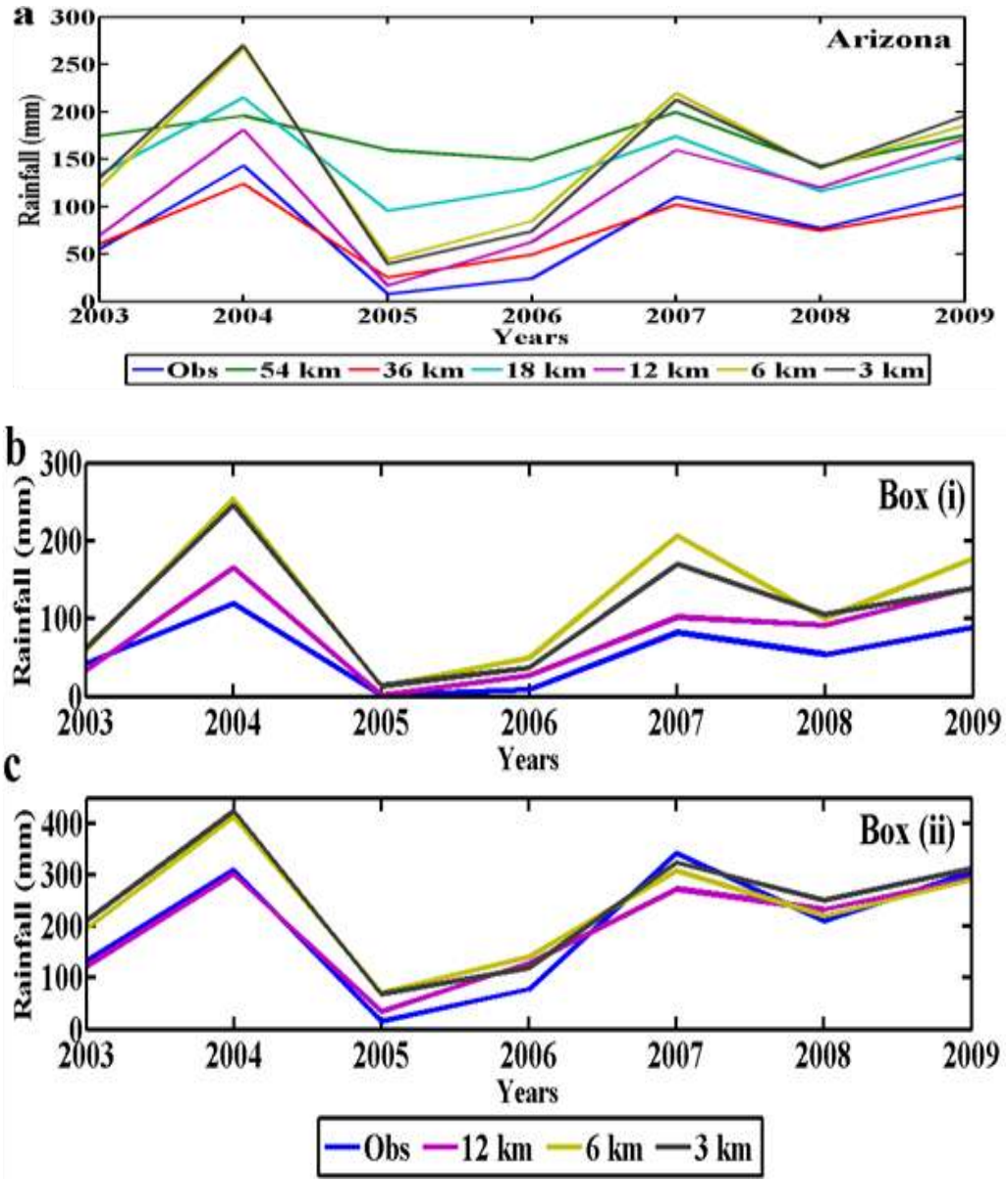

Figure 15: Comparisons of the simulated winter seasonal mean rainfall with observation. Shown are the averages over (a) the entire innermost model domain that covers the State of Arizona; (b) Box (i), and (c) Box (ii) (as marked in Fig. 2a). The observation from PRISM data is in dark blue. The cases for the simulations are labeled in the legends. See text for detail.

3.4.5 Temporal characteristics of rainfall and extreme events

Figure 16 shows the model simulated hourly rainfall for one of the winters, November 2009 - January 2010, for a sub-domain over southern Arizona marked as box (i) in Figure 9a. This box covers a region with relatively flat topography and modest rainfall. Red and blue are the hourly rainfall and cumulative rainfall, respectively. The eight panels in that figure are from the runs with different resolutions, and further separated into subgrid-scale (convective parameterization) and grid-scale rainfall, as detailed in the caption. What is noteworthy here is not the difference, but the similarity, among the eight panels. A significant rainfall event is usually picked up by all runs regardless of their horizontal resolutions (e.g., compare the last four panels); The difference is in the magnitude of rainfall. Also, the time series of the rainfall produced by subgrid-scale convective parameterization (RAINC) is similar to that produced by grid-scale processes (RAINNC), only that the latter has larger amplitude (e.g., compare panel c with panel d). Although we only show the detailed time series for one winter, the characteristics described above are shared by the simulations for the other 6 winters.

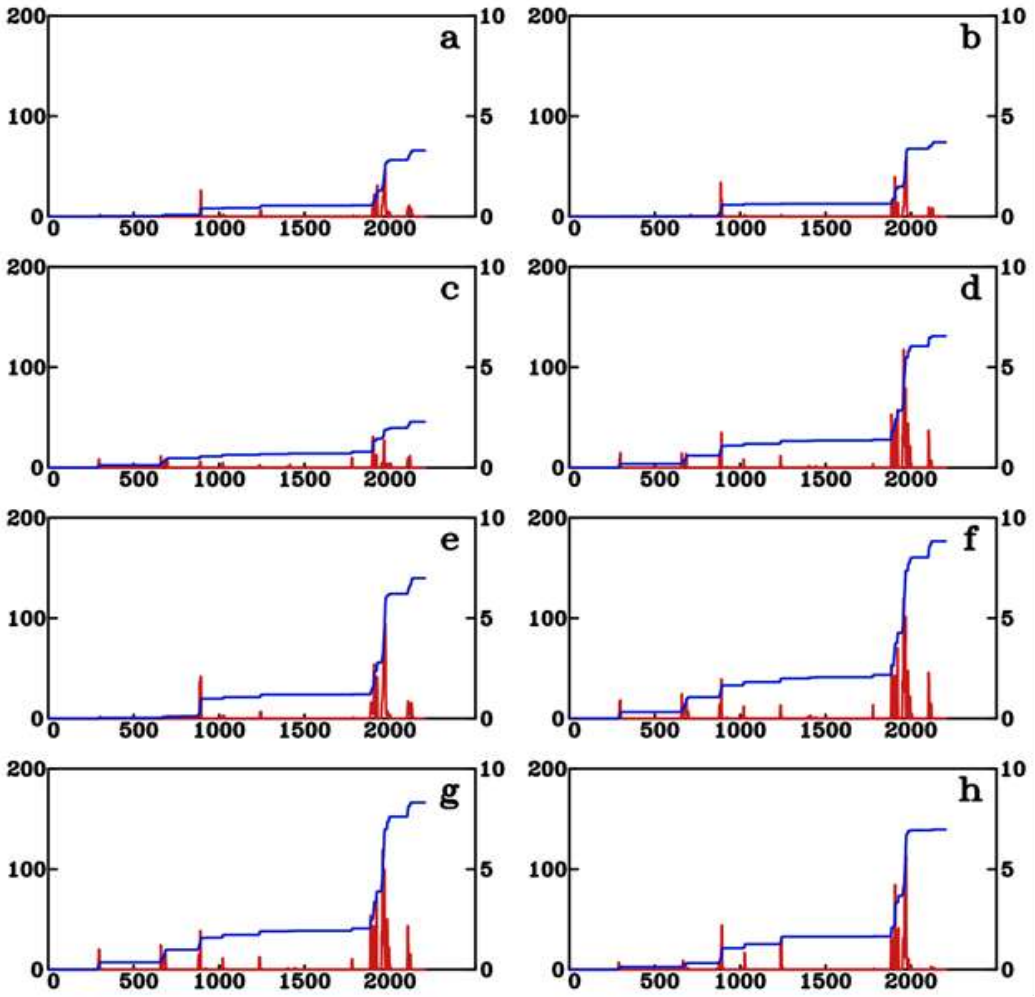

Figure 16: Time-series of hourly rainfall averaged over box (i) in Fig. 2a for 1 Nov 2009 - 31 Jan 2010 for different sets of runs. Red and blue curves are the instantaneous and cumulative rainfall, respectively. The top 4 panels correspond, in the same order, to the 4 panels shown in Fig. 2 (panel a in Fig. 6 corresponds to panel a in Fig. 2, etc.). The bottom 4 panels correspond to the 4 panels in Fig. 3 (panel e in Fig. 6 corresponds to panel a in Fig. 3, etc.) The scale at left, in mm, is for the cumulative rainfall and scale at right, in mm/hr, is for the instantaneous rainfall. Abscissa is time in hours since 00Z, 1 Nov 2009.

Figure 17 compares the hourly rainfall from the 12 km (blue dots) and 3 km (red line) runs for all 7 winter seasons (November-January) from 2003-2009 by stitching the seven 92-day runs together. Figure 17a is for the average over box (i) and Figure 17b for box (ii) as marked in Figure 9a. Figure 17c is the average over the entire Arizona domain. Unlike box (i) that covers the relatively flat southern part of Arizona, box (ii) is over the mountainous region in central Arizona with more intense rainfall. All three panels show that whenever there is a major rainfall event it is usually picked up by both 12 km and 3 km runs. However, the rainfall from the 12 km run is systematically less intense than its counterpart from the 3 km run for the same event.

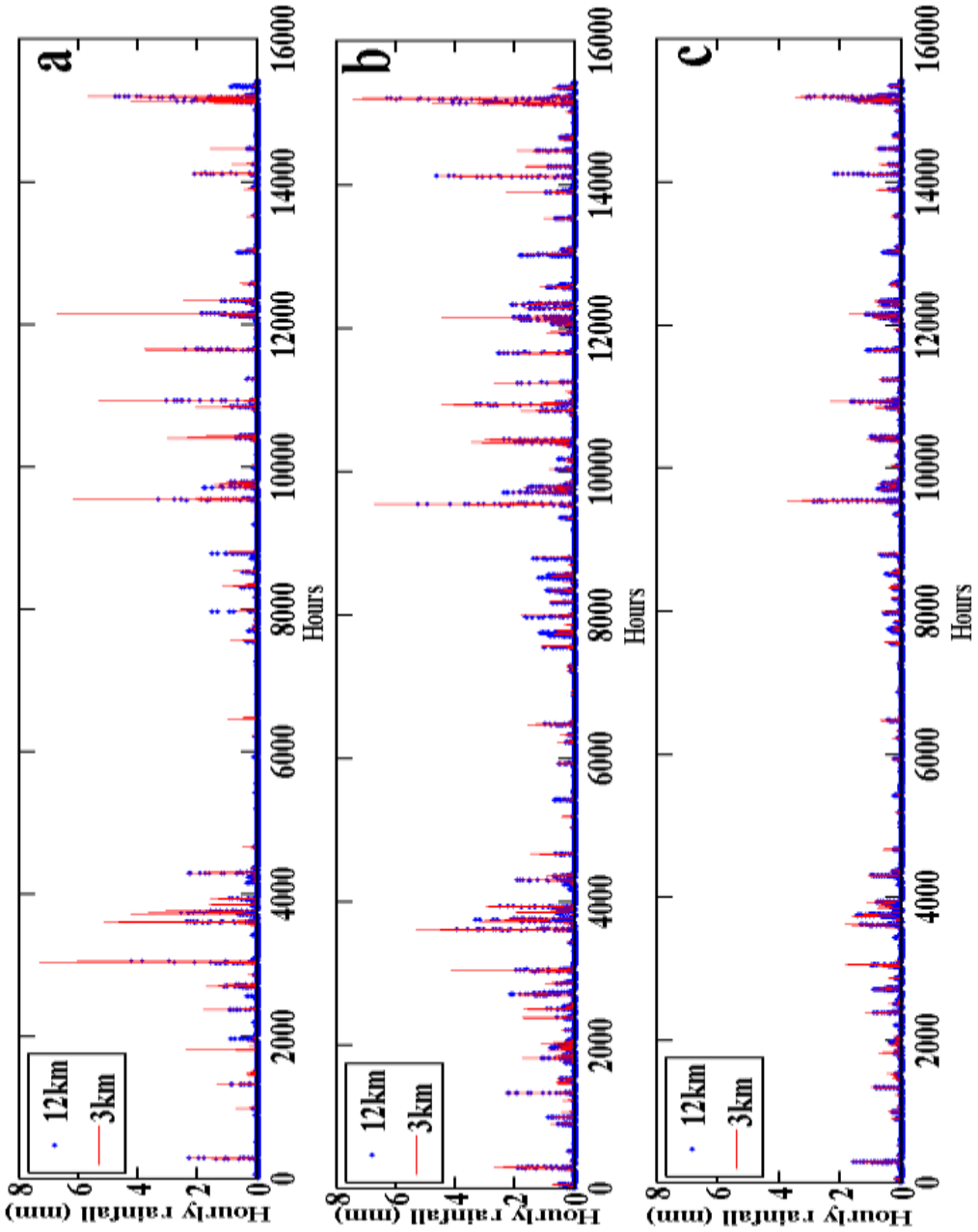

Figure 17: Time series of hourly rainfall averaged over (a) box (i), (b) box (ii) in Figure 9, and (c) the entire innermost domain (Arizona). The red line and blue dots are for the 3 km and 12 km runs, respectively. Each panel contains the time series for all 7 winters stitched together. Abscissa is time in hours.

One can further quantify the differences among the 12 km, 6km, and 3 km runs by comparing their histograms of rainfall using the hourly data for all grid points in the innermost model domain over Arizona. For a fair comparison, we first merge 16 (4 x 4) grid boxes of the 3 km runs into a "super box" with dimension of 12 km x 12 km (i.e., the same size as one grid box for the 12 km runs) and calculate the averaged rainfall for each super box. In doing so, we have about the same number of grid boxes (times the number of hours) from the 3 km and 12 km runs to construct the histograms. Similar approach is used to coarse grain 6 km to 12 km resolution. The comparison for all 4 major cases listed in Table 1 is shown in Figure 18 in a log-linear plot, using a bin width of 3 mm of rainfall. All 7 winters of simulations are used. (The left most bar is for the samples with no rain.) It is interesting to note that extreme rainfall events with hourly rainfall exceeding 21 mm over a 12 km x 12 km box are produced only by the 6 km and 3 km runs, while they are absent in the 12 km runs.

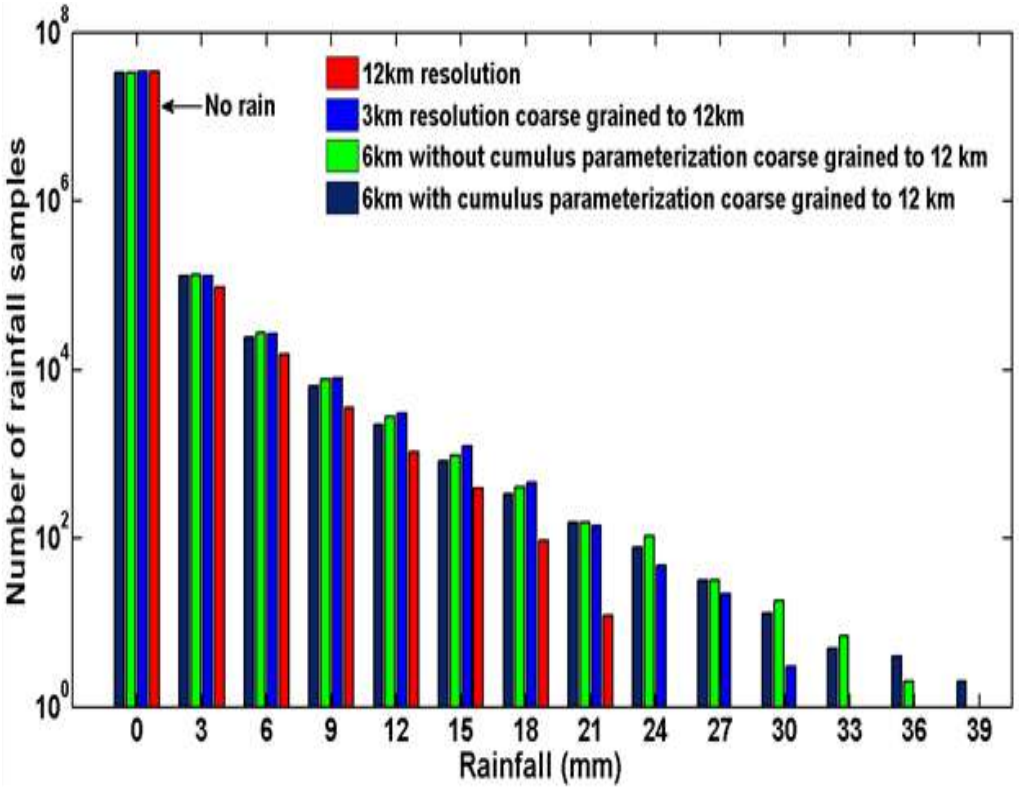

Figure 18: A comparative histogram with a 3 mm bin width for the rainfall from the 12 km, 6 km with and without parameterization, and 3 km runs. For the 6 km and 3 km runs, the data has been coarse grained to 12 km grid to facilitate a fair comparison to the 12 km runs.

3.4.6 Vertical velocity

Since rainfall is closely related to vertical motion (either by convection or mechanical lifting), a further analysis of the variance of vertical velocity is performed to help understand the behavior of rainfall in our simulations. As a useful comparison of the vertical velocity field across the four major sets of simulations, we choose to focus on the standard deviation of vertical velocity at a

mid-tropospheric level where vertical velocity is near its maximum. To help choosing this level, Figure 19 first illustrates the averaged vertical profile of vertical velocity from selected runs (one set each for 12, 6, and 3 km resolution). In order to meaningfully relate the vertical velocity to convection or rainfall, in Figure 19 only the vertical profiles over the grid points with hourly rainfall exceeding 2 mm are included for the averaging. Given the large variation of topography over Arizona, we further classified the grid points into three groups of low (Ps > 945 hPa), medium (800 hPa < Ps < 945 hPa), and high surface elevation (Ps < 800 hPa, where Ps is surface pressure), shown in Figure 19 in red, green, and blue, respectively. Each curve in Figure 19 is based on the statistics of hourly model output for the 7-winter runs. From Figure 19, the vertical profile of vertical velocity associated with rainfall generally has a uni-modal structure with maximum at close to 625 hPa, a level we choose for a further analysis.

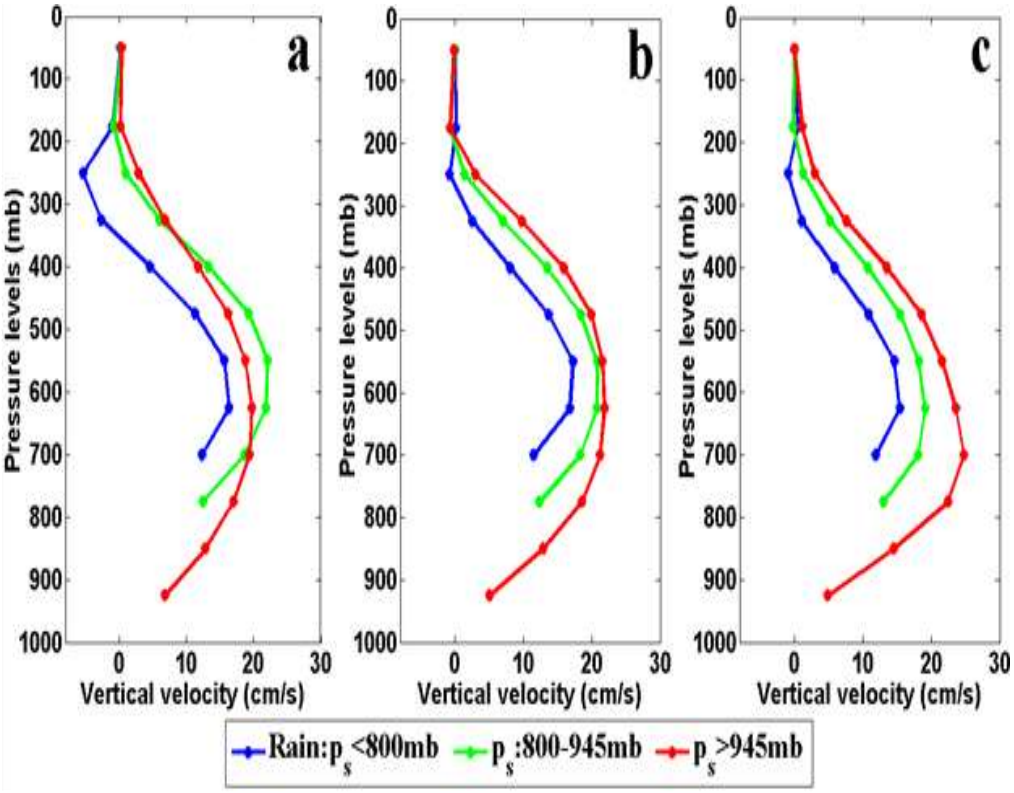

Figure 19: The averaged vertical profiles of vertical velocity (in cm/s) deduced from (a) 12 km runs (b) 6 km runs with cumulus parameterization turned on, and (c) 3 km runs.

As shown in Figure 19, a standard deviation of vertical velocity at 625 mb pressure level is constructed for different domains. It compares the dependence of variance of vertical velocity at different resolutions. The results show that the increase in rainfall with increase in grid resolution could be due to two possible mechanisms. Assuming low elevation regions like Phoenix can have more rainfall if it has more moisture content. If boundary layer becomes wetter, i.e. it has more moisture, then the convergence of velocity and moisture given by, $-\int \nabla.(\nu q)dz$, will lead to rainfall to maintain the water budget. Even if there is no change in velocity field for horizontal convergence, we can have more moisture that will cause more rainfall. This process can be due to increase in temperature and in turn increase in water vapor.

Alternatively, when there is no change in moisture, there could be change in convergence of velocity. If there is a mountain, it can cause horizontal convergence of velocity. Since the wind can't penetrate the mountain, it goes upward i.e. mountain will convert horizontal velocity to vertical velocity. So, mountain will always create a mass convergence. As seen in Figure 14, 3 km grid spacing has highly resolved terrain. It increases our chance for increase in topographic lifting. Comparing 6 km and 3 km runs, it can be observed that mountains will become sharper for finer resolution and effect of topographic lifting is even more intense. Normally, in atmosphere with no mountains (for atmosphere not too far from hydrostatic), velocity is calculated from mass continuity equation. For such a situation, with atmosphere close to hydrostatic state, the vertical velocity is calculated from vertical integration of mass. If there

is a lot of mass convergence in the region, it results in water vapor and in turn rainfall. Thus, for a situation with no mountains, but large scale motion, we can have vertical convergence & that can produce rainfall.

Therefore, increase in rainfall in Arizona is due to two processes. Firstly, it could be due to thermodynamical process. This mechanism will increase moisture (q) without any change in divergence of vertical velocity. It will cause more rainfall just by ample supply of moisture. Secondly, rainfall is possible through mechanistic process, wherein, there is no change in moisture (q) but change in wind velocity. (The reason our simulations are showing more rainfall in finer resolution is due to the wind velocity term, as the amount of moisture remains unchanged, we are not playing with q). So, the mechanistic process is dominant in Arizona's hydrology.

Figure 20 shows the standard deviation of vertical velocity at 625 hPa level for the innermost domain, for the 4 major sets of runs with 12, 6, and 3 km resolution. At 12 km resolution, the maximum vertical velocity is mostly associated with large-scale topographic lifting over northern Arizona where the highest peaks of mountains in Arizona are located. Over there, most of the precipitation in winter is snow such that the maximum vertical velocity does not correspond to maximum liquid-form rainfall, which is located in central Arizona. For the two cases with 6 km and especially the case with 3 km resolution, we begin to see more fine structures of vertical velocity over the mountainous central Arizona, and a hint of northeast-southwest oriented "streaks" in southern Arizona. Those streaks are consistent with a similar structure in rainfall (see Figure 10d).

They likely reflect the impact of fine topography on rainfall in this region. They become even more prominent in the 3 km run. The contrast between 3 km and 12 km runs in Figure 20 is significant; The aforementioned streaks in the 3 km runs are almost absent in the 12 km runs. The change in the characteristics of vertical velocity with resolution shown here is consistent with the changes in the intensity and patterns of rainfall in Figure 9. The maps in Figure 20 are based on the vertical velocity at original model grids, i.e., the standard deviation in Figure 20a is on 12 km grid, and that in Figure 20d is on 3 km grid, and so on. However, even after coarse-graining the vertical velocity fields of the 6 km and 3 km runs to the 12 km grid, the qualitative differences among the 4 runs described above remain true (not shown). Figure 21 shows cumulative snowfall for year 2008 and 2009 at 12, 6 and 3 km resolutions. No further analysis is done on snowfall analysis.

Conclusions of this chapter are included at the end of chapter 4, in section 4.4.

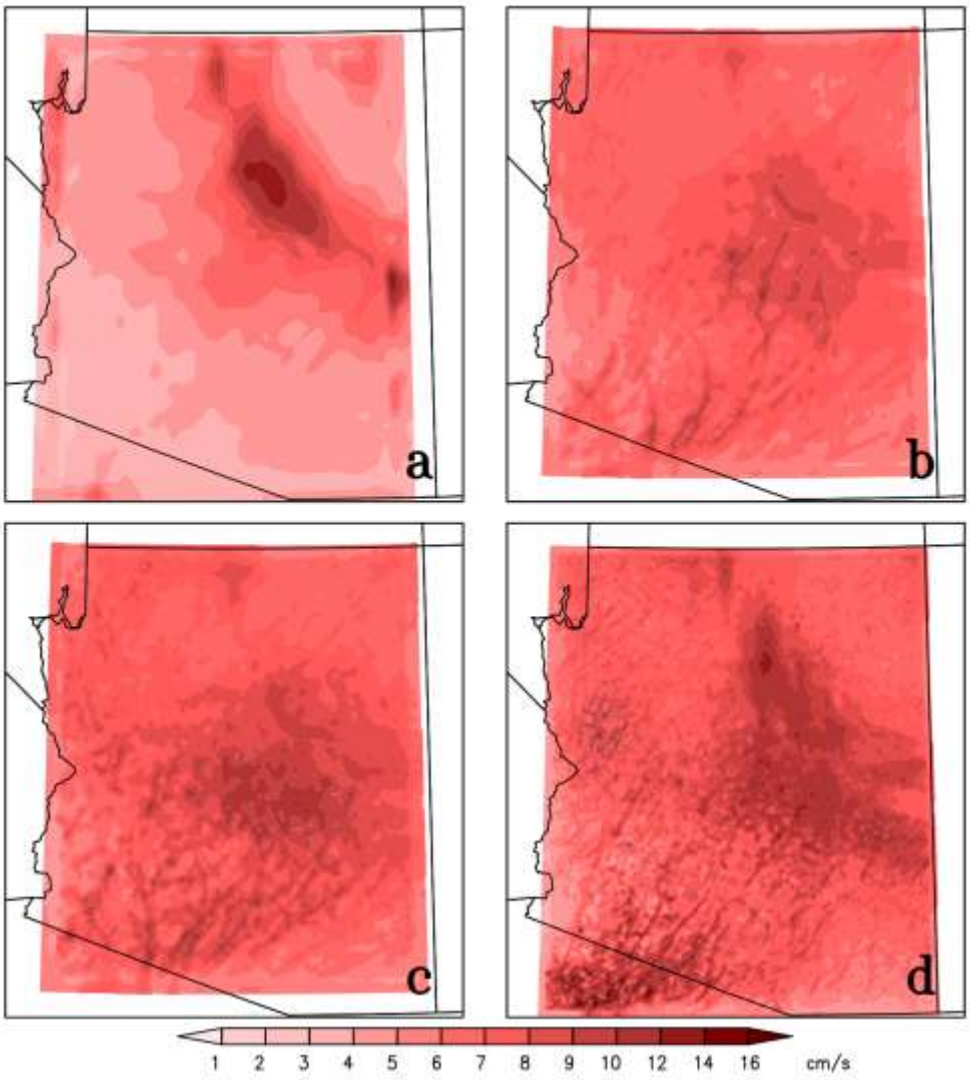

Figure 20: The standard eviation of vertical velocity at 625 hPa level for (a) the 12 km runs, (b) the 6 km runs with cumulus parameterization turned on, (c) the 6 km runs with cumulus parameterization turned off, and (d) the 3 km runs. The color scale in cm/s is shown at bottom.

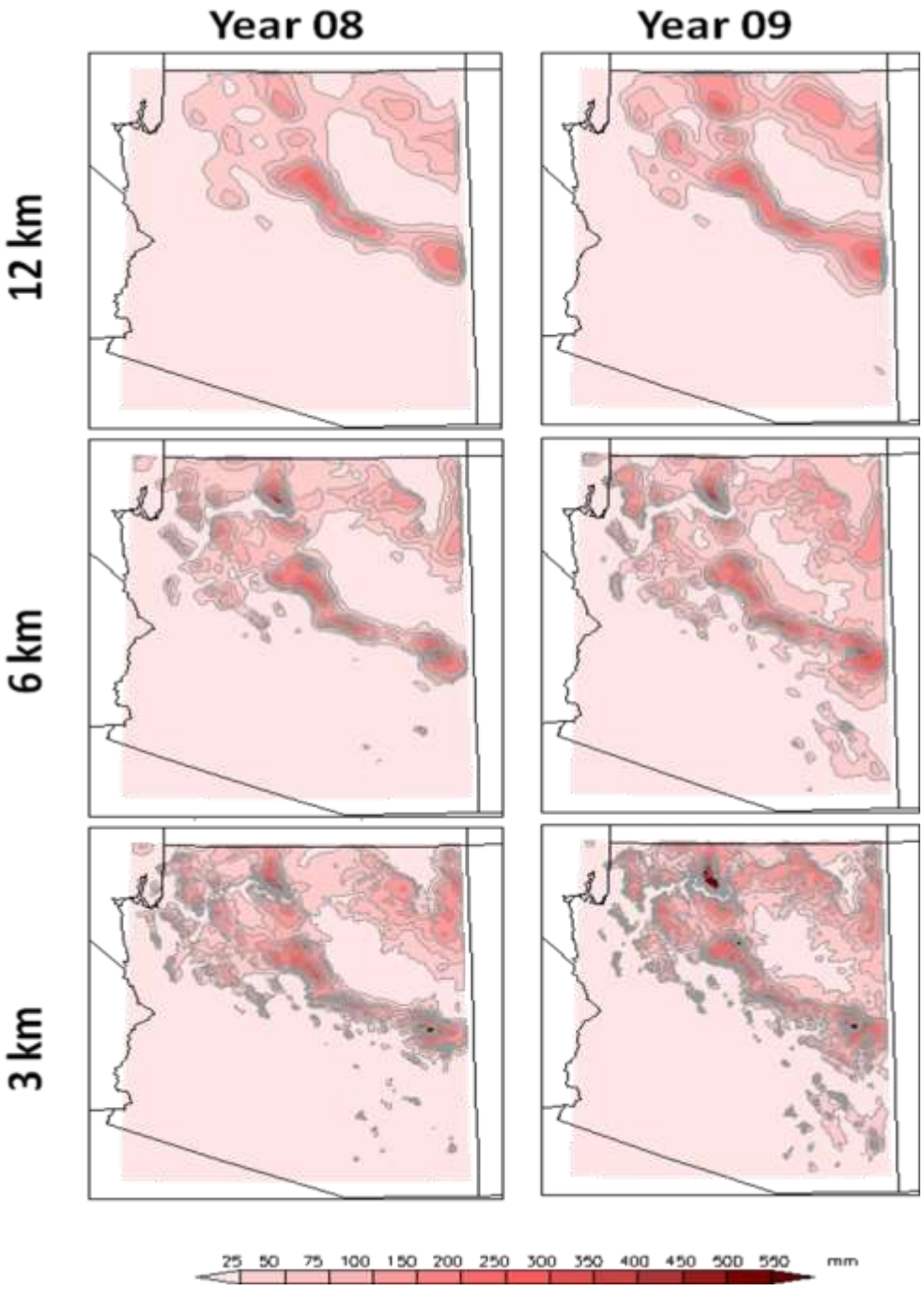

Figure 21: Cumulative snowfall for year 2008 and 2009 at different grid resolutions.

Chapter 4

4. ARIZONA STUDY: PART 2

Given our finding in Chapter 3, it will certainly be useful if the high-frequency behavior of the simulated rainfall can be further validated with observation. The existing rainfall PRISM observations for Arizona do not have a spatial and temporal resolution comparable to our model simulations. (The PRISM data used for the model validation in Sec 3.2 are only monthly mean.) This will be a very useful comparison if such high-resolution observations become available in the future. Chapter 3 focused on state-wide features. In this chapter, we use station observations to compare simulated rainfall on local scales.

4.1 Comparison of simulated rainfall with station observations

Rain gauges network in a region are sparse and thus available data is insufficient to characterize spatial distribution of rainfall [*Smith*, 1996]. Thus, Numerical Weather Prediction (NWP) models are used to estimate rainfall estimates at high temporal and spatial resolution to study climate variability.

In this study, seven stations at different topographical locations are selected to test the sensitivity of output at different resolutions for rainfall and temperature with observations. Hourly rainfall inputs are analyzed for only six stations for seven winter seasons from 2003-09 (one of the station does not have measurements for year 2009 winter). The output of the hourly rainfall at each

resolution is statistically compared with the Arizona Meteorological Network (AZMET) dataset for rainfall. Figure 22 shows a typical station used in Arizona by AZMET and the geographic locations of all seven stations. Rainfall measurements are done with Sierra Misco RG2501 Rain Gauge or Texas Instrument rain gauge. They have a tipping bucket magnetic sensor with an accuracy of +/-1 mm. Air temperature is measured by Vaisala HMP35C/45C instrument that has thermistor sensor. The accuracy of air temperature sensors is +/-0.4 ^{0}C. Stations collect hourly measurements each day. More detailed information on the AZMET observational network is available on the World Wide Web at http://ag.arizona.edu/azmet/. Table 2 shows the lat-lon location and elevation of the observation sites in Arizona used in this study.

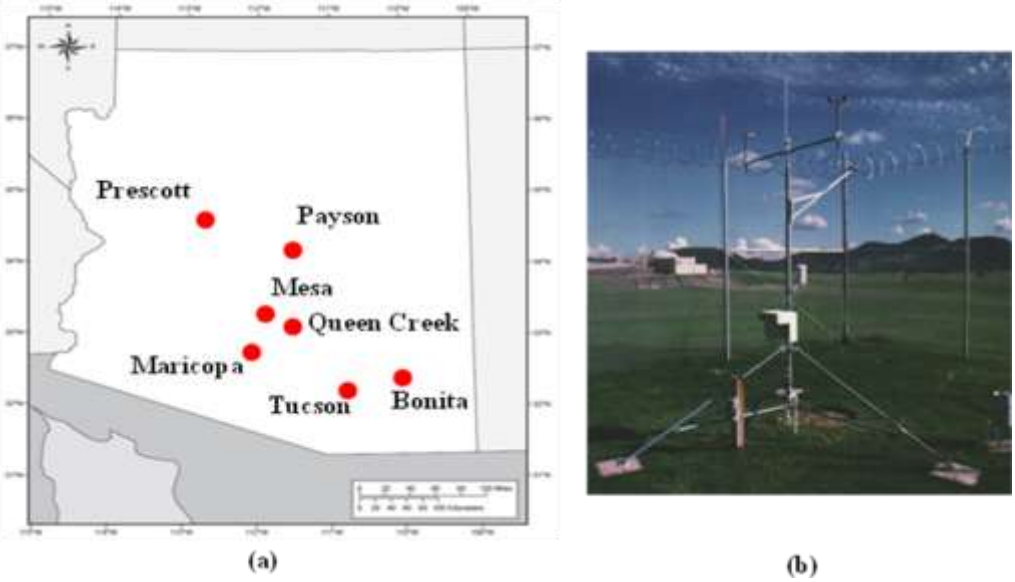

Figure 22: (a) Location of stations in Arizona used in the study. (b) A typical photo of a measurement station used in Arizona by AZMET. The station measures rainfall using a rain gauge, wind speed, direction and air temperature.

Table 2: Location and elevation of the observation sites in Arizona (AZMET) used in this study.

Station name	Location	Elevation (m)
Bonita	32° 27' 49" N, 109° 55' 46" W	1346
Maricopa	33° 04' 07" N, 111° 58' 18" W	361
Mesa	33° 23' 12" N, 111° 52' 03" W	366
Payson	34° 13' 57" N, 111° 20' 39" W	1478
Prescott	34° 35' 31" N, 112° 25' 11" W	1583
Queen Creek	33° 11' 20" N, 111° 31' 48" W	457
Tucson	32° 16' 49" N, 110° 56' 45" W	713

We first analyze the simulated weekly rainfall from the WRF model outputs. We choose six stations at different topographies to validate the model results at different terrains. The grid points that are closest to the station's lat-lon are selected to create a time series of hourly simulated rainfall for a winter season. These time series are then stitched together and compared to their respective station measurements. Since, the time series at hourly interval produce a lot of fluctuations, we collect rainfall for a week and construct weekly rainfall for each station as shown in Figure 23. For most cases, it is observed that WRF simulations pick the rainfall events whenever there is rainfall in observations. However, the magnitude of rainfall varies with resolutions. 12 km resolution shows the closest match with observations. 6 and 3 km resolution shows relatively higher amount of rainfall. The model is sensitive during the dry periods of 2004 winter. Observations show no signs of rainfall during this period. However, the WRF model at 6 and 3 km resolution pick some amounts of rainfall. The noticeable feature of the simulations is that there is no time lag for rainfall between simulations and observations and both have a similar temporal evolution.

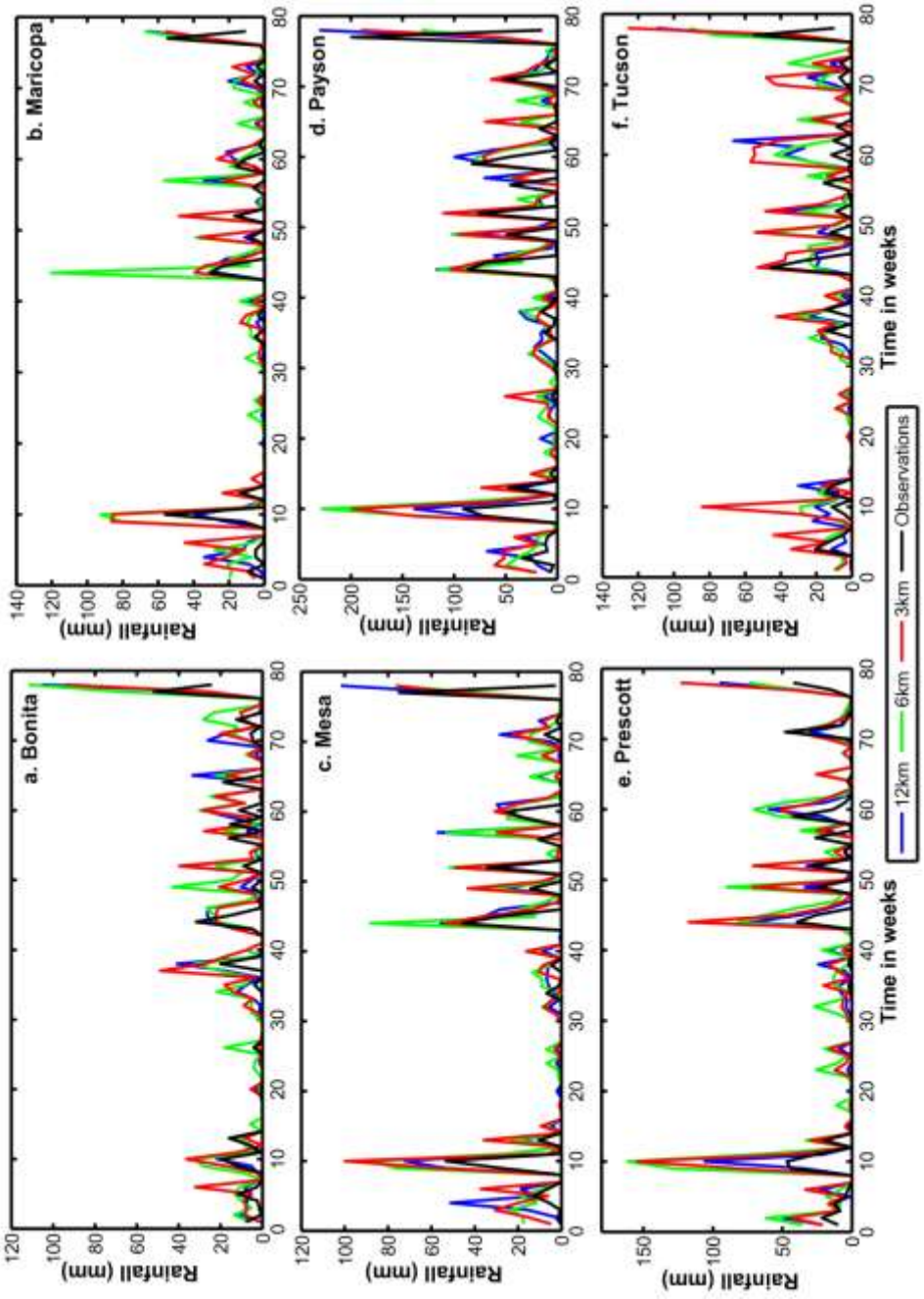

Figure 23: Comparative time series of simulated and observed weekly rainfall for 7 years for six different stations at 12, 6 and3 km resolutions with station observations.

Figure 24 is a six panel figure for each year from 2004-09 showing the total amount of rainfall for each station at 12, 6, 3 km resolutions and observations. It can be seen in Figure 24 that for any given year, rainfall varies with a station's topographic location. Normally, a station at low elevation and at plains (Maricopa/Mesa) has a less amount of rainfall than a station at high elevation (Payson). Note that the ordinate in the panels of Figure 24 are not same for all subplots. Comparing all the subplots for each station, it is observed that the model reproduces the inter-annual variability for each station. Since, each station is located at different terrain; they have their own local systematic bias at different resolutions that varies from season to season. The removal of local bias can ascertain better predictions for each station. Figure 25 shows the bias at each station. The bias is calculated at each station by subtracting 12 km resolution rainfall with observations for simulations from 2004-09 (since simulations from 12 km resolution produces the closest results to observations). This calculated bias is then subtracted from each corresponding 6 and 3 km resolution rainfall amounts for every station and is shown in Figure 25. Figure 26 shows the total weekly rainfall for all stations under consideration for six years from 2004-09. From the plot it is inferred that 12 km resolution rainfall has a wet bias but is close to observation in comparison to 6 and 3 km resolution rainfall.

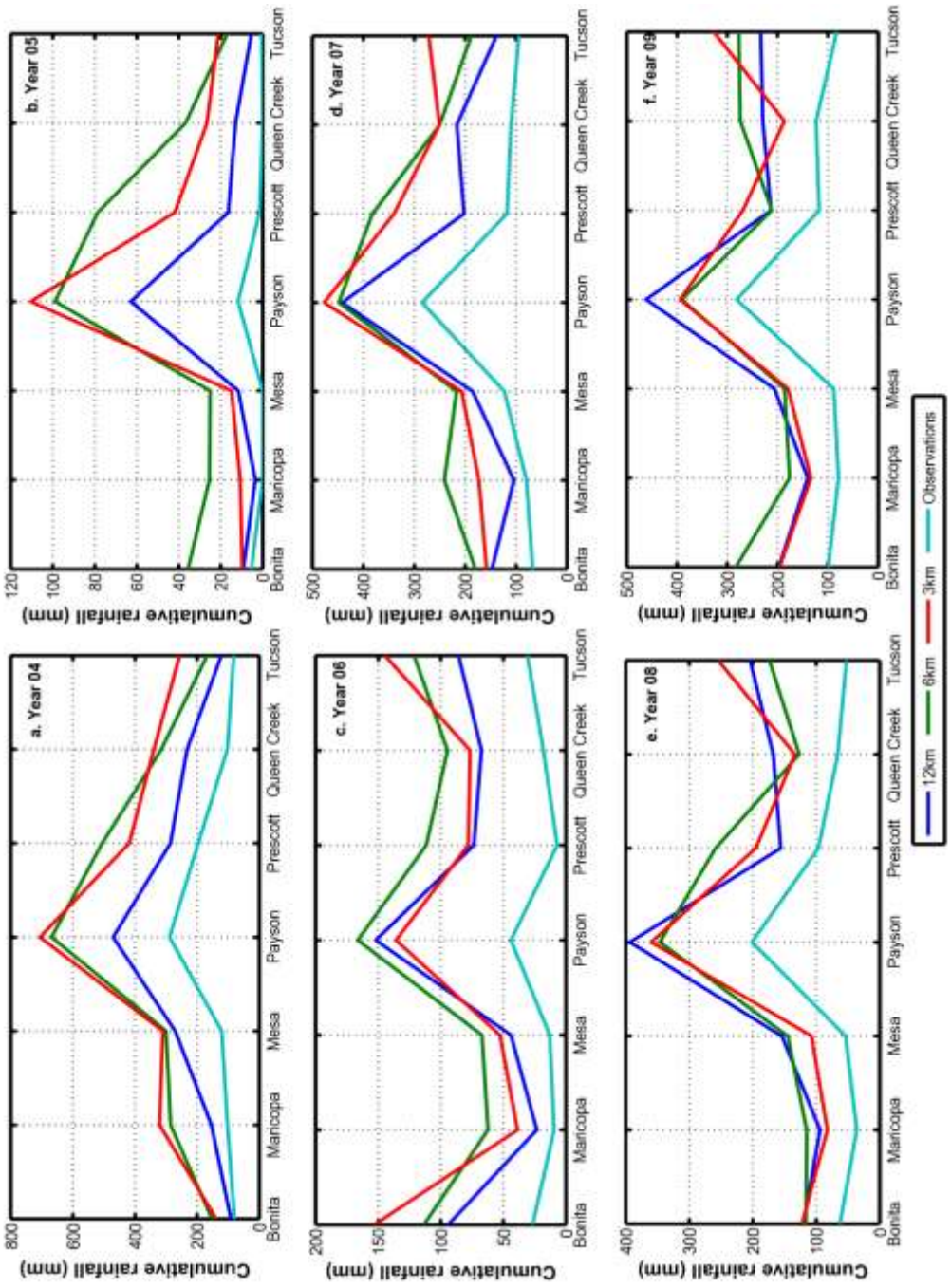

Figure 24: Comparisons of the simulated winter seasonal rainfall with observation for six years (2004-09) for different stations at different resolutions. The observation from AZMET data is in light green.

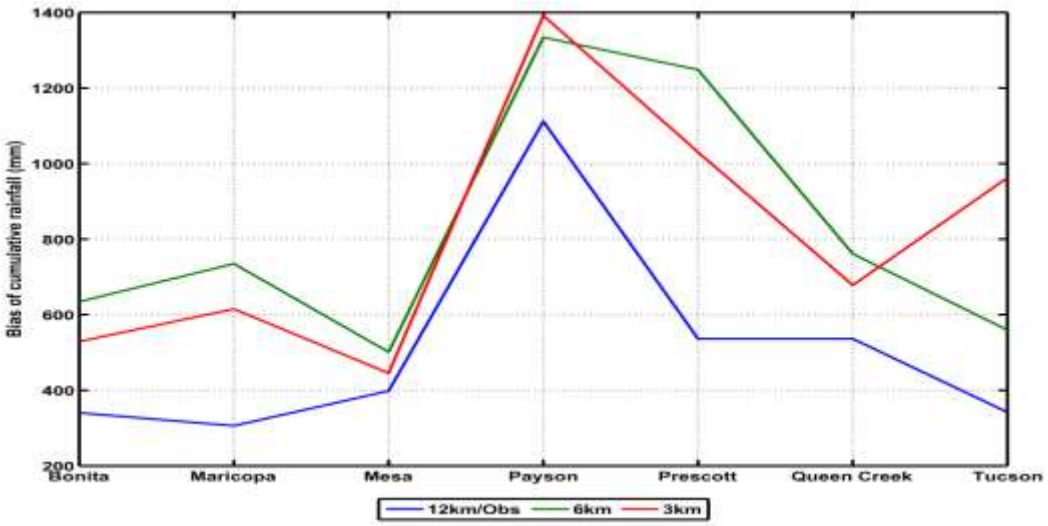

Figure 25: Bias of the simulated total winter seasonal rainfall with observation for six years (2004-09) for different stations at different resolutions. We assume that the bias is the difference between 12 km and observations. The plot shows bias corrected amounts for 6 and 3 km simulations.

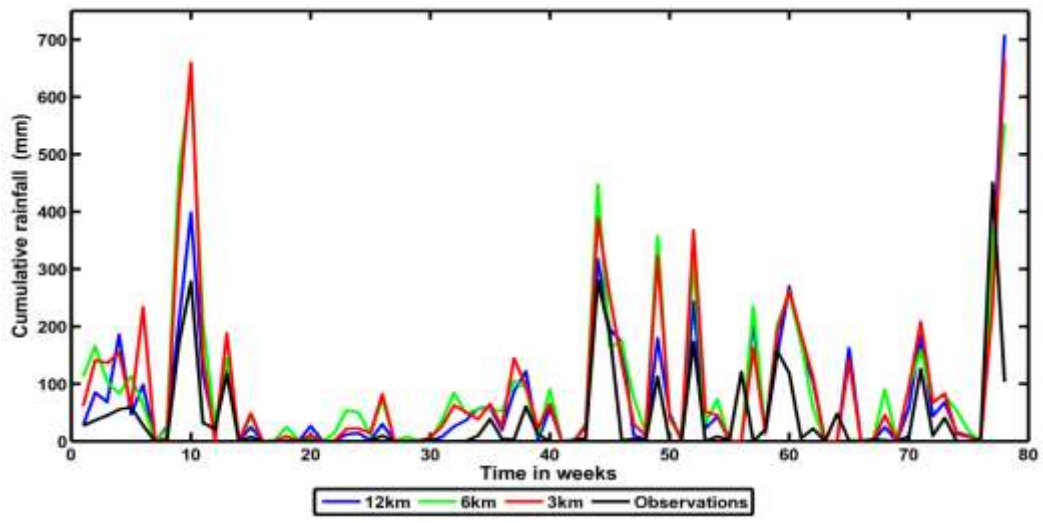

Figure 26: Comparison of total weekly rainfall for all stations under consideration for six years from 2004-09 at 12, 6 and 3 km resolutions with observations.

4.2 Statistical evaluation of station rainfall

Statistical analysis is performed on weekly winter rainfall to assess the simulation performances relative to the station observations. We perform both categorical and continuous statistics: For categorical statistics, we use a 2x2 contingency table for detection tests and for continuous statistics; we use root mean square errors for retrieval tests. Scores are commonly used to statistically assess the performance of a model simulation relative to observations (validation) or to compare with the results of other model simulations (inter-comparison). Some of them are derived from a 2×2 matrix called "contingency table" [e.g., *Wilks*, 1995], where each of the elements (*H*, *F*, *M*, *R*) holds the number of combinations of model prediction and observation in a given statistical population (see Table 3). The contingency table is a useful way to see different types of errors in simulations. A perfect forecast system would produce only hits and correct number of non-events, and no misses or false alarms. In this study, five different statistical scores are studied and are shown in Table 4.

Table 3: Contingency table for winter rainfall sensitivity study for Arizona.

		Observed rainfall (Rain gauge)	
	Event	Rain	No rain
WRF estimated rainfall	Rain	Hits (H)	False alarm (F)
	No rain	Miss (M)	Correct non–event (R)

Bias Score (BIAS): This score is an indicator of how well the model recovers the number of occurrences of an event, regardless of the spatio-temporal distribution. (Range: 0 to ∞. Perfect score: 1).

$$BIAS = \frac{F + H}{M + H} \tag{21}$$

False Alarm Rate (FAR): It computes the fraction of predicted events that were not observed. (Range: 0 to 1. Perfect score: 0.)

$$FAR = \frac{F}{F + H} \tag{22}$$

Probability of Detection (POD): Fraction of the observed precipitation events that are also correct forecast. (Range: 0 to 1. Perfect score: 1.)

$$POD = \frac{H}{H + M} \tag{23}$$

Probability of False Detection (POFD): It is the fraction of the predicted rainfall events that have not been observed relative to the total number of unobserved events. (Perfect forecast, POFD = 0.)

$$POFD = \frac{F}{F+R} \tag{24}$$

Heidke Skill Score (HSS): It indicates the capability of a simulation to be better or worse than a random simulation, and ranges from −1 to 1 (1 for a perfect and 0 for a random case).

$$HSS = \frac{S - S_{\mathrm{Re}f}}{S_{Perf} + S_{\mathrm{Re}f}} \tag{25}$$

where $S = \frac{H+R}{N}$; $S_{\mathrm{Pr}ef} = 1$; and $S_{\mathrm{Re}f} = \frac{(H+F)(H+M)+(F+R)(M+R)}{N^2}$

For calculating the above statistical variables, simulation and observation time series were considered above 5 mm threshold amounts. The statistical results are put together in Table 4. It is observed that for all stations Bias Score is lowest for 12 km resolution confirming that the model has recovered the number of occurrences of rainfall events regardless of temporal distribution. However, it is observed that WRF model has a tendency to over-forecast (*BIAS* > 1) winter events in Arizona. *POD* determines the hit rate. Almost 75% and above events were correctly forecasted at all resolutions. Since *FAR* is around 0.5 for all cases, it indicates that for around 50% of the forecasted rain events, rain was not observed. The value is relatively high as it is sensitive to false alarms, but ignores misses.

Table 4: Scores for statistical evaluation for weekly six years winter rainfall for year 2004-09 for station sites at different resolutions.

Bias score (BIAS)

	Bonita	**Maricopa**	**Mesa**	**Payson**	**Prescott**	**Tucson**
12 km	1.78	1.33	1.94	1.85	1.55	1.55
6 km	2.33	2.20	2.31	2.08	2.20	2.10
3 km	2.17	1.80	2.00	1.88	1.85	2.00

False Alarm Rate (FAR)

	Bonita	**Maricopa**	**Mesa**	**Payson**	**Prescott**	**Tucson**
12 km	0.56	0.40	0.55	0.54	0.42	0.45
6 km	0.64	0.58	0.62	0.57	0.57	0.57
3 km	0.64	0.52	0.56	0.53	0.49	0.58

Probability of False Detection (POFD)

	Bonita	**Maricopa**	**Mesa**	**Payson**	**Prescott**	**Tucson**
12 km	0.30	0.13	0.27	0.50	0.22	0.24
6 km	0.45	0.31	0.37	0.60	0.43	0.41
3 km	0.42	0.23	0.29	0.50	0.31	0.40

Probability of Detection (POD)

	Bonita	**Maricopa**	**Mesa**	**Payson**	**Prescott**	**Tucson**
12 km	0.78	0.80	0.88	0.85	0.90	0.85
6 km	0.83	0.93	0.88	0.88	0.95	0.90
3 km	0.78	0.87	0.88	0.88	0.95	0.85

Heidke Skill Score (HSS)

	Bonita	**Maricopa**	**Mesa**	**Payson**	**Prescott**	**Tucson**
12 km	0.38	0.57	0.45	0.29	0.57	0.51
6 km	0.17	0.51	0.39	-0.42	0.24	0.27
3 km	0.26	0.65	0.57	0.00	0.54	0.31

For continuous statistics, results from rainfall simulations show that the 12 km resolution shows a lower value of root mean squared errors in comparison to other resolutions. These results show that coarse resolution is optimal for downscaling rainfall for our configuration of the model. Table 5 shows RMSE errors for the weekly time series of winter rainfall from year 2004-09.

Table 5: RMSE errors for weekly six years winter rainfall for year 2004-09 for station sites at different resolutions (mm).

	Bonita	**Maricopa**	**Mesa**	**Payson**	**Prescott**	**Tucson**
12 km	13.48	10.05	16.40	35.72	14.26	16.57
6 km	14.71	18.31	16.29	34.04	25.06	16.00
3 km	14.04	14.55	14.40	36.57	22.40	23.78

4.3 Comparision of simulated temperature with station observations

Figure 27 shows the comparison of simulated daily temperature with observations. To calculate simulated daily temperature, average temperature for each day is calculated from hourly outputs. Although we only show the results for year 2009 winter season, the simulations for the other winter seasons are qualitatively similar to this case. Temperature is a prognostic variable and not a by-product of downscaling. It does not fluctuate much with space, except when there is a steep gradient in topography. Thus, with refinement in resolution simulated temperature shows better correlation with observations. For all resolutions, simulated temperature has 0.96 correlation coefficient with 98% significance level. Note, the timestamps in WRF model and its output are on Coordinated Universal Time (UTC). In this exercise, since the observations are in Mountain Standard Time (MST), WRF model outputs in UTC clock is adjusted to MST for a fair comparison.

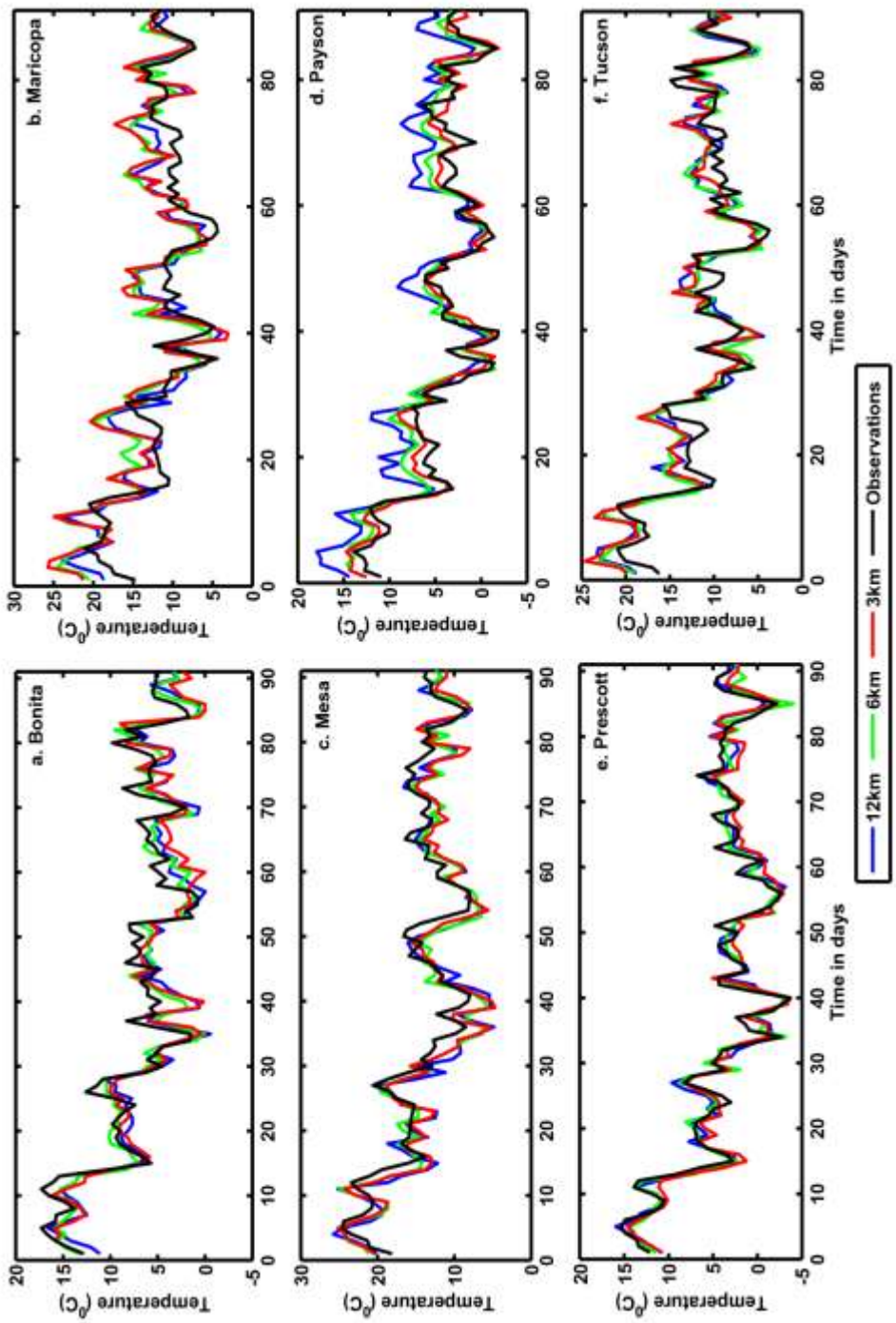

Figure 27: Comparison of daily winter temperature for year 2009 for different stations at different resolutions with observations.

4.4 Conclusions for Arizona study

Important findings from different kinds of sensitivity tests performed over Arizona in chapter 3 and 4 are given below:

1. Sensitivity tests on spatial distribution for Arizona show that rainfall at 12 km resolution is closest to observation. The rainfall produced by grid scale processes in 12 km run is the dominant contributor to the total rainfall, in contrast to coarse resolution global climate models that rely almost exclusively on subgrid convective scheme to generate precipitation.
2. Sensitivity of convective parameterization shows that when sub grid-scale convective parameterization is turned off at 6 km, grid-scale convective rainfall increases to compensate for the absence of subgrid-scale rainfall. They both have a similar pattern in their temporal evolution.
3. It is found that the simulated winter seasonal mean rainfall for different sub-domains of Arizona increases substantially with the refinement of horizontal resolution from 12 to 6 km. The increase is minimal from 6 to 3 km. Simulations show that whenever there is a major rainfall event, it is usually picked up by both 12 km and 3 km runs and the 12 km run is systematically less intense than its counterpart from the 3 km run for the same event.
4. An interesting result from the sensitivity test shows that higher resolution runs with $\Delta x \leq 6\,\text{km}$ produce extreme rainfall events that are absent in lower resolution runs.
5. Simulations from 3 km run show a substantial increase in the maximum rainfall over the mountains in central Arizona and emergence of organized

convective storms moving across the relatively flat southern Arizona. The changes in the characteristics of vertical velocity with resolution are consistent with the changes in the intensity and patterns of rainfall.

6. Results from studying the effect of changes in time step size generally confirm that (for the range of time step size we use) the dependence of the simulated seasonal rainfall on *dt* is weak.
7. Isolating the effects of refining grid resolution vs. refining topography show that the effect of changing the resolution of topography is not negligible (using the 2' topography leads to more "streaks" in the rainfall pattern whose realism remains to be analyzed as future work).
8. Comparison of simulations with the observed seasonal mean rainfall from the PRISM data and rain gauge stations show that the rainfall simulated by the 3, 6 and 12 km runs is excessive, while that produced by the 12-km-grid simulations is closer to observations.
9. Cumulative rainfall is examined at 54, 36, 18, 12, 6 and 3 km grid resolution. However, rainfall at 12 km performs better in comparison to high resolutions and coarse resolution runs. Comparison of simulations at these different resolutions with PRISM observations shows that WRF successfully simulate interannual variability of rainfall for the state of Arizona in winters (even without interior nudging) at 12 km resolution and higher.
10. Comparison with station observations show that temperature has 0.96 correlation coefficient and above with 98% significant level for 12, 6 and 3 km resolutions, but with higher accuracy at 3 km resolution.

11. Simulations show that rainfall at 12 km resolution is closest to observation in comparison to higher resolution runs from 6 and 3 km. It is counter intuitive as the results should numerically improve (converge to observations) at higher resolution. Thus, further research should be directed towards studying the physical processes at these higher resolutions that currently are giving erroneous results at 6 and 3 km resolutions. (We leave this analysis for future study).

Chapter 5

5. ARAL SEA STUDY

5.1 Introduction

This chapter serves the purpose of testing the sensitivity of WRF model simulations on changes in the surface characteristics. For this purpose, Aral Sea, a natural test-bed is chosen. This section of the study relates observed climate with land cover change caused by drying up of the Aral Sea. To explore this interaction caused by the desiccation at local scale and overall warming trends in Central Asia at regional scale, a series of climate downscaling experiments for 1960 and 2000 decade are performed using the WRF model at 12 km model resolution. These decades are selected to perform sensitivity tests because the desiccation began in 1960s and reached its limits in 2000s. Both winter and summer seasons are studied. Sensitivity tests include a set of runs performed by changing Aral Sea spread with same lateral boundary conditions to quantify the relative contribution of change in land/sea surface and, in another set of runs keeping a constant Aral Sea spread and changing lateral Boundary Conditions (BC) to quantify the effect of large scale BC over the Aral region.

5.2. Background

The Aral Sea belongs to two states of former Soviet Union, Uzbekistan and Kazakistan in Central Asia. Since 1960s, it has lost over 80% of its surface

water and about 90% of its water depth. The shrinking of Aral Sea is considered anthropogenic in nature. The shallowing of the Sea was caused primarily by unsustainable diversions of the inflowing Amu Dar'ya and Syr Dar'ya rivers to provide water for rice irrigation and cotton plantation (Figure 28). It caused the Sea to sink by more than 50%, to lose two-thirds of its volume, and to greatly increase its salinity. The contribution of anthropogenic factors in desiccation of Aral Sea is undeniable. However, a section of scientific community believes that a part of desiccation may have been due to large-scale natural climatic warming trends across Central Asia [*Small et al.*, 2001]. So, there is a debate about the role/share of climate verses anthropogenic factors on desiccation of Aral Sea. Desiccation of Aral Sea and its disaster has adversely affected local climate, water balance and marine environment in the region [*Bortnik and Chistyaeva*, 1990; *Perera*, 1993; *Muminov and Inagatova*, 1995; *Pidwirny*, 1999; *Chub*, 2000; *Small et al.*, 2001; *Micklin*, 2002; *Khan et al.*, 2004].

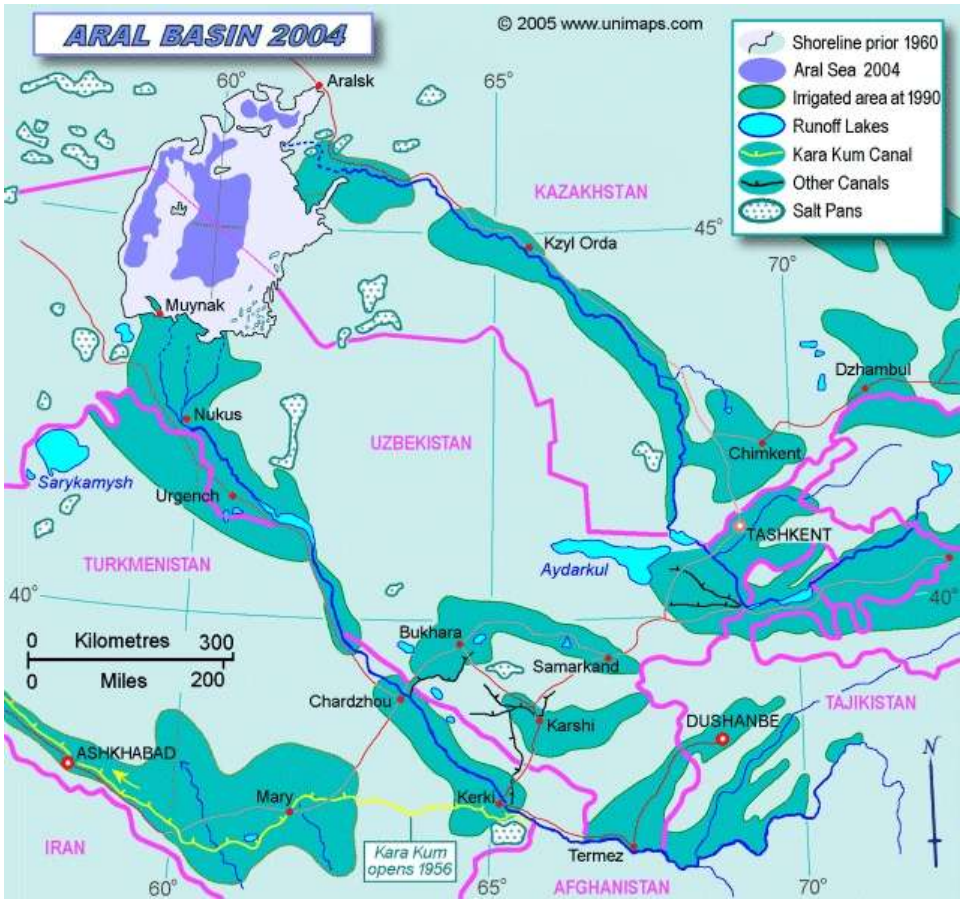

Figure 28: Aral Sea basin in year 2004 showing Aral shorelines, irrigated areas and salt pans in the region (image is taken from www.unimaps.com).

5.3. Objectives and methodology

We plan to perform comprehensive sensitivity analysis to study the impact of change in land cover on the climate over Aral region. Therefore the general objectives of this part of the study are: (i) To explore the sensitivity of changed land cover due to desiccation on critical parameters of the regional climate such

as precipitation (rain and snow), and temperature over the Aral Sea and around the region. (ii) To study how the overall warming in Central Asia affects the regional climate variability (iii) Comparison of simulations with observed station datasets.

To attain the above objectives, we utilize the *climate downscaling* approach that uses large-scale boundary conditions to constrain a mesoscale model for long-term, regional climate prediction [*Giorgi et al*., 2001; *Leung et al*., 2003; *Lo et al.*, 2008]. These regional climate simulations will be performed using the state of the art WRF model [*Skamarock et al.*, 2008]. A lot of climate downscaling studies for seasonal and longer time scales have adopted a horizontal resolution within the range of 12-50 km [*Rockel et al.*, 2008; *Caldwell et al.*, 2009; *Bukovsky and Karoly*, 2009; *Urrutia and Vuille*, 2009; *Raucher et al.*, 2010; *Duliere et al.*, 2011]. The outcome of our study from Chapter 3 and 4 has shown that the simulations with a refined resolution can possibly produce greater deviation from observation as the parameterization schemes for rainfall in the model are not resolution-independent [also see *Sharma and Huang*, 2012]. So we choose to perform this study at 12 km model resolution. Climate downscaling using WRF has never been used for this region to analyze the impact of desiccation and to study the sensitivity of WRF model on changed land cover characteristics for this region. Thus, this study is new and unique.

We will change the surface boundary condition by altering the landscape of the Aral Sea region based on the observed changes in bathymetry for the Sea from year 1960 to 2000. The results of the sensitivity tests from these simulations

will help to quantify the impact of desiccation on the local climate in the region and its interaction with large scale-climate. This study will also present an upscale influence of land cover change over the regional climate. Researchers are facing a challenge to identify the contribution of Aral Sea desiccation in heating up the regional climate, as there is heating all around Central Asia. We will study the influence of warming in Central Asia on the climate of the region. With this sensitivity study, we will help in the disaster management of the region and thus, expect to contribute significantly to the ecosystem management of Aral Sea region.

5.4. Model and numerical experiments

5.4.1 WRF model domain

The region has a few local meteor-stations. These would be insufficient to provide the desired spatial coverage. We use 6-hourly reanalysis data on 2.5x2.5 degree resolution to study the climate change over a domain covering Aral Sea and surrounding regions. The data is produced by U.S. National Center for Environmental Prediction, National Center for Atmospheric research (NCEP/NCAR) [*Kalnay e al.*, 1996; *Kistler et al.*, 2001]. The climate assessment is based on (i) analysis of observational data from oceanographic observations that provide mean depth of Aral Sea and surface water levels from 1960 to present and; (ii) use of global NCAR/NCEP reanalysis data on 2.5x2.5 grid resolution. We will use Weather Research and Forecast (WRF) [*Skamarock*, 2008] Model

Version 3.2, a non-hydrostatic mesoscale model that allows multiple nesting. The model domain consists of three-layer nesting with 108, 36 and 12 km for the outermost, intermediate and innermost domain respectively with all domain centers over Aral Sea. The model grids are configured such that the innermost domain covers Uzbekistan, parts of Kazakhstan & Turkmenistan and outermost domain covers the entire central Asia region. Large-scale boundary conditions are imposed at the lateral boundary of the outermost domain only. We save output after every six hours. Hereafter, unless otherwise noted, the "model resolution" in our discussion refers to the grid size of the innermost domain and all results shown in this chapter are from the innermost domain. Details of nesting and physical topography are shown in Figure 29. The model has 28 levels in the vertical with the model top set at 50 mb. Cumulus parameterization is always turned on for all domains and Kain-Frisch scheme is used for simulations [*Kain and Frisch*, 2004].

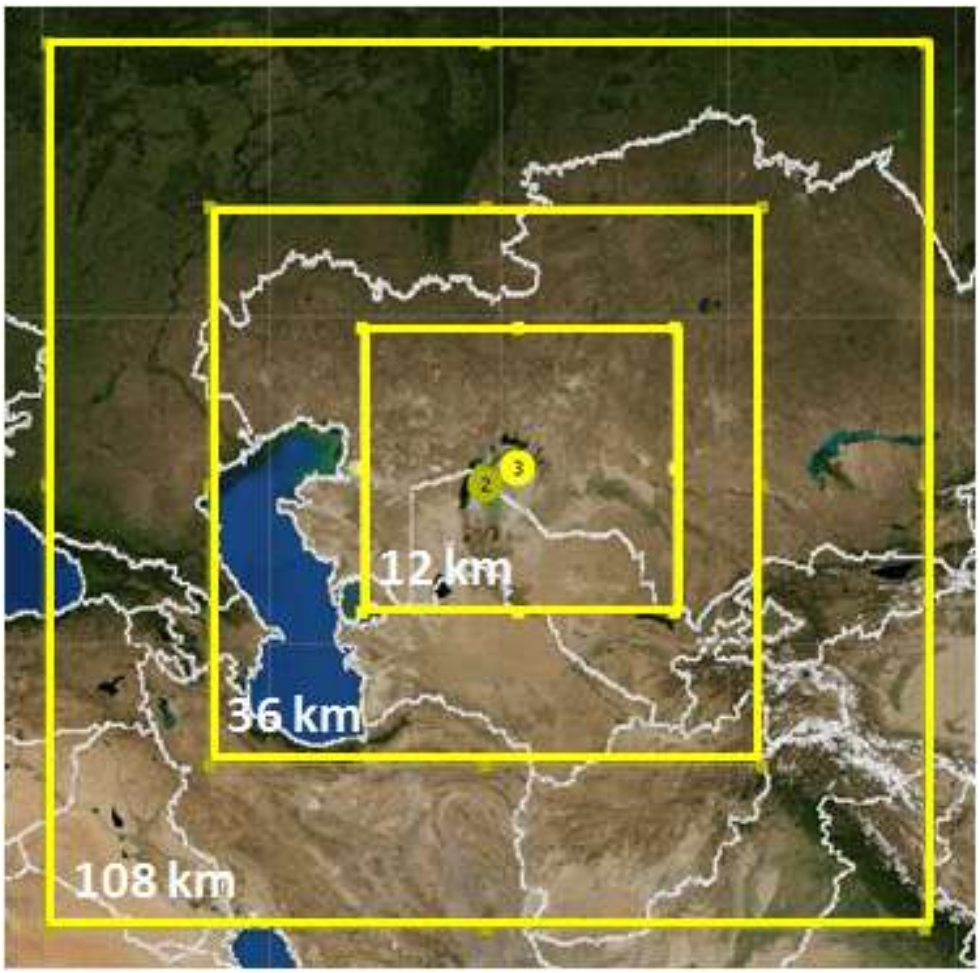

Figure 29: Aral Sea domain and arrangement of nesting for the WRF numerical experiments overlaid on topographical map of Central Asia. Outermost, intermediate and innermost domain has 108, 36 and 12 km grid resolution respectively with all domain centers over Aral Sea.

We use USGS 24 classification categories of land-use data for interpolating topography and land surface characteristics (from standard *geogrid* package in WRF) at 10' spatial resolutions. (The model automatically interpolates

topographic data to the model grids.) Constant surface characteristics are interpolated in all nests and use their respective input files. Only the time varying meteorological and surface data is utilized from the outermost domain. WRF model comes with a constant surface land cover from year 1981. Since the Aral Sea dried up within past half century, the surface landmask and land-use categories have changed. Thus, we perform seasonal simulations for winter and summer with lateral boundary conditions from 1960 and 2000 decade with surface characteristics from year 1960 and 2000 respectively. Another set of simulations has lateral boundary conditions from 2000 decade with surface characteristics from year 1960 to study the isolated effect of large-scale meteorological conditions. Details of the combinations are given in Table 6. Note that we assume that the spread of Aral Sea does not change within a decade.

Table 6: A summary of experimental setup of surface characteristics with lateral boundary conditions performed in this study.

	Case 1	**Case 2**	**Case 3**
Surface characteristics	Year 1960	Year 2000	Year 1960
Lateral boundary conditions	1960 decade	2000 decade	2000 decade

Based on experimental setup in Table 6, we analyze three scenarios. Firstly, change in Aral Sea spread with same lateral boundary conditions from 2000 decade (comparing Cases 2 and 3), would help to quantify the relative contribution of change in land/sea surface. Secondly, constant Aral Sea spread

and change in lateral boundary conditions (comparing case 1 and case 3), would help to quantify the effect of large scale boundary condition over the Aral Sea. Thirdly, comparing different decades with their respective spread in Aral Sea (Case 1 and 2) will give an overall estimate of change in climatology of the region.

5.4.2 Bathymetry of Aral Sea and surface boundary conditions

Bathymetry of the Aral Sea is obtained from the field experiments [*Zavialov*, 2010]. Mean depth and surface water levels from bathymetry helped us to prepare desiccated Aral Sea for the desired years for simulation. Table 7 contains yearly Aral Sea level standings for 1960 and 2000 decade, and the corresponding surface area and volume of the lake. The table also shows the inflow of Amu-Darya and Syr-Darya rivers in the Sea. Value of 999 refers to missing value. It can be seen from table that the yearly lake level standing of Aral Sea has reduced significantly. Figure 30 shows the bathymetry for year 1960 for a reference.

Table 7: A summary of Aral Sea bathymetry and river inflow data for 1960 and 2000 decade. Note that the Aral Sea level is measured from the Ocean Sea Level (OSL). Value of 999 refers to no data available.

Year	Aal Sea level a.o.l. (m)	Mean depth (m)	Surface area (km^2)	Volume (km^3)
1960 decade				
1960	53.4	16.5	61666	1015
1961	53.3	16.5	61666	1015
1962	53	16.5	61666	1015
1963	52.6	16.1	61666	990
1964	52.5	16	61666	984
1965	52.3	16	60924	972
1966	51.9	15.9	59623	948
1967	51.6	15.8	58885	930
1968	51.2	15.6	58110	907
1969	51.3	15.7	58294	912
2000 decade				
2000	33	6	23006	133
2001	999	999	999	999
2002	30.5	6.1	15319	94
2003	30.5	6.1	15319	94
2004	30.7	6.1	15820	96
2005	30.1	6.2	14254	88
2006	29.6	7.8	11347	89
2007	29.2	6.8	12279	84
2008	29.3	6.8	12424	85
2009	27.6	11.8	6015	71

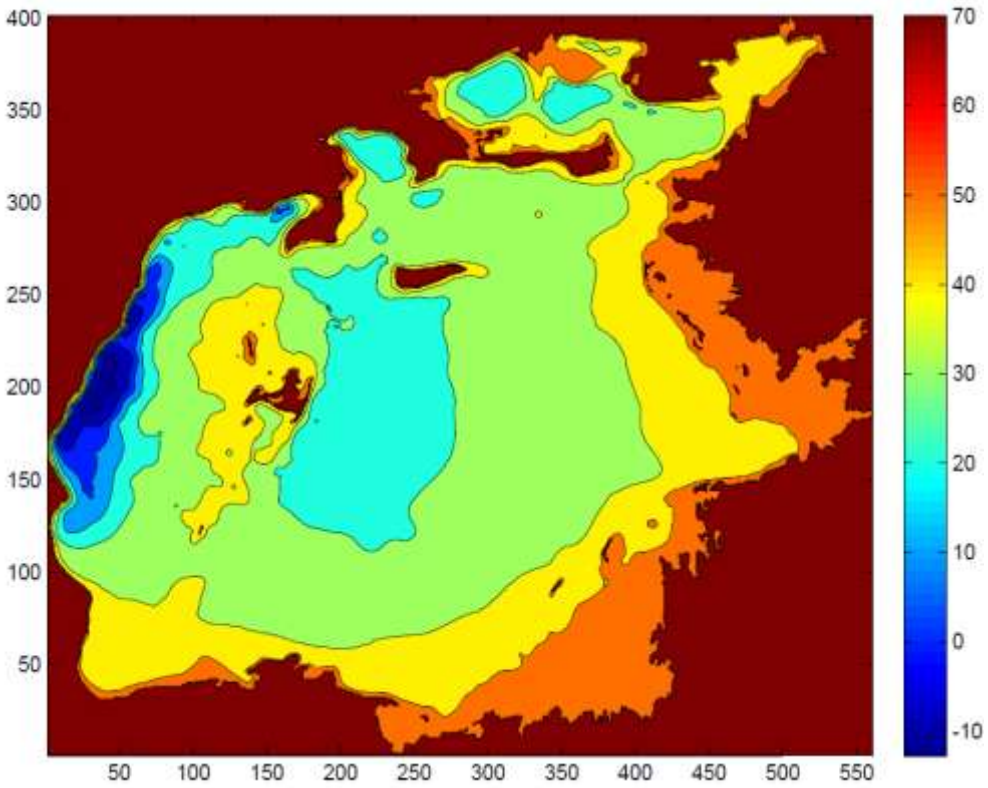

Figure 30: Bathymetry for Aral Sea for year 1960. Lower values near west shows steep depth of the Aral Sea in blue. Regions towards right are shallow.

Figure 31 shows the land-sea cover for year 1960 and 2000. The new dried-up area generated by desiccation is successfully included to avoid any vacuum in the model that may cause the model to blow off. Modified surface height for new desiccated land surfaces are included in the model. The desiccation of Aral Sea has caused the water surface to convert to barren land with sparse vegetation. Figure 32 shows the contrast in land-use categories for both years produced by artificially changing the surface characteristics of the desiccated

region. The sparse shrub land (orange color) is due to the desertification of the region. The change in vegetative cover over dried up water bodies to barren shrub land is due to the increase in salt content of the region. The vegetation has perished as a result of increased salinity followed by wind erosion in the region. Consequently, intense winds create dust storms in the region and salt is carried by the winds and dumped far off. Thus, many agricultural lands are destroyed by salinization and desertification [*Bosch*, 2007].

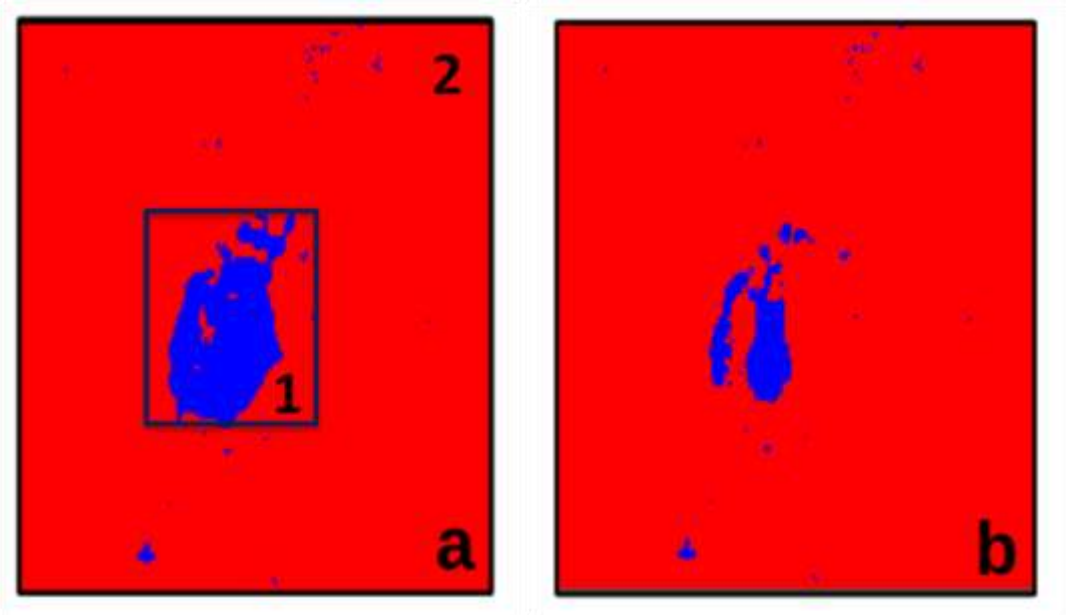

Figure 31: Land-sea cover shown for the innermost domain for (a) fully filled Aral Sea in year 1960 and, (b) desiccated Aral Sea in year 2000. In panel (a), box 1 shows the area covered over Aral Sea and box 2 is the area over the innermost domain except under box 1.

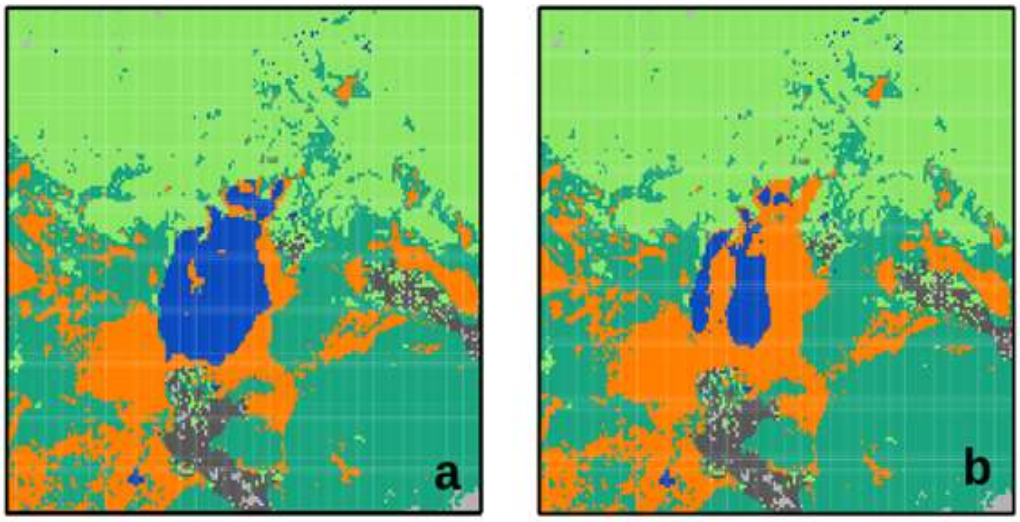

Figure 32: Land use Categories for (a) year 1960, (b) and year 2000 where blue is water, green is grassland, deep green is shrub land, orange is barren/sparse vegetation and grey is the irrigated crop land along the river paths.

5.5 Results

5.5.1 Sensitivity for temperature

We first analyze the simulated surface temperature from the WRF model output. Simulation results show inter-annual variability of average temperature within each decade. For simplicity, we show average temperature for a winter season decade to indicate the decadal climatology. Inter-annual variability of temperature, rainfall and snowfall are shown in Appendix A. Figure 33a and Figure 33b show the decadal mean of winter (November-January) average temperature from the innermost domain of 12 km for 1960 and 2000 decade respectively with their corresponding surface characteristics. 2000 decade shows

an overall warming in comparison to 1960 decade for the surrounding regions of Aral Sea. The warming trend appears to shift northwards. Over the desiccated regions of the Sea in 2000, the temperature has decreased. Figure 33a and Figure 33c have surface conditions from year 1960 but lateral boundary conditions are from 1960 and 2000 respectively. This comparison shows an increase in temperature over Aral Sea and the surrounding regions.

Figure 33d, e and f are similar to Figure 33a, b and c but for the summer simulation. It is obvious that summers are hotter than winters. The positive trend in warming is also evident in summers. The southern part in the domain is affected by warming more than the northern. Possible reason for the increase in temperature in southern part of Aral Sea can be the fact that the southern part has a land-cover consisting of barren/sparse vegetation and shrub land. The barren shrub land region in south of Aral Sea has more sensible heat flux in comparison to northern grassland regions and thus, higher temperature as shown in Figure 32. The regions of irrigated cropland along the path of rivers show lower temperature trends in comparison to neighboring regions. The desiccated regions of the Sea show increase in surface temperature due to the fact that dried-up land gets more heated in summers. However, the shallow Aral Sea depth in 2000 decade shows an increase in temperature, but the increase is not as intense as over the desiccated regions. Comparison of same surface conditions (year 1960) with different lateral boundary conditions shows increase in temperature, thus explaining overall warming in Central Asia.

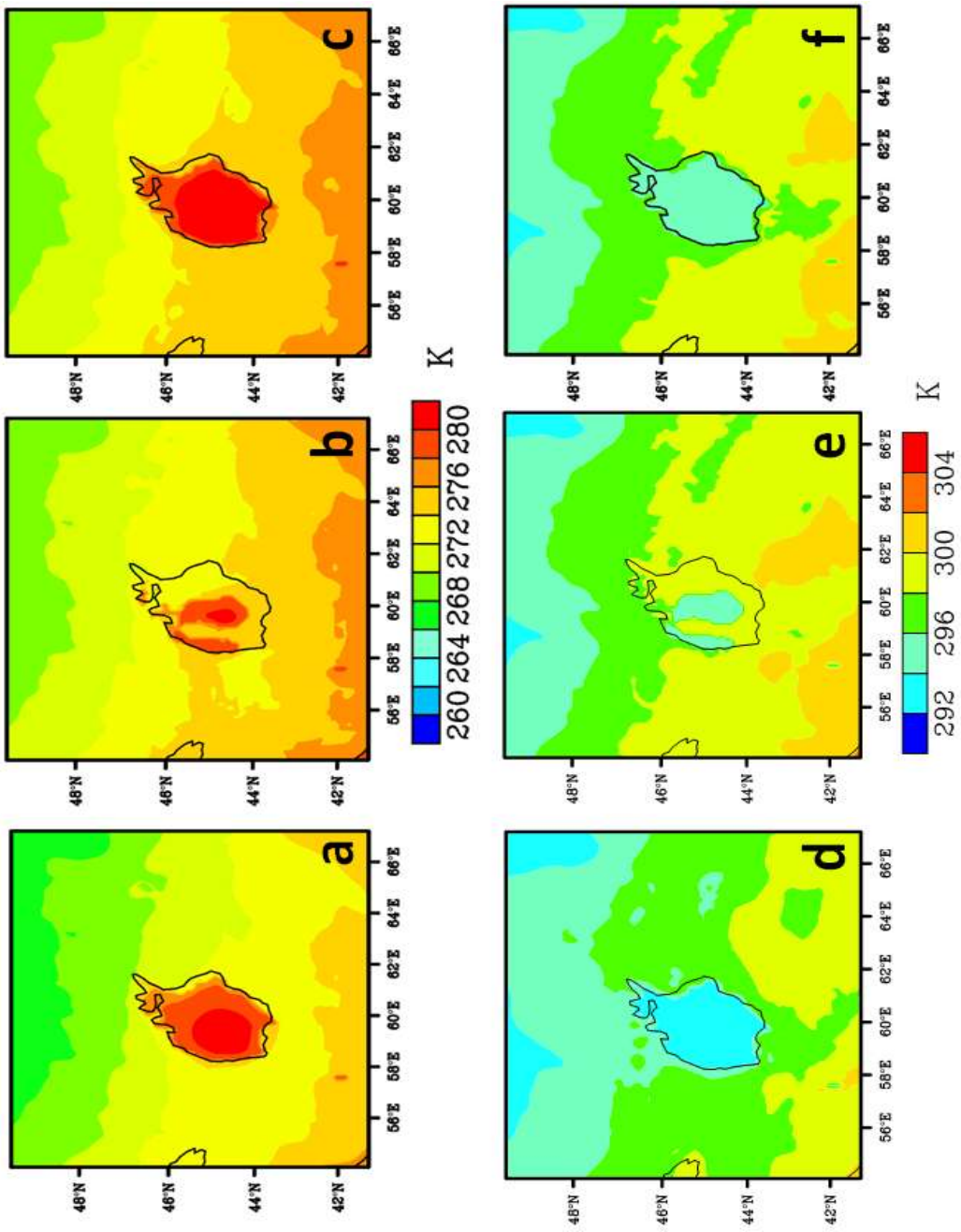

Figure 33: Average temperature for decadal winter with (a) surface from year 1960 and boundary conditions from 1960 decade, (b) surface from year 2000 and boundary conditions from 2000 decade, (c) surface from year 1960 and boundary conditions from 2000 decade. Figure 33d, e and f are similar to Figure 33a, b and c respectively but for summer season. .

Figure 34a, b and c show the difference plot of surface temperature for winter season for cases 1-2, 1-3 and 2-3 respectively based on Table 6. Similarly Figure 34d, e and f show similar plots for summer seasons. The shrinkage of the Sea should enhance the existing continental climate in the Central Asia region; instead, there is a positive wintertime and summertime temperature trend. The trend is more intense for winters than in summers. Winters show 2-3^{0}C increase in average temperature, whereas summers have 1-2^{0}C increase. This positive trend in temperature is confirmed by analysis of snow in later section. An important finding from the simulations show that while the desiccation of Aral Sea has significant impacts on the local climate over the confine of Aral Sea, the regional climate over the greater Central Asia on interdecadal time scale is more clearly influenced by the continental or global scale climate change on that time scale.

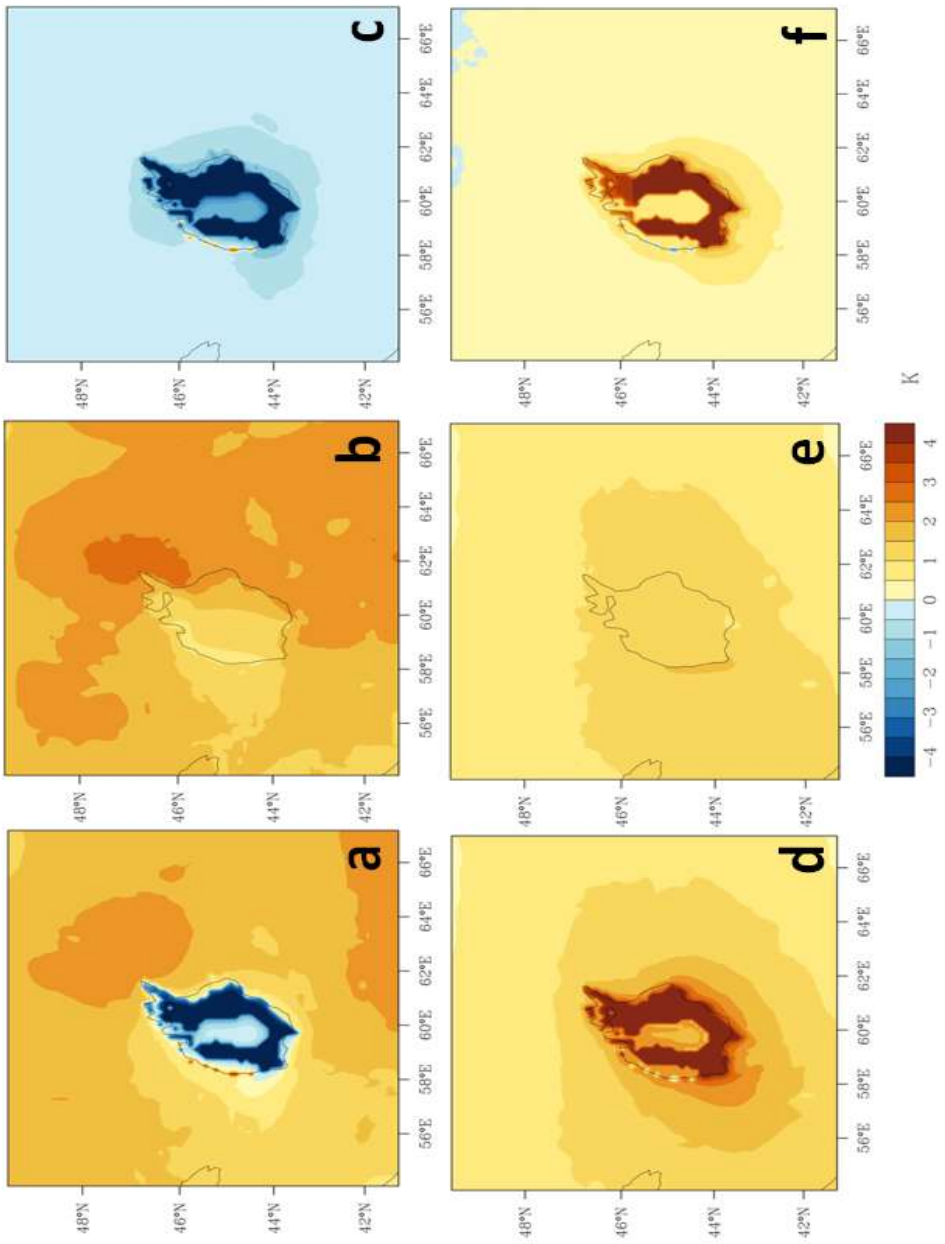

Figure 34: Difference plot for decadal mean temperature for winter season (November 1 – January 31) are shown in panel (a), (b) and (c) for cases 1-2, 1-3 and 2-3 respectively based on Table 6. Similarly, panel (d), (e) and (f) shows the difference plots for decadal mean temperature for summer season. (June 1 – August 31)

We show the time-series results only for winter as the largest trend values correspond to winter season. Figure 35 shows the model simulated daily temperature for winter season averaged over corresponding decades. Figure 35a refers to average over grid points with water mask over the Sea and Figure 35b refers to the average over land points in the domain. From Figure 35a, the mean temperature over both instances of Sea is almost constant, but there is significant daily variation of temperature. Comparison of surface temperature for 1960 and 2000 decade with constant surface from year 1960 shows an overall increase in daily mean temperature of around 2^0C. This mean temperature may be misguiding because we have relatively less grid points for 2000 decade in comparison to 1960 decade. However, over land points, the daily average winter temperature has increased from 1960 to 2000 decade for both instances when the surface is either from year 1960 or 2000. Figure 35b confirms that an overall warming in Central Asia has significantly influenced the regional climatology.

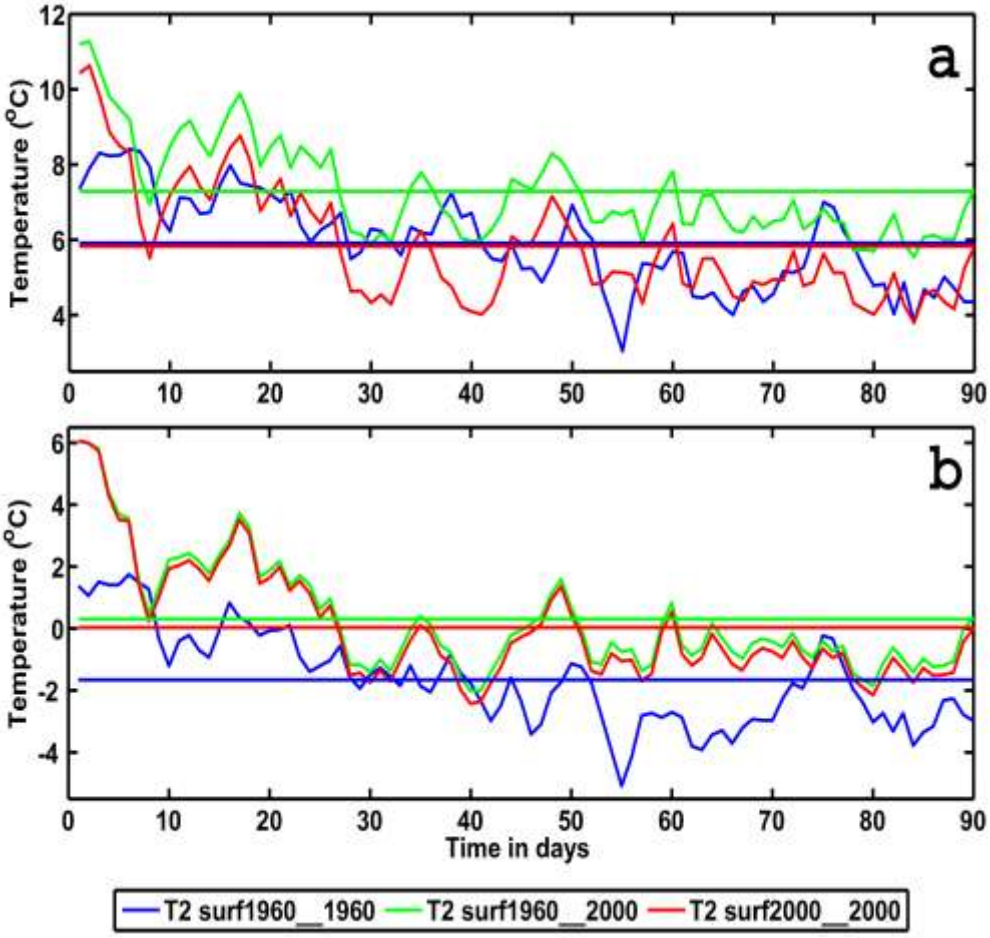

Figure 35: Time series for daily decadal mean temperature for a grid box of 144 km^2 for winter season (November 1 – January 31) over (a) Aral Sea spread, (b) area except Aral Sea. Blue line denotes case 1, red case 2 and green case 3 as discussed in Table 6.

Desiccation of Aral Sea has changed the Sea Surface Temperature (SST) over the period. Figure 34 shows that the winter SST of Aral Sea is declining, while the summer SST is rising. It is possible due to the fact that as the water levels are reducing, the Sea is warming and cooling off quickly [*Zavialov*, 2005].

It has affected the diurnal climate in the region. The regional climate has transformed to desert type with extreme climatic conditions (unlike in 1960 decade). Drying up of Aral Sea has also its influence on climate change around the region. In 1960s, the Central Asia region flourished with rich Aral Sea water. The Sea used to maintain the region's climate inhabitable by regulating the strong Siberian wind currents in winters and cooling the region in summers. With time, desiccation of the Sea has reduced the moisture content and contributed in warming up the climate of the region.

5.5.2 Sensitivity for rainfall

Figure 36 shows a similar plot as Figure 33 but for cumulative decadal average seasonal total rainfall (i.e. rainfall due to sub-grid and grid scale). Figure 36a and Figure 36b show cumulative seasonal rainfall for 1960 and 2000 decade for winters. The amount of rainfall over Aral Sea has reduced considerably due to the desiccation. If the desiccation had not happened, the total amount of winter rainfall would have increased (Figure 36c). This probably means that there is a positive influence of warming in Central Asia. The domain around Aral Sea does not show any explicit differences except some structural changes and redistribution of moisture. Figure 36(d, e, and f) and same as Figure 36(a, b, and c) but for summers. The summer rainfall does not show major impacts of warming.

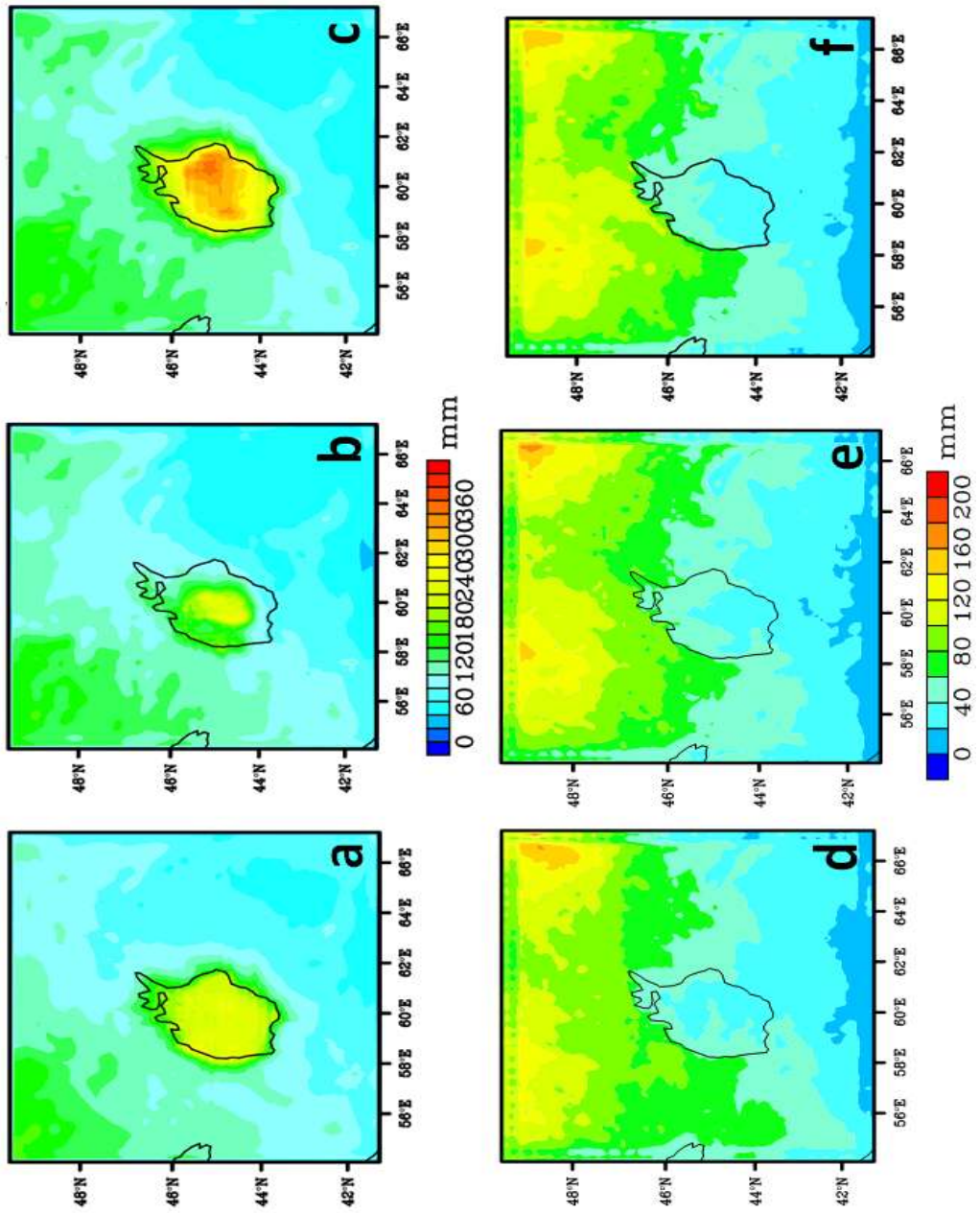

Figure 36: Cumulative rainfall for decadal mean winter season with (a) surface from year 1960 and boundary conditions from 1960 decade, (b) surface from year 2000 and boundary conditions from 2000 decade, (c) surface from year 1960 and boundary conditions from 2000 decade. Figure 36d, e and f are similar to Figure 36a, 5b and 5c respectively but for summer season. .

Figure 37 shows the difference plots of rainfall similar to Figure 34 for temperature in previous section. Difference plot shows that there is a reduction in rainfall with desiccation over Aral Sea. If the desiccation had not happened, the total amount of winter rainfall would have increased due to increase in evaporation of surface water caused by warming. Simulations show that while the shrinkage of Aral Sea has a dramatic impact on the precipitation over the confine of (former) Aral Sea, its effect on the precipitation over greater Central Asia is not necessarily greater than the typical interannual variability induced by the lateral boundary conditions. If the desiccation had not happened, the large-scale warming would have significantly increased the total amount of rainfall over the extent of Aral Sea.

Figure 38 shows the simulated average daily rainfall averaged over all 10 year winter seasons. Figure 38a is for the average over box 1 over Aral Sea and Figure 38b for box 2 for the rest of the region except box 1 as marked in Figure 31a. Comparing the daily rainfall for 1960 and 2000 decade with their respective surface characteristics, the daily rainfall has reduced significantly. If we had the same extent of Aral Sea surface as in year 1960 for year 2000, the daily rainfall amounts would have increased. The time-series for 2000 decade with and without Aral Sea desiccation shows similar trend. However, there is an increase in rainfall over the Sea for lateral boundary conditions from 2000 decade and surface conditions from year 1960. It happens due to increase in evaporation of surface

water caused by local warming. Region around Aral Sea shows daily differences in rainfall pattern but mean values does not change for both decades.

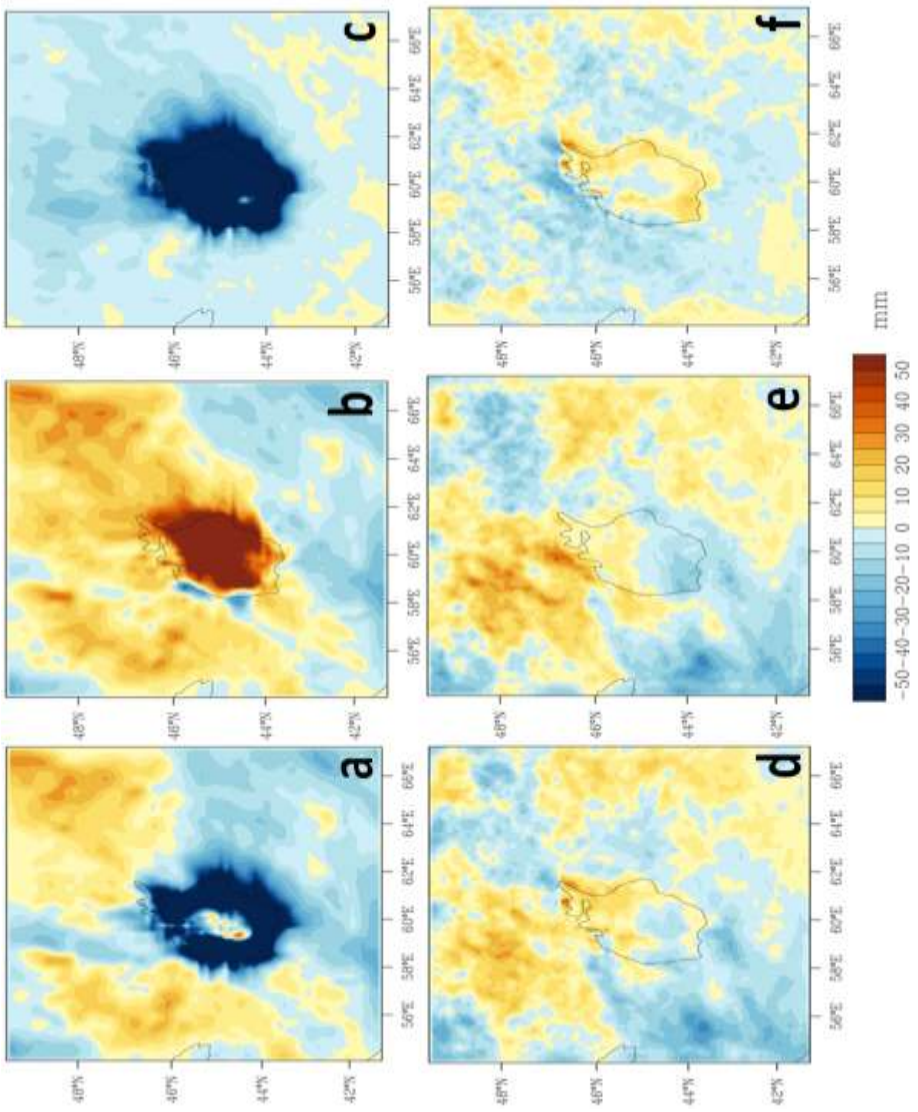

Figure 37: Difference plot for decadal mean rainfall for winter season (November 1–Jan 31) are shown in panel (a), (b) and (c) for cases 1-2, 1-3 and 2-3 respectively based on Table 6. Similarly, panel (d), (e) and (f) shows the difference plots for decadal mean rainfall for summer season. (June 1 – Aug 31).

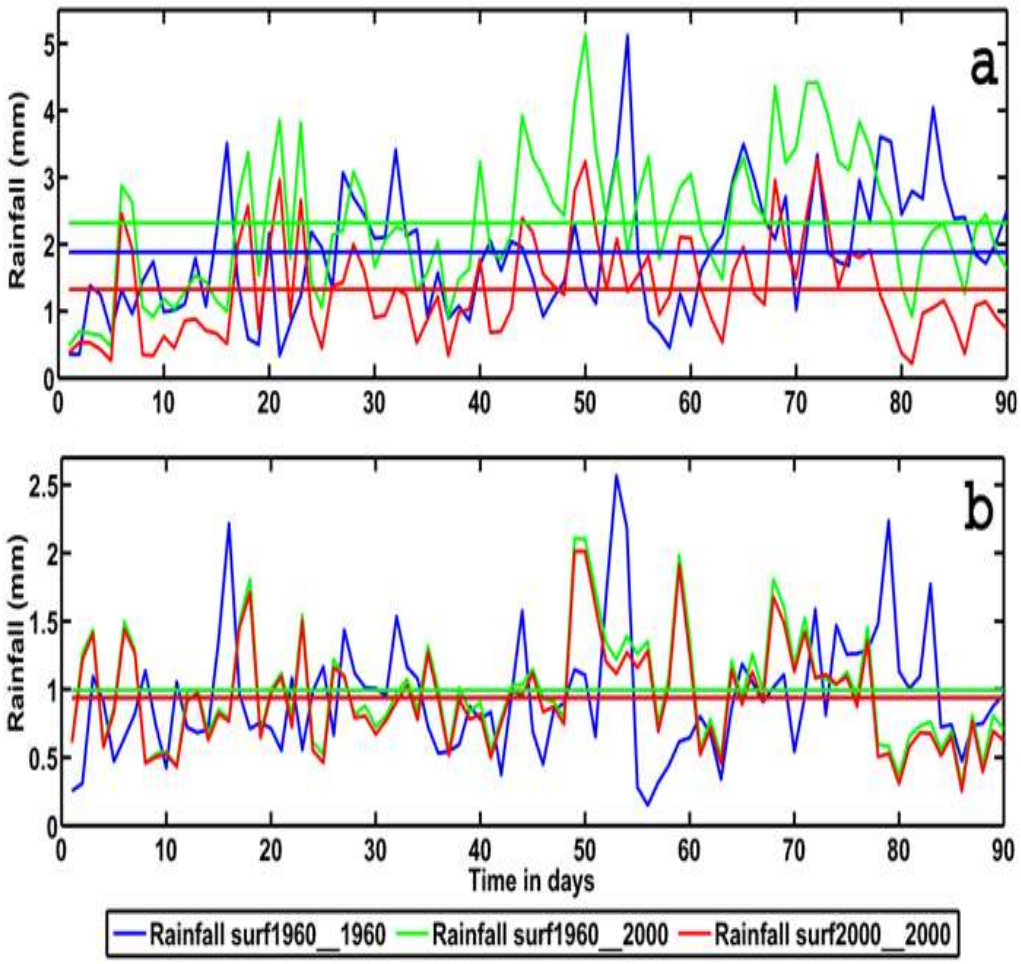

Figure 38: Time series for daily decadal mean rainfall for a grid box of 144 km^2 for winter season (November 1 – January 31) over (a) box 1, (b) box 2 in Figure 31a. Blue line denotes case 1, red case 2 and green case 3 as discussed in Table 6.

5.5.3 Sensitivity for snowfall

Figure 39 shows the cumulative snowfall for winter season averaged over respective decades. Since, it does not snow in summers; there are no figures for snowfall in summers. Interestingly, lake-effect snow is visible at the shore of Aral Sea. Aral shores have a lower temperature than Sea due to lake-effect snow and

the fact that land gets cooler quickly than water. Lake-effect snow is produced during cooler atmospheric conditions when cold winds move over warmer lake water. These winds pick up water vapor that deposit on the leeward shores and freezes. Desiccation has weakened the lake-effect snow as shown in Figure 39b. Warming in Central Asia has its influence in weakening the lake-effect snow. As seen in Figure 39c, even if the Aral Sea is filled with water for 2000 decade, the snow accumulation over the edges is not as significant as in 1960 decade. Simulations suggest that the limit of the snow cover in the domain has migrated northward. This result provides a confirmation of significant decadal warming in winters along with the weakening of lake-effect snow for Aral Sea.

Figure 40 shows the difference plots for decadal mean snowfall for winter season. Simulations show confirmation of *lake-effect snow* in winter seasons over the shores of (former) Aral Sea in 1960s. Figure 40a shows that desiccation has weakened the lake effect in the region. Change in lateral boundary conditions show that this lake-effect decreases with desiccation and overall warming in Central Asia. Aral shores have a lower temperature than Sea due to Lake-effect snow and the fact that land gets cooler quickly than water. These simulations provides a confirmation of significant interannual warming in winters along with the Aral sea shallowing.

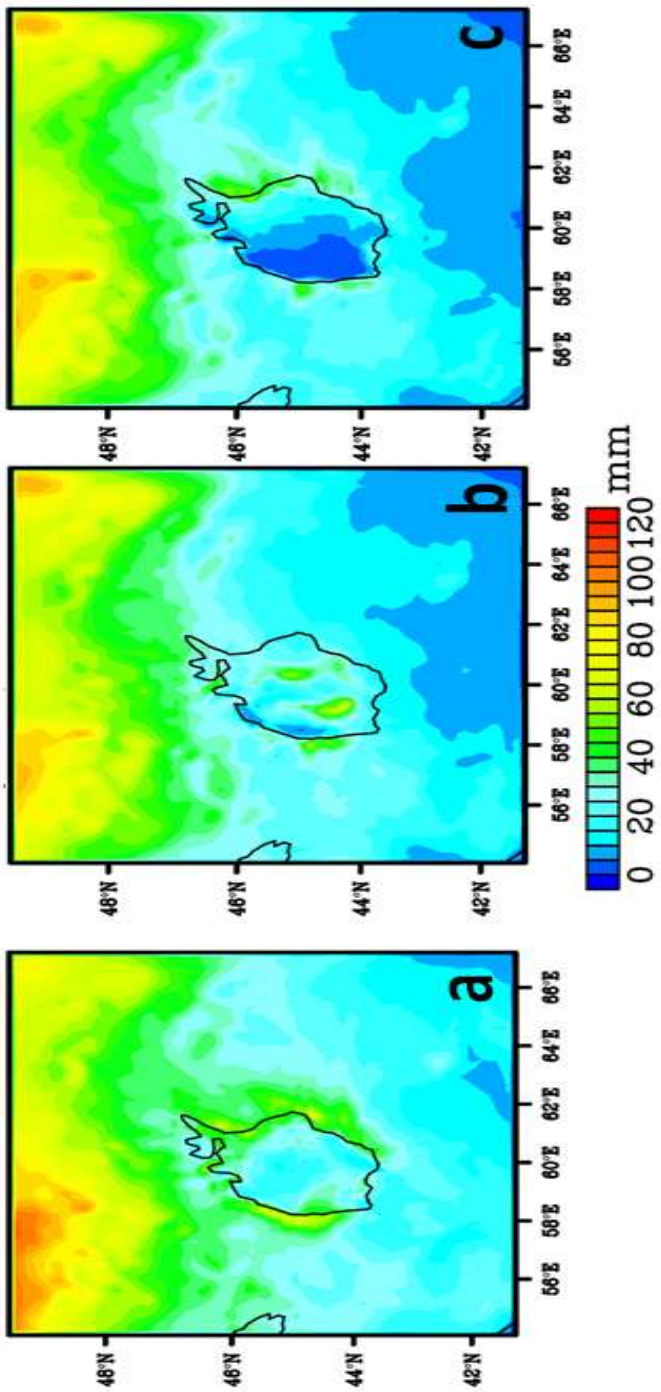

Figure 39: Cumulative decadal mean snowfall for winter season with (a) surface from year 1960 and boundary conditions from 1960 decade, (b) surface from year 2000 and boundary conditions from 2000 decade, (c) surface from year 1960 and boundary conditions from 2000 decade.

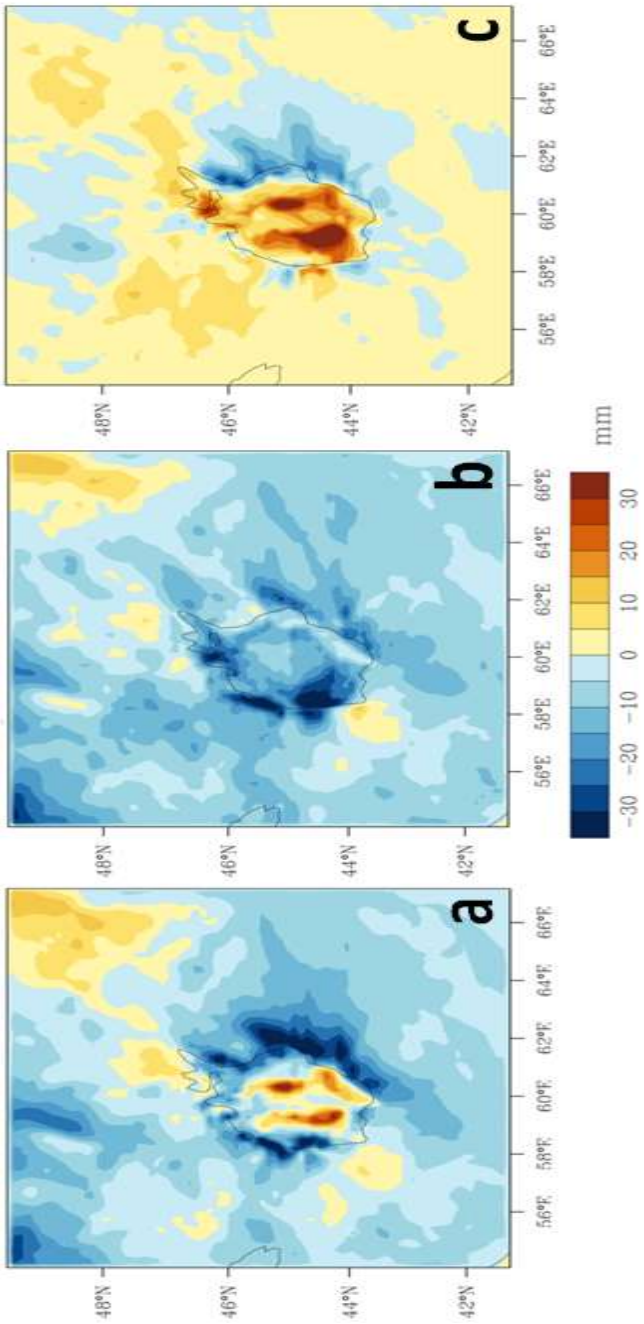

Figure 40: Difference plot for decadal mean snowfall for winter season (November 1 – January 31) are shown in panel (a), (b) and (c) for cases 1-2, 1-3 and 2-3 respectively based on Table 6.

Figure 41 is similar to Figure 38 but shows the time series of simulated daily snowfall. Snowfall has decreased over Aral Sea from 1960 to 2000 decade as shown in Figure 41a. Interestingly, comparing the differences in snowfall for land-cover from 1960 and 2000 year for 2000 decade meteorological conditions, simulations show less snowfall amounts for 1960 land-cover. This sensitivity test for daily snowfall amounts clearly shows the influence of regional warming in Central Asia region and particularly over the Aral Sea. The snowfall amounts for region around Aral Sea do not have significant differences as shown in Figure 41b and c except for some extreme events of snowfall that occur in 1960s. However, the mean for daily snowfall has decreased for 2000 decade in comparison to 1960 decade.

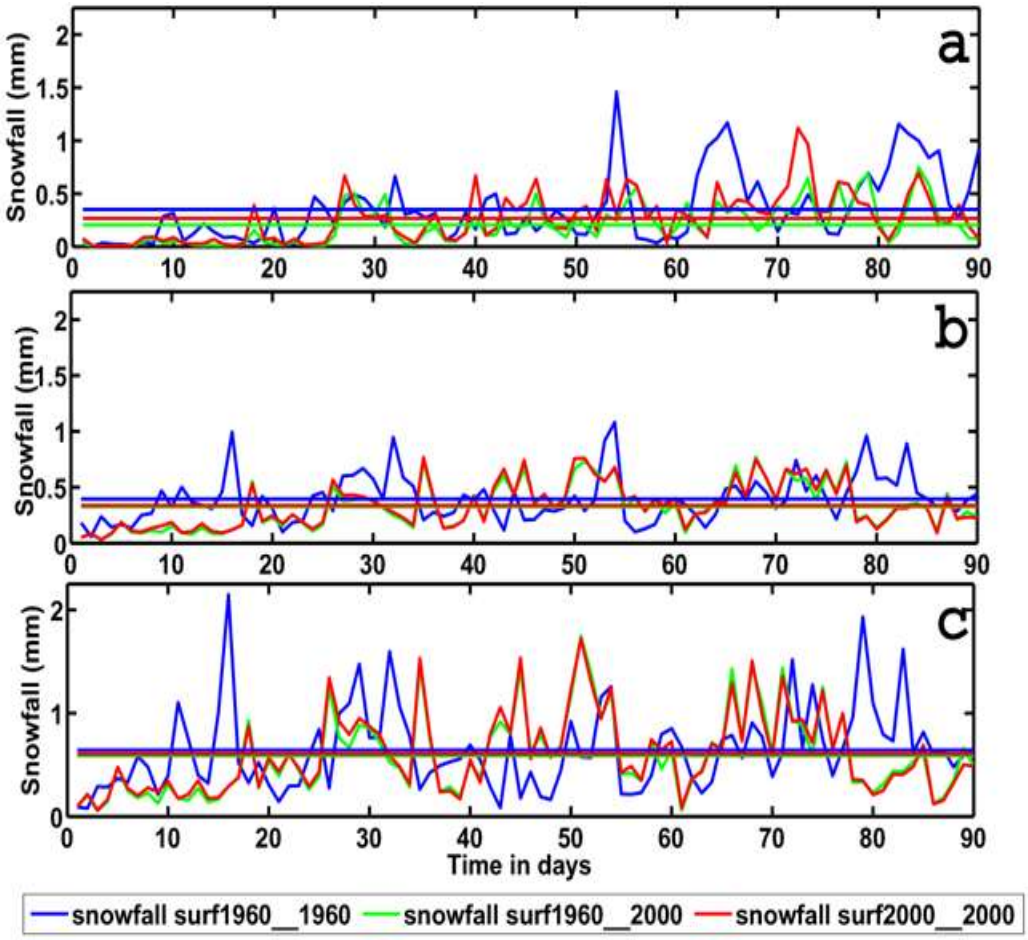

Figure 41: Time series for daily average decadal snowfall for 1 grid box of 144 km^2 for winter season (November 1 – January 31) over (a) box 1, (b) lower part of box 2 (below 47degN and excluding box 1), (c) upper part of box 2 (above 47degN) in Figure 31a. Blue line in the plot denotes case 1, red case 2 and green case 3 as discussed in Table 6.

5.6 Comparison with observations and statistical analysis

Figure 42 shows a comparison of decadal monthly data for temperature from Aralsk meteostation for summer season of 1960 decade. The co-ordinates of

the station are 46deg47'N, 61deg40'E. Since observations are monthly mean values, seasonal simulations are averaged over individual months and all summer seasons are stitched together to produce a time series. Thus, both observations and simulations are plotted together for a comparison. Further statistics show that the root mean square error is approximately 4.89^0C. Figure 43 shows a scatter plot. The simulation data shows a good fit with slope of 0.7. The fit is close to a perfect linear curve. Correlation coefficient is a good measure of linear association of data points. Correlation coefficient for summer temperature is 79.25%. Statistically, this value shows that our simulation data is close to observations.

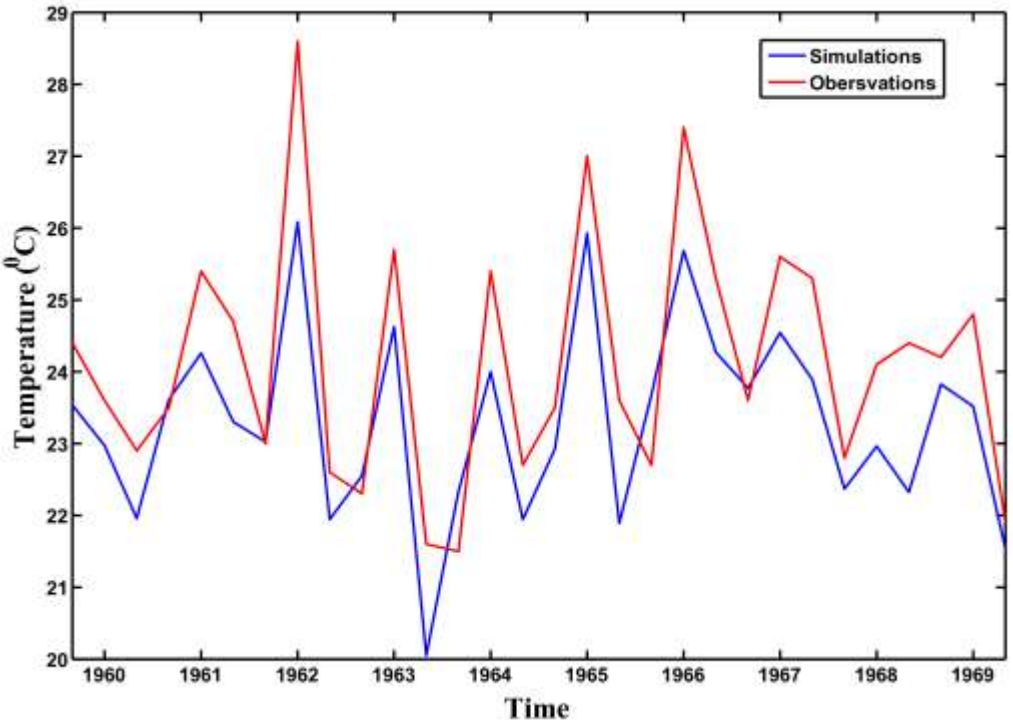

Figure 42: Time series comparison for monthly simulated temperature with observations for Aralsk station located at north of Aral Sea for summer season from June-August, 1960-69.

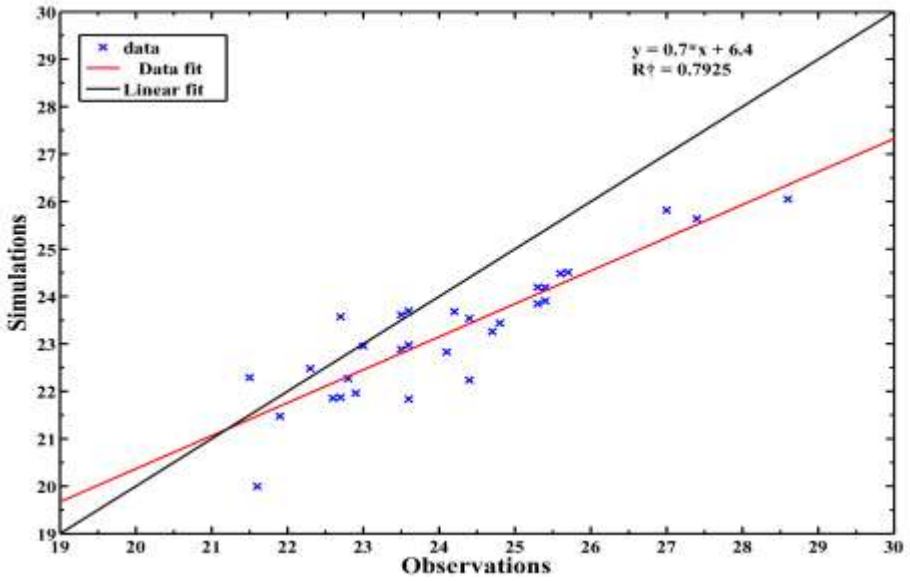

Figure 43: Scatter plot for summer monthly mean temperature with its data fit and linear fit for June-August, 1960-69. The temperature has a 79.25% correlation.

Similarly, a comparison of simulated winter temperature is done with observations. Figure 44 shows the time series of monthly simulated and observed winter temperature at Aralsk station for 1960 decade. The trend is captured perfectly in simulations. However, there is a mean shift in simulated time-series of winter temperature in comparison to observations. We believe this shift in mean temperature could possibly be due to the increased salinity of water of the Aral Sea influencing the simulation results. (Note that the simulations does not account for increase in salinity of the Sea). Figure 45 shows the scatter plot for winters similar to Figure 43. The data fits appropriately on a line. However, the fit is not as perfect as in summers. Correlation of 71.3% is found for winters. Another reason of this difference could be the fact that winters get more affected from the overall warming in Central Asia in comparison to summers.

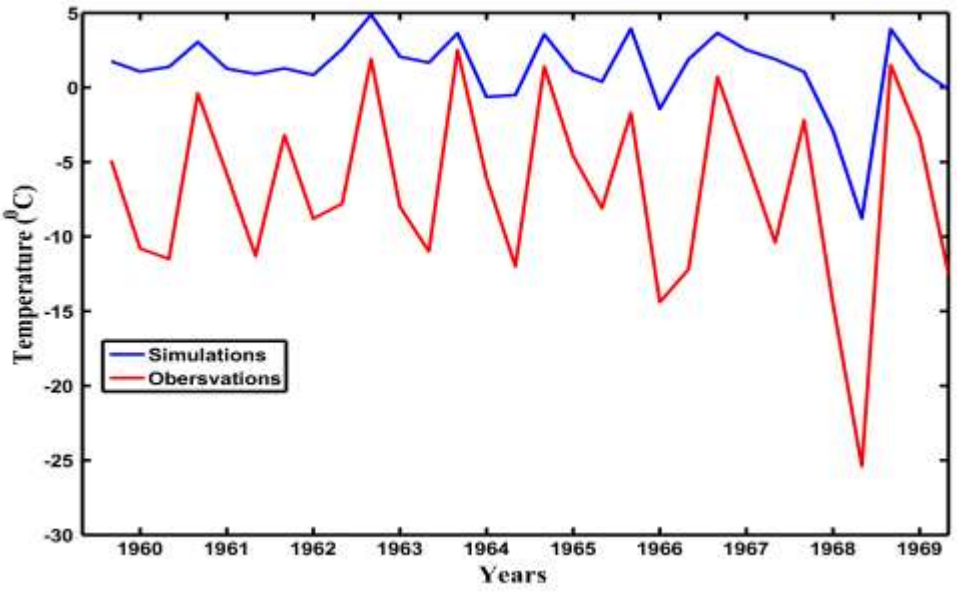

Figure 44: Time series comparison for monthly simulated temperature with observations for Aralsk station located at north of Aral Sea for winter season from November-January, 1960-69.

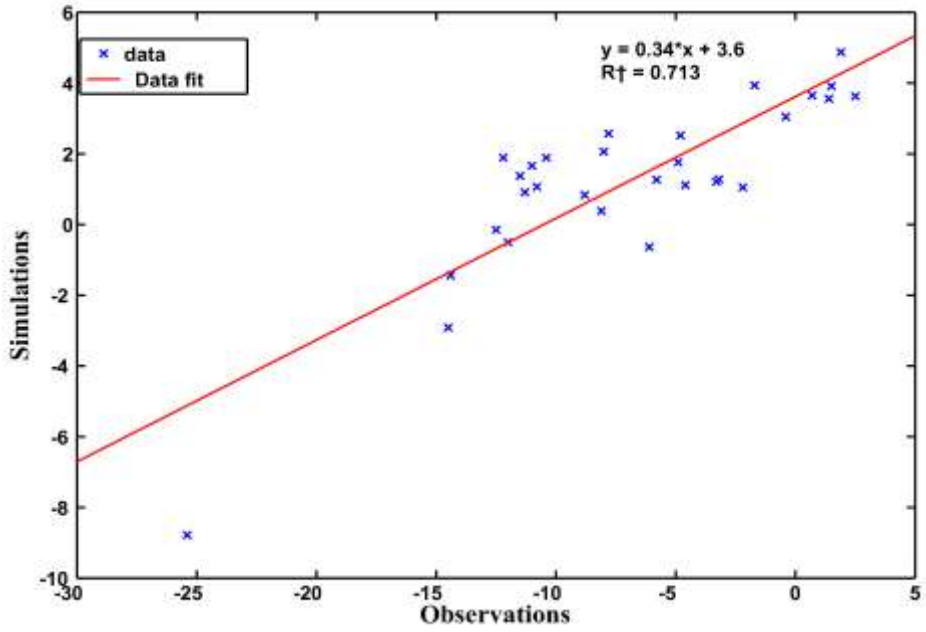

Figure 45: Scatter plot for winter monthly mean temperature with its data fit from November-January, 1960-69. The temperature has a 71.3% correlation.

5.7 Conclusions for Aral Sea Study

This chapter performs another set of sensitivity tests to study the impact of change in surface characteristics caused by desiccation of Aral Sea in Central Asia on precipitation and temperature. A series of climate downscaling experiments were performed for 1960 and 2000 decades for both winter and summer seasons using WRF model at 12 km horizontal resolution. Important findings from this sensitivity study are given below:

1. Sensitivity tests show that change in surface characteristics of land cover and landmask have an influence on rainfall, snowfall and temperature due to change in heat fluxes, moisture fluxes and albedo.
2. Numerical simulations show that while the desiccation of Aral Sea has significant impacts on the local climate over the confine of Aral Sea, the regional climate over the greater Central Asia on interdecadal time scale is more clearly influenced by the continental or global scale climate change on that time scale. Comparison of 1960 and 2000 decade simulations show that largest trend in warming is for winter season with an increase of 2-3^0C in average temperature, whereas summers have 1-2^0C increase.
3. Simulations show confirmation of lake-effect snow in winter seasons over the shores of (former) Aral Sea in 1960s and this effect decreases with desiccation and overall warming in Central Asia. Nevertheless, the warming has caused reduction in snowfall over water surface of Aral Sea.
4. Sensitivity tests indicates that while the shrinkage of Aral Sea has a dramatic impact on the precipitation over the confine of (former) Aral Sea

itself, its effect on the precipitation over greater Central Asia is not necessarily greater than the typical interannual variability induced by the lateral boundary conditions in the model. Results indicate that desiccation of Aral Sea has led to a local reduction in rainfall over the extent of Sea. Simulations show that if the desiccation had not happened, the large-scale warming would have significantly increased the total amount of rainfall over the extent of Aral Sea.

5. Comparison of simulations with station observations shows positive bias in temperature. This bias is possibly due to the fact that the station is located at a land surface which is in close proximity to the shores of Aral Sea.

Chapter 5

6. SUMMARY

Primarily, the outcome of this sensitivity study is a cautionary tale for all regional climate model users. Results from this study suggest the need for the climate community to perform rigorous sensitivity tests to find an appropriate resolution to run a WRF model depending on the requirements of the study.

This study investigated the dependence of simulated rainfall on model resolution in a series of climate downscaling experiments to test our primary hypothesis that as the grid spacing is decreased, the simulations produce results closer to observations. In contrast to our hypothesis, it was found that winter seasonal mean rainfall for different sub-domains of Arizona shows a wetter bias with the refinement of horizontal resolution from 12 to 6 km. This conclusion holds regardless of whether the subgrid-scale cumulus parameterization is turned on or off in the 6 km run. At that resolution, results from sensitivity tests of twin experiments with convective scheme turned on and off produced approximately the same amount of rainfall for Arizona and its sub-domains. When cumulus parameterization is turned off, the rainfall produced by grid-scale processes increases to compensate for the absence of the contribution from (parameterized) subgrid-scale convection. A further refinement of the grid size to 3 km leads to relatively minor changes in the seasonal mean rainfall. However, a comparison with the observed seasonal mean rainfall from the PRISM data revealed that the rainfall simulated by the 6 km and 3 km runs is excessive, while that produced by

the 12-km-grid simulations is closer to observation. Time series analyses of wintertime rainfall simulations over observation stations also show a significant increase in the total rainfall at all resolutions. The results show that WRF is able to simulate almost all of the large-scale features of the heavy rainfall events at different resolutions. However, large differences were seen in the temporal distribution. Comparing different resolutions with station datasets, it is seen that the 12 km resolution simulated the regional rainfall most accurately among all the resolutions.

Thus, our hypothesis that as the grid spacing is decreased, the simulations produce results closer to observations turns not true for rainfall. A plausible interpretation is that when WRF was first developed the benchmark simulations used to fine tune the model against observation were run at a considerably coarser resolution than our 3 or 6 km. Then, a greater deviation from observation can possibly be produced by the runs with a refined resolution as the parameterization schemes for rainfall in the model are not resolution-independent. However, the hypothesis is true for temperature. Temperature was simulated accurately at all resolutions with more accuracy at 3 km resolution. The contrast in rainfall and temperature is due to the reason that unlike temperature, rainfall is a by-product of the prognostic variable and is a result of many climate processes in the model that requires calibration of several variables in the equations and physics. So, WRF model produces a systematic local bias for each station that varies with time.

The hypothesis is further tested with vertical velocity as the study also demonstrates the resolution dependence for the variance of vertical velocity, a

variable that is intimately related to the processes (thermal convection and/or mechanical/topographic lifting) for rainfall production. At 12 km resolution, the maximum of the variance of vertical velocity is mainly associated with large-scale topographic lifting over the mountainous northern Arizona. With a refinement of grid size to 3 km, streaks of high variance of vertical velocity begin to emerge in southern Arizona where mountains are shorter and smaller in horizontal scale. An analysis of the high frequency behavior of rainfall indicates that the 3 km runs produced significantly more extreme rainfall events within Arizona that are missing or muted in the 12 km runs.

In the second part of the study we performed sensitivity tests to investigate the impact of change in surface characteristics on rainfall and temperature using Aral Sea as a test-bed. For this sensitivity study, a horizontal 12 km resolution was chosen based on the analysis from our first part of the study [for more details, *Sharma and Huang*, 2012]. This study showed that a reduction in vegetation cover and drying of water bodies decreases rainfall and increases warming over the confine of (former) Aral Sea itself. However, its effect on the precipitation over greater Central Asia is not necessarily greater than the inter-annual variability induced by the lateral boundary conditions in the model and large scale warming in the region. From simulation results of winter and summer seasons of post-1960 era for two different decades (1960's and 2000's), it is observed that there is a positive trend in overall warming in Central Asia. This trend has produced changes in regional moisture and temperature distribution. As anticipated, our secondary hypothesis tested true. However, these sensitivity tests

brought greater amount of insight about the climatology of the region. The warming changes in climate at regional and local scales have caused an ecological imbalance in the region. This research is an important step to suggest measures and give recommendations to the regional government to take steps for restoring the Sea. The results of this sensitivity study are expected to contribute significantly to the ecosystem management of the Aral region. This study will help the scientific community to perform similar experiments for other semi-arid regions of the world.

Thus, this sensitivity study is a cautionary tale for WRF users. The study is beneficial for hydrological analysis and its applications like runoff modeling or extreme events analysis like floods, as these studies require rainfall data at relatively very high resolution.

REFERENCES

Bortnik, V.N.; Chistyaeva, S. P.;. (1990). Hydrometeorology and hydrochemistry of the seas of the USSR. Vol. 7. The Aral Sea. Gidrometeoizdat, Leningrad, 194 pp (in Russian).

Bosch, K.; Erdinger, L.; Ingel, F.; Khussainova, S.; Utegenova, E.; Bresgen, N.; Eckl, P. M.;. (2007). Evaluation of the toxicological properties of ground- and surface-water samples from the Aral Sea basin, Sci Total Environ. 374, 43–50.

Bryson, R.A.; Hare, F. K.;. (1974). The climates of North America, Elsevier, New York. pp. 1–47.

Bukovsky, M. S.; Karoly, D. J.;. (2009). Precipitation Simulations Using WRF as a Nested Regional Climate Model. *J. Appl. Meteor. Climatol.* , 48, 2152–2159.

Caldwell, P. M.; Chin, H-N. S.; Bader, D. C.; Bala, G.;. (2009). Evaluation of a WRF dynamical downscaling simulation over California. *Climatic Change* , 95, 499–521.

Chub, V.E.;. (2000). Izmenenie klimata i ego vliyanie na prirodno- resursniy potential Respubliki Uzbekistan. Glavgidromet RUz, Tashkent (in Russina).

Collier, J. C.; Zhang, G. J.;. (2007). Effects of Increased Horizontal Resolution on Simulation of the North American Monsoon in the NCAR CAM3: An Evaluation Based on Surface, Satellite, and Reanalysis Data. *J. Climate* , 20, 1843–1861.

Daly, C.; Kittel, T. G. F.; McNab, A.; Gibson, W. P.; Royle, J. A.; Nychka, D.; Parzybok, T.; Rosenbloom, N.; Taylor, G.;. (2000). Development of a 103-year high-resolution climate data set for the conterminous United States, in Proc. 12th AMS Conf. on Applied Climatology, Amer. Meteorol. Soc., Ashville, NC, May 8-11. pp. 249-252.

Duffy, P. B. (2006). Simulations of present and future climates in the western United States with four nested regional climate models. *J. Climate* , 19, 873–895.

Duliere, V.; Zhang, Y.; Salathe, E. P. (2011). Extreme precipitation and temperature over the U.S. Pacific Northwest: a comparison between observations, reanalysis data, and regional models. *J. Climate* , 24, 1950-

1964.

Duliere, V.; Zhang, Y.; Salathe, E. P.;. (2011). Extreme precipitation and temperature over the U.S. Pacific Northwest: a comparison between observations, reanalysis data, and regional models. *J. Climate* , 24, 1950-1964.

Hurrell; (1995). Decadal trends in the North Atlantic Oscillation – Regional temperatures and precipitation. *Science*, 269: 676–679.

Gibson, W. P.; Daly, C.; Kittel, T.; Nychka, D.; Johns, C. ; Rosenbloom, N.; McNab, A.; Taylor, G.;. (2002). Development of a 103-year high-resolution climate data set for the conterminous United States, in Proc. 13th AMS Conf. on Applied Climatology, Amer. Meteorol. Soc., Portland, OR, May 13-16., (pp. pp. 181-183).

Gilliland, E. K.; Rowe, C. M.;. (2007). A comparison of cumulus parameterization scheme in the WRF model, Proceedings of the 21th Conference on Hydrology, San Antonio, Texas.

Giorgi, Filippo; (1990). Simulation of Regional Climate Using a Limited Area Model Nested in a General Circulation Model. *J. Climate*, 3, 941–963.

Giorgi, F. (2001). Emerging patterns of simulated regional climatic changes for the 21st century due to anthropogenic forcings. *Geophys. Res. Lett.* , 28, 3317-3320.

Giorgi, F.; Bates.;(1989). A regional climate model for the western United States, *Climatic Chang*e, 15, 383-422.

Giorgi, F.; Marinucci, M. (1996). An investigation of the sensitivity of simulated precipitation to model resolution and its implications for climate studies. *Mon. Wea. Rev.* , 124, 148–166.

Giorgi, F., and coauthors, 2001: Emerging patterns of simulated regional climatic changes for the 21st century due to anthropogenic forcings, *Geophys. Res. Lett*., **28**, 3317-3320.

Haltiner, G.J.; Williams, R. T.; (1980). Numerical Prediction and Dynamic Meteorology (2nd ed.), *John Wiley & Sons*, 477pp.

Kain, J. S. (2004). The Kain-Fritsch convective parameterization: An update. *J. Appl. Meteor.* , 43, 170–181.

Kain, J. S. (2004). The Kain-Fritsch convective parameterization: An update. *J.*

Appl. Meteor. , 43, 170–181.

Kalnay, E.; Kanamitsu, M.; Kistler, R.; Collins, W.; Deaven, D.; Gandin, L.; Iredell, M.; Saha, S.; White, G.; Woollen, J.; Zhu, Y.; Chelliah, M.; Ebisuzaki, W.; Higgins, W.; Janowiak, J.; Mo, K.C.; Ropelewski, C.; Wang, J.; Leetmaa, A.; Reynolds, R.; Jenne, R.; Joseph, D.;. (1996). The NCEP/NCAR 40-year reanalysis project. *Bull. Amer. Meteor. Soc.* , 77, 437-471.

Khan, V. M.; Vilfand, R.M.; Zavialov , P.O.;. (2004). Long-term variability of air temperature in the Aral Sea region. *Journal of Marine Systems* , 47, 25–33.

Knutson, T. R.; J. J. Sirutus, S. T. Garner, I. M. Held, R. E. Tuleya; (2007). Simulation of the recent multidecadal increase of Atlantic hurricane activity using a 18-km-grid regional model, *Bull. Am. Meteor. Soc*., **88**, 1549-1565.

Kim, J. (2004). A projection of the effects of the climate change induced by increased CO2 on extreme hydrologic events in the western U.S. *Climatic Change* , 68, 153–168.

Kistler, R.; Kalnay, E.; Collins, W.; Saha, S.; White, G.; Woollen, J.; Chelliah, M.; Ebisuzaki, W.; Kanamitsu, M.; Kousky, V.; Dool, H. van den; Jenne, R.; Fiorino, M.;. (2001). The NCEP-NCAR 50-Year Reanalysis: Monthly Means CD-ROM and Documentation. *Bull. Amer. Meteor. Soc.* , 82, 247-267.

Knutson, T. R.; Sirutus, J. J.; Garner, S. T.; Held, I. M.; Tuleya, R. E.;. (2007). Simulation of the recent multidecadal increase of Atlantic hurricane activity using a 18-km-grid regional model. *Bull. Am. Meteor. Soc.* , 88, 1549-1565.

Laprise, R.; (1992). The Euler equation of motion with hydrostatic pressure as an independent variable. *Monthly weather review*, 120, 197.

Leung, L. R. (2003). Hydroclimate of the western United States Based on observations and regional climate simulations of 1981–2000. Part I: Seasonal statistics. *J. Climate* , 16, 1892–1911.

Leung, L.; Yun Qian, Ruby;. (2003). The Sensitivity of Precipitation and Snowpack Simulations to Model Resolution via Nesting in Regions of Complex Terrain. *J. Hydrometeor.* , 4, 1025–1043.

Lin, J.-L.; Mapes, B. E.; Weickmann, K. M.;. (2008). North American monsoon and convectively coupled equatorial waves simulated by IPCC AR4 coupled GCMs. *J. Climate* , 21, 2919-2937.

Lo, J. C.-F.; Yang, Z.-L.; Pielke, R. A. (2008). Assessment of three dynamical climate downscaling methods using the Weather Research and Forecasting

(WRF) model. *J. Geophys. Res.* , 113, D09112, doi:10.1029/2007JD009216.

Mariotti, A., N. Zeng, and coauthors; (2008). Mediterranean water cycle changes: transition to drier 21st century conditions in observations and CMIP3 simulations, *Environ. Res. Lett*, **3**, 044001, doi:10.1088/1748-9326/3/4/044001.

Marshall, J., R. A. Plumb (2008), Atmosphere, ocean, and climate dynamics: An introductory text, *Elsevier Inc*.

Mercader, J. (2007). Sensitivity of precipitation forecasts to cumulus parameterizations in Catalonia (NE Spain), WRF Users' Workshop, NCAR, June 2007.

Micklin, P. (2002). Water in the Aral Sea Basin of Central Asia: Cause of Conflict or Cooperation?, In Eurasian Geography and Economics., (pp. 43, 505-528).

Muminov, F.A.; Inagatova, I. I.; (1995). Inagatova (1995), Variability of Central Asian Climate, SANIGMI, Tashkent., (pp. 215 pp., (in Russian)).

Perera, J. (1993). A sea turns to dust. *New Sci.* , 23, 24–27.

Pidwirny, M. (1999). Fundamentals of Physical Geography, Department of Geography, Okanagan University.

Raucher, S.; Coppola, E.; Piana, C.; Giorgi, F.;. (2010). Resolution effects on regional climate model simulations of seasonal precipitation over Europe. *Clim. Dynam.* , 35, 685-711.

Rockel, B.; Castro, C. L.; Pielke, R. A.; Storch, H. von; Leoncini, G.;. (2008). Dynamical downscaling: Assessment of model system dependent retained and added variability for two different regional climate models. *J. Geophys. Res.* , 113, D21107, doi:10.1029/2007JD009461.

Seager, R., M. Ting, I. Held, Y. Kushnir, J. Lu, G. Vecchi, H.-P. Huang, N. Harnik, N.-C. Lau, C. Li, J. Velez, and N. Naik (2007). Model projections of an imminent transition to a more arid climate in southwestern North America, *Science*, *316*, 1181-1184.

Sellers, W. D. (1960). Arizona Climate, the University of Arizona Press, Tucson, Arizona.

Sharma, A.; Huang, H.-P.; (2012). Regional Climate Simulation for Arizona: Impact of Resolution on Precipitation. *Advances in Meteorology*, 13 pages,

doi:10.1155/2012/505726.

Sheppard, P.R.; Comrie, A. C.; Packin, G. D.; Angersbach, K.; Hughes, M. K.;. (2002). The climate of the U.S. Southwest. Climate Research. 21, 219-238.

Skamarock, W. C. (2008). A description of the Advanced Research WRF version 3. NCAR Tech., (pp. Note NCAR/TN-4751STR, 113 pp.).

Small, Eric E.; Giorgi, F.; Sloan, L. C.; Hostetler, S.;. (2001). The Effects of Desiccation and Climatic Change on the Hydrology of the Aral Sea. *J. Climate* , 14, 300–322.

Smith, J.A., D.J.Seo, M.L.Baeck, and M.D.Hudlow. (1996). An intercomparison study of NEXRAD precipitation estimates. *Water Resour. Res*. 32:2035–2045.

Stensrud, D. J. (2007), Parameterization schemes: keys to understanding numerical weather prediction, *Cambridge University Press*, UK.

Urrutia, R.; Vuille, M.;. (2009). Climate change projections for the tropical Andes using a regional climate model: temperature and precipitation simulations for the end of the 21st century. *J. Geophys. Res.* , 114, doi:10.1029/2008JD011021.

Wang, X., et al., (2008). A Hybrid ETKF–3DVAR Data Assimilation Scheme for the WRF Model. Part II: Real Observation Experiments. *Mon. Wea. Rev*., 136, 5132–5147.

Woodhouse, C. A. (1997). Winter climate and atmospheric circulation patterns in the Sonoran Desert region. *Int. J. Climatol.* , 17, 859-873.

Wicker, L. J.; Skamarock, W. C., (2002). Time splitting methods for elastic models using forward time schemes, *Mon. Wea. Rev.*, *130*, 2088–2097.

Zavialov, P. O. (2005). Physical Oceanography of the dying Aral Sea, Springer-Verlag, Berlin., (pp. 146 pp., ISBN: 3-540-22891-8, 2005).

Zavialov, P.O.; (2010). Physical oceanography of the Large Aral Sea. IN: Aral Sea Environment. *Hdb Env Chem. Springer-Verlag*, A.G. Kostianoy, A.N. Kosarev (Eds).

APPENDIX A

FIGURES FOR EACH WINTER AND SUMMER SIMULATIONS FROM ARAL SEA STUDY.

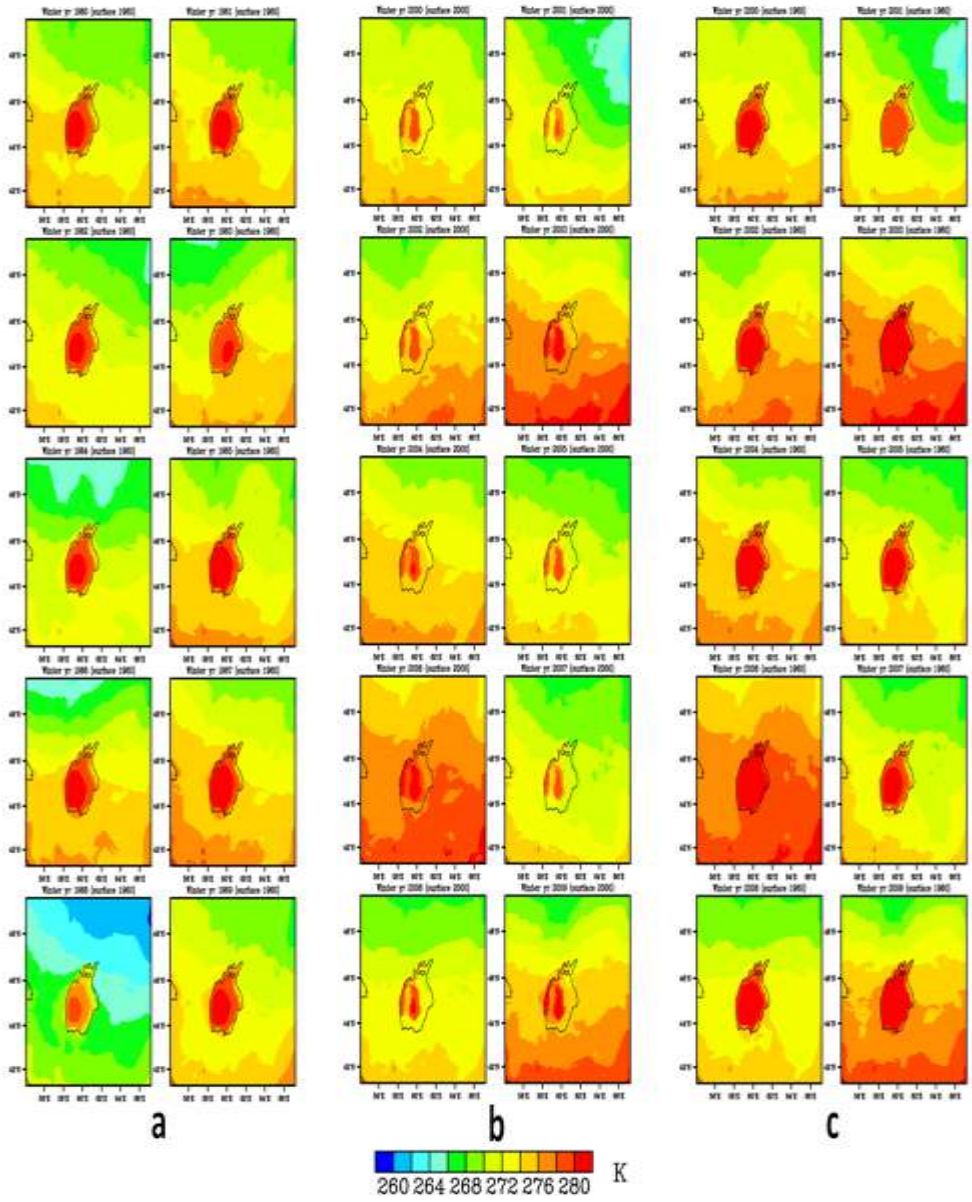

Figure 46: Average temperature for each winter with (a) surface from year 1960 and boundary conditions from 1960 decade, (b) surface from year 2000 and boundary conditions from 2000 decade, (c) surface from year 1960 and boundary conditions from 2000 decade.

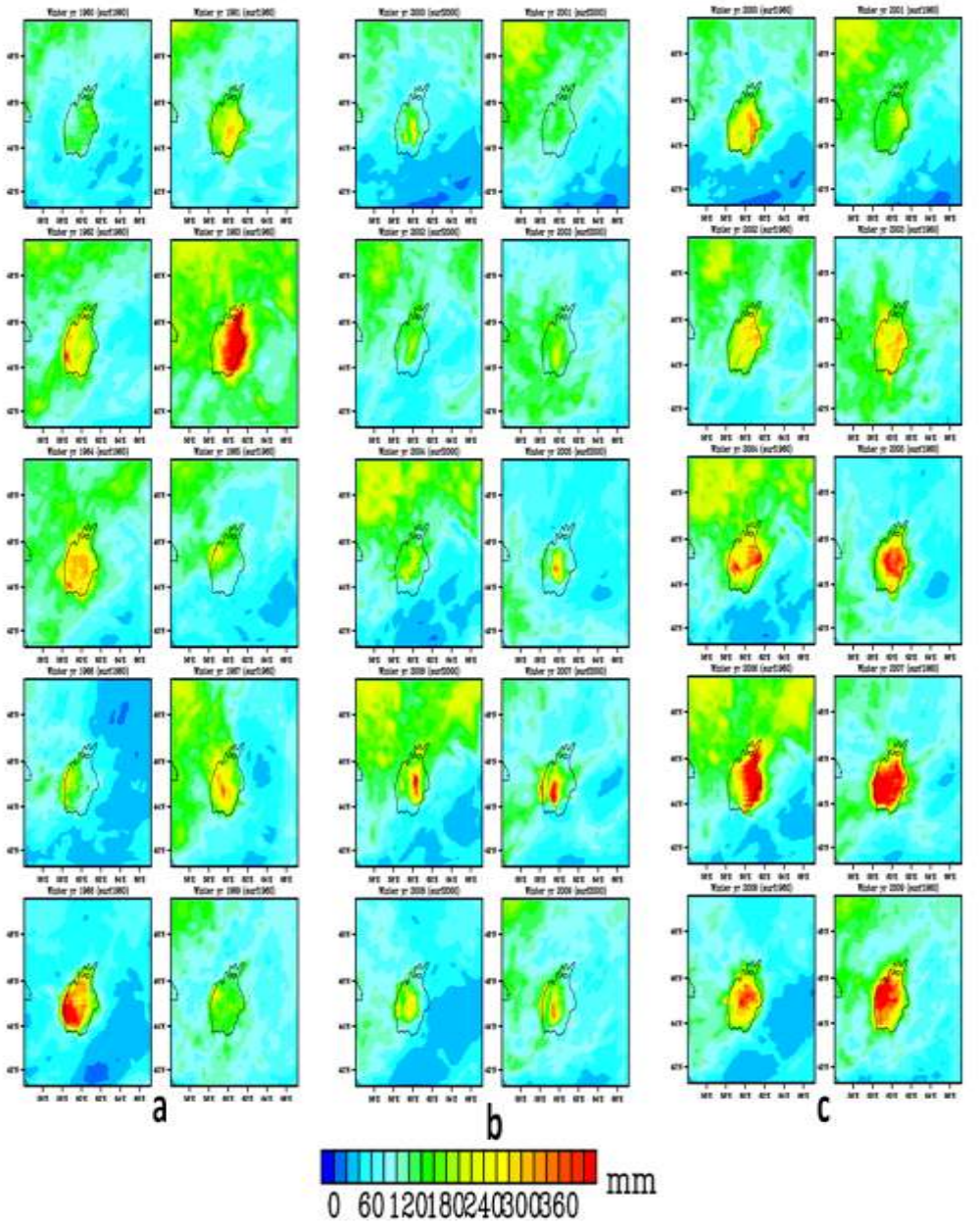

Figure 47: Average rainfall for each winter with (a) surface from year 1960 and boundary conditions from 1960 decade, (b) surface from year 2000 and boundary conditions from 2000 decade, (c) surface from year 1960 and boundary conditions from 2000 decade.

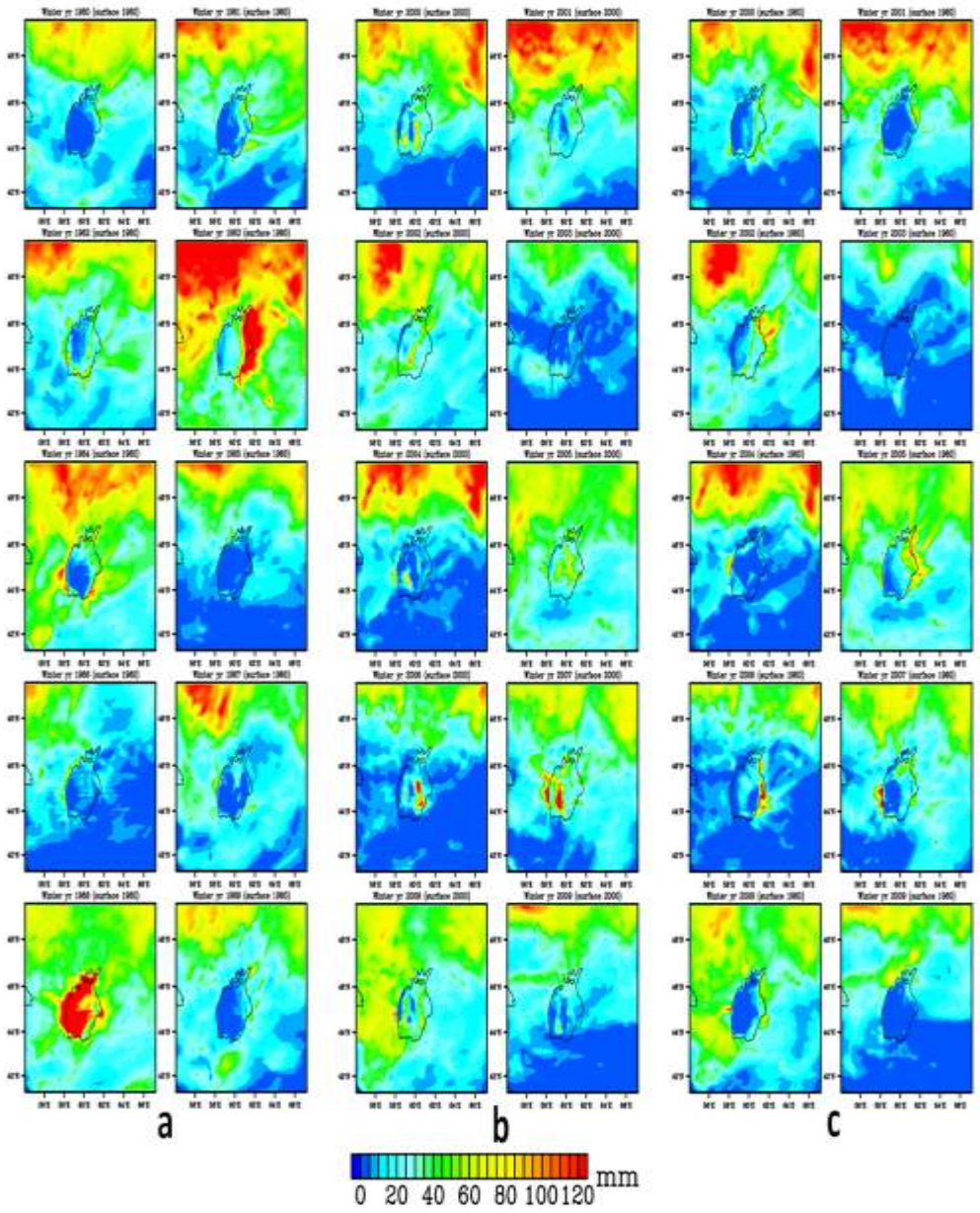

Figure 48: Average snowfall for each winter with (a) surface from year 1960 and boundary conditions from 1960 decade, (b) surface from year 2000 and boundary conditions from 2000 decade, (c) surface from year 1960 and boundary conditions from 2000 decade.

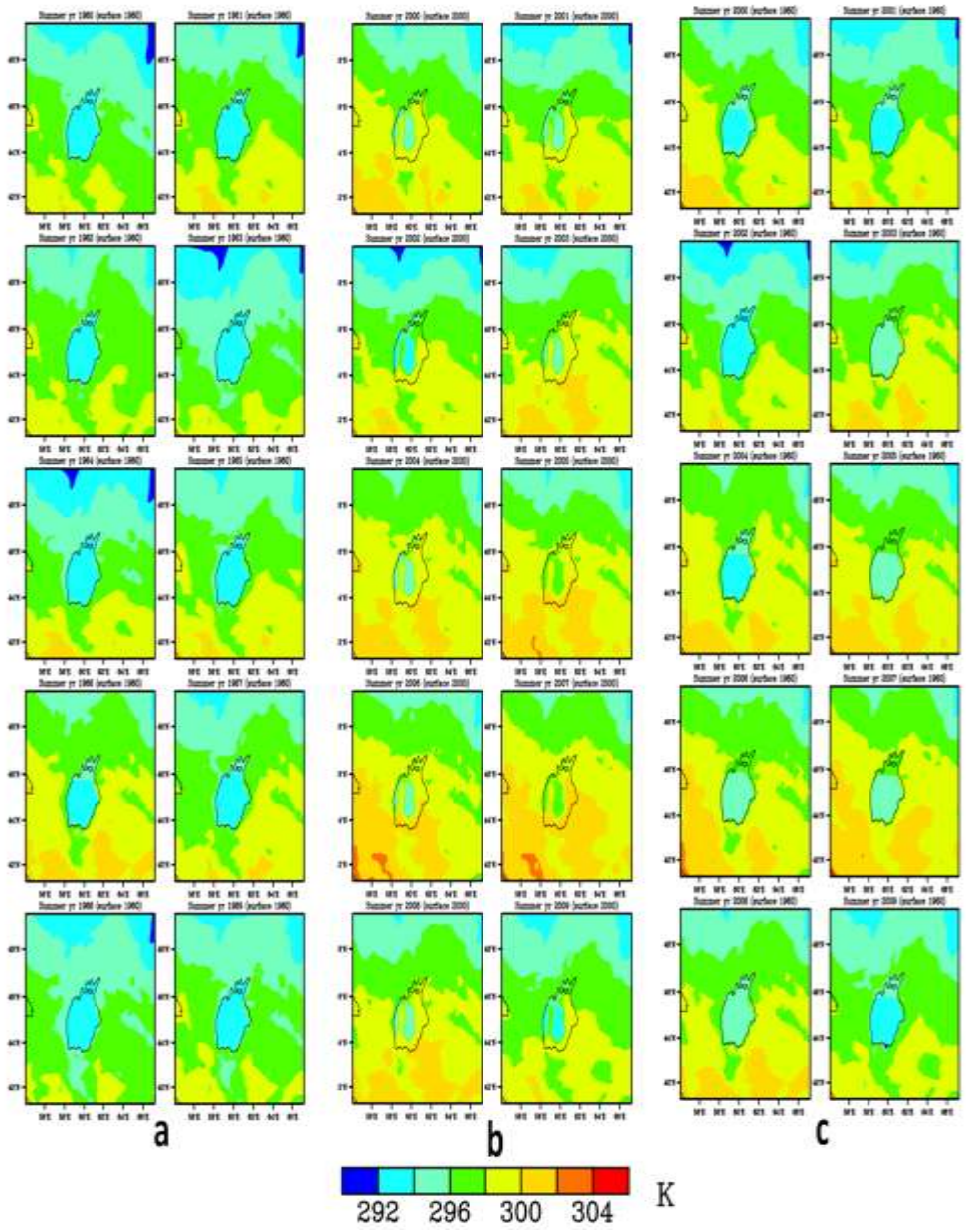

Figure 49: Average temperature for each summer with (a) surface from year 1960 and boundary conditions from 1960 decade, (b) surface from year 2000 and boundary conditions from 2000 decade, (c) surface from year 1960 and boundary conditions from 2000 decade.

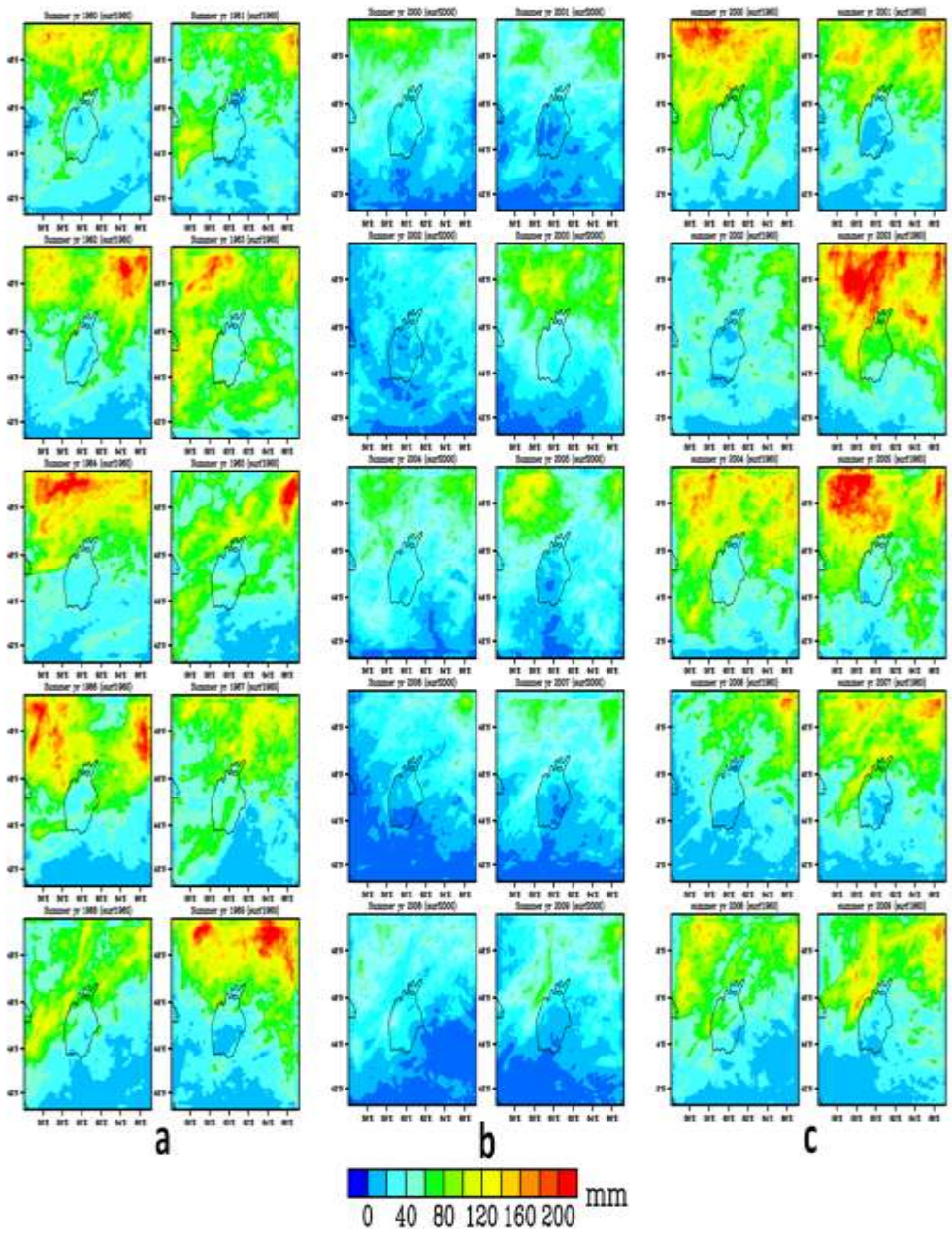

Figure 50: Average rainfall for each summer with (a) surface from year 1960 and boundary conditions from 1960 decade, (b) surface from year 2000 and boundary conditions from 2000 decade, (c) surface from year 1960 and boundary conditions from 2000 decade.

Brief Resume

I am a Ph.D. candidate in Aerospace Engineering at Arizona State University working with Dr. Huei-Ping Huang. My research interests include Climate modeling, Geophysical Fluid Mechanics and Computational Fluid Dynamics. Specifically, I am interested in climate modeling and downscaling for semi-arid regions. I finished my Masters of Science in Aerospace Engineering from ASU working with Dr. H.J.S. Fernando on a CFD project for Palo Verde Nuclear Power plant. I defended my MS thesis titled "Numerical modeling of flow in the condensate polisher vessel of a nuclear reactor".

JOURNAL PUBLICATIONS

Sharma, A.; Huang, H.-P.; (2012). Comparison of observed rainfall with simulations from regional climate simulations for Arizona using WRF. (in preparation).

Sharma, A.; Huang, H.-P.; Zavialov, P.; Khan, V.; (2012) Impact of climate change in Central Asia and its relation with Aral Sea desiccation. (in preparation).

Sharma, A.; Huang, H.-P.; (2012). Regional Climate Simulation for Arizona: Impact of Resolution on Precipitation. *Advances in Meteorology*, Article ID 505726, 13 pages, 2012. doi:10.1155/2012/505726.

Sharma, A.; Brown, J.; Fernando, H. J. S.; (2011). Numerical modeling of flow in the condensate polisher vessel of a nuclear reactor, with applications to PVNGS. *Nuclear Technology*, *174* (1), 18-28.

CONFERENCE PUBLICATIONS

Huang, H.-P.; Hunt, J.C.R; Sharma, A.; Tse, L.; Fernando, H.J.S.; Gunawan, A.; Phelan, P,; Madrid, A.; Thompson, M.; (2011). Axially asymmetric rotating tank experiments for thermally forced stationary waves in geophysical fluids.

64th Annual Meeting of the APS Division of Fluid Dynamics, 56, Baltimore, USA.

Sharma, A.; Huang, H.-P.; (2011). Impact of model resolution on rainfall for Arizona using WRF model. *12th Annual WRF Users Workshop,* NCAR, Boulder, USA.

Sharma, A.; Huang, H.-P.; (2010). Climate downscaling for Arizona using WRF: Dependence of precipitation on model resolution and convective parameterization. *11th Annual WRF Users Workshop*, NCAR, Boulder, USA.

Kohli, N.; Sharma, A.; Crane, C.D.; (2009). Babel Caelestis: Progression from an Outpost to Full Lunar Settlement," *Revolutionary Aerospace Systems Concepts Linkage sponsored by NASA and National Institute of Aerospace (NIA)*, USA.

Sharma, A.; Mikellides, P.; (2008). A Novel Approach for Inter Planetary Explorations: Lunar Support Hub. *American Institute of Aeronautics and Astronautics*, USA.

Sharma, A.; Kohli, N.; (2007). Future Space Explorations: Benefits to Society. *58th International Astronautical Congress*, India.

Kohli, N.; Sharma, A., et al; (2007). Pelican-Supersonic Vehicle," *NASA Langley Research Centre*, USA.